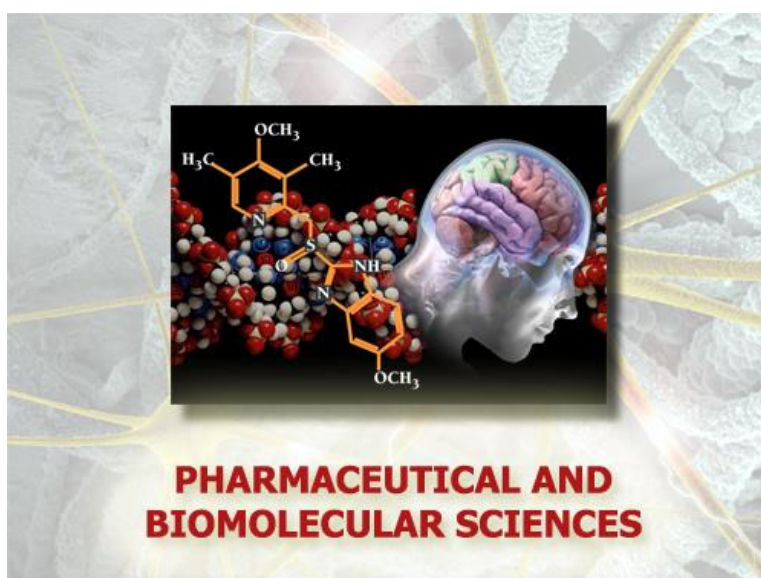


Università degli Studi di Torino



Scuola di Dottorato in
Scienze della Natura e Tecnologie Innovative

Dottorato in
Scienze Farmaceutiche e Biomolecolari
(XXXIII ciclo)



Design and testing of "smart" probes for
multimodal molecular imaging applications

Candidata: Martina Tripepi

Tutors: Prof.ssa Daniela Delli Castelli
Prof. Silvio Aime

A.A. 2017-2020

List of Abbreviations

APT: Amide Proton Transfer

BMS: Bulk Magnetic Susceptibility

c(RGDfC): Cyclo(-Arg-Gly-Asp-D-Phe-Cys)

CEST: Chemical Exchange Saturation Transfer

CPMG: Carr-Purcell-Meiboom-Gill

CT: Computed Tomography

DLS: Dynamic Light Scattering

DPPC: 1,2-dipalmitoyl-sn-glycero-3-phosphocholine

DSPEmPEG2000: 1,2-distearoyl-sn-glycero-3-phosphoethanolamine-N-[methoxy(polyethylene glycol)-2000]

DSPE-PEG2000-Folate: 1,2-distearoyl-sn-glycero-3-phosphoethanolamine-N-[folate(polyethylene glycol)-2000]

DSPE-PEG2000Maleimide: 1,2-distearoyl-sn-glycero-3-phosphoethanolamine-N-[maleimide(polyethylene glycol)-2000]

ECM: extracellular matrix

ELISA: Enzyme-Linked ImmunoSorbent Assay

FACS: Fluorescence-Activated Cell Sorting

FITC: Fluorescein isothiocyanate

FOV: Field of View

GBCA: Gadolinium-based Contrast Agent

GUV: Giant Unilamellar Vesicle

HEPES: (4-(2-hydroxyethyl)-1-piperazineethane-sulfonic acid)

HPDO3A: 10-(2-hydroxypropyl)-1,4,7,10-tetraazacyclododecane-1,4,7-triacetic acid

ICP-MS: Inductively Coupled Plasma-Mass Spectrometry

Liss Rhod PE: 1,2-dioleoyl-sn-glycero-3-phosphoethanolamine-N-(lissamine rhodamine B sulfonyl)

LUV: Large Unilamellar Vesicle

MLV: Multilamellar Vesicle

MRA: Magnetic Resonance Angiography

MRI: Magnetic Resonance Imaging

MSME: Multi Slice Multi Echoes

MTC: Magnetization Transfer Contrast

MTR: Magnetization Transfer Ratio

MTT: 3-(4,5-dimethylthiazol-2-yl)-2,5-diphenyltetrazolium bromide

NEC: Normal Endothelial Cell

OI: Optical Imaging

OLV: Oligolamellar Vesicle

PAI: Photoacoustic Imaging

PEG: polyethylene glycol

PET: Positron Emission Tomography

RARE: Rapid Acquisition with Refocused Echoes
RES: reticuloendothelial system
RF: Radio Frequency
SAR: Specific Absorption Rate
SAXS: Small Angle X-ray Scattering
SPECT: Single Photon Emission Computed Tomography
SPIO: Superparamagnetic iron oxide
SR: Shift Reagent
ST: Saturation Transfer
SUV: Small Unilamellar Vesicle
TE: Echo Time
TEC: Tumor Endothelial Cell
TEM: Transmission Electron Microscopy
TR: Repetition Time
US: Ultrasound

Table of contents

| | |
|--|-----|
| Chapter 1: Introduction | 7 |
| 1.1 Topic of this thesis | 8 |
| 1.2 Molecular Imaging | 8 |
| 1.3 Nanosystems and microsystems in medicine | 10 |
| 1.4 Chemical Exchange Saturation Transfer (CEST) contrast agents for MRI | 12 |
| 1.4.1 Improving the sensitivity of CEST agents: lipoCEST | 15 |
| 1.5 Magnetization Transfer Contrast (MTC) in MRI | 18 |
| 1.6 Liposomes in <i>in vitro</i> diagnostic assays | 21 |
| Chapter 2: | 31 |
| Multilamellar LipoCEST Agents Obtained from Osmotic Shrinkage of Paramagnetically Loaded Giant Unilamellar Vesicles (GUVs) | |
| Chapter 3: | 49 |
| Challenging the Sensitivity of Imaging Probes Targeting Epitopes on the External Surface of Cellular Membranes | |
| Chapter 4: | 61 |
| Detection of U-87 tumor cells by RGD-functionalized/ Gd-containing Giant Unilamellar Vesicles (Gd-GUVs) in Magnetization Transfer Contrast (MTC)-MR images | |
| Chapter 5: | 91 |
| LipHosomes: a new generation of reporters for ligand/anti-ligand assays based on pH readout | |
| Chapter 6: Concluding remarks and future perspectives | 109 |
| List of abstracts | 113 |
| List of publications | 113 |

Chapter 1: Introduction

- Chapter 1 -

Introduction

1.1 Topic of this thesis

The topic of the herein reported work was to develop innovative and highly sensitive smart probes for diagnostic and molecular imaging applications.

The goal of this work relies on the development of a new vesicle-based micrometric system provided with a high sensitivity and biocompatibility and its possible application in biomedicine and diagnostic.

At the beginning of **Chapter 1** a brief introduction about Molecular Imaging and the use of nanosystems in medicine and MRI is reported. Then, basic knowledge of vesicle based CEST contrast agents and Magnetization Transfer Contrast (MTC) is described. Finally, some applications of vesicles in diagnostic assays *in vitro* are highlighted.

Trying to overcome the sensitivity issue, in **Chapter 2**, a new micrometric system based on GUVs is studied as paramagnetic LipoCEST agent and compared to nanometric LipoCEST systems. To highlight the versatility of Giant Unilamellar Vesicles, **Chapter 3** describes a novel application of fluorescent GUVs as receptor imaging; due to their size, they will remain anchored to cell surface without internalization and they could be visualized by fluorescent microscopy. In **Chapter 4**, fluorescent targeted Gd-containing GUVs are studied to demonstrate that small amount of Gd (not detectable by conventional T_1 contrast) could be indirectly visualized using MTC-MRI protocol, in *in vitro* and *in vivo* experiments. In **Chapter 5**, a diagnostic kit kind of application of small and giant unilamellar vesicles is studied and reported; they were exploited as probes to assess a pH readout-based ligand/anti-ligand assay.

The thesis ends with **Chapter 6** where the conclusions and general discussions on the future perspectives and applications of the studied vesicles are reported.

1.2 Molecular Imaging

Molecular imaging is a rapidly evolving field in biomedical research, aiming at non-invasively visualize, characterize and measure physiological and pathological processes at the cellular and molecular levels within intact living organisms.¹⁻⁴

The revolutionary idea at the origin of molecular imaging is to probe molecular abnormalities at the basis of diseases, rather than imaging the end effects. This scientific discipline is a multidisciplinary approach that combines biomedicine (cellular biology, molecular biology, medicine and pharmacology), chemistry, physics, engineering and radiology.

A large number of molecules or molecular events could be targeted by molecular imaging including gene expression, mRNA, receptors or other components on the cell membrane surface, enzymes, metabolites and other key molecules or changes in microenvironments at the basis of pathophysiological processes.

The application of Molecular Imaging procedures may provide useful information in many different diseases like cancer, cardiovascular disease, neurological disease, metabolic disease, inflammation, infection, etc...

Chapter 1: Introduction

Molecular Imaging is based on the use of single or combined techniques such as X-Ray Computed Tomography (CT), Positron Emission Tomography (PET), Single Photon Emission Computed Tomography (SPECT), Magnetic Resonance Imaging (MRI), Ultrasound (US) and Optical Imaging (OI).

The main characteristics of the different molecular imaging modalities vary considerably in terms of sensitivity and resolution as summarized in Table 1.

Table 1. Comparison among the different imaging modalities (Magnetic Resonance Imaging, Positron Emission Tomography, Single Photon Emission Computed Tomography, Optical Imaging, Computed Tomography, Ultrasounds, Photo Acoustic Imaging).

| Imaging technique | Imaging source | Resolution | Depth | Sensitivity | Imaging probes | Probe amount |
|-------------------|------------------|----------------------|----------|---------------------------|--|---------------------|
| MRI | Radiowave | 10-100 μm | No limit | mM to μM (Low) | Para-, superparamagnetic materials; endogenous contrast (APT, MTC, endogenous molecules) | μg to mg |
| PET/SPECT | γ -rays | 1-2 mm | No limit | pM (High) | Radionuclides ^{19}F , ^{124}I , $^{99\text{m}}\text{Tc}$ | ng |
| OI | Vis or NIR light | 2-3 mm | < 1 cm | nM to pM (Medium) | Fluorochromes, quantum dots, fluorescent proteins | μg to mg |
| CT | X-rays | 50-100 μm | No limit | Not well characterized | High atomic number atoms (Iodine) | NA |
| US | Ultrasonic waves | 50-100 μm | cm | nM | Microbubbles | μg to mg |
| PAI | Vis light | 50-100 μm | cm | nM to pM (Medium) | Fluorochromes, SPR-based metal nanoparticles, fluorescent proteins | μg to mg |

Radionuclide imaging, i.e. PET and SPECT imaging, is characterized by a huge sensitivity, being able to visualize a very low amount of radiotracer, but its spatial resolution is limited thus requiring coupling with other techniques to anatomically localize the signal obtained. Moreover, potential exposure to radiations limits its applications especially for multiple imaging sessions.⁵

Magnetic Resonance Imaging, instead, is characterized by an outstanding spatio-temporal resolution, the capability to investigate deep regions, the absence of ionizing radiation and the possibility to generate contrast by using different mechanism but characterized by low sensitivity (10^{-3} to 10^{-5} M).⁶

Hence, according to the process to be visualized, every time the best-able technique should be employed. A combination of different imaging process, such as PET/CT, PET/MRI, PET/US or OI/PET, could also be possible.⁷

In most cases the administration of contrast agents, also known as imaging probes, is necessary to obtain more precise and subtle information about pathophysiological events normally not distinguishable in a MR image, thus expanding the capability of *in vivo* molecular imaging and molecular diagnostics.^{8,9}

Finally, by combining diagnostic information given by Imaging with a therapeutic procedure, it is possible to create targeted, tailored therapies with the ability of simultaneously find, diagnose, and treat diseases. This strategy is a promising approach in the era of personalized medicine also known as theranostics.¹⁰⁻¹³

1.3 Nanosystems and microsystems in medicine

Over the past decades, an increasing interest has been devoted to the development of nano- or microsystems able to carry a large amount of molecules.¹⁴ Moreover, nano- and micro-systems are easily functionalized on their surface with molecular targeting vectors, thus providing an increase in selectivity for the carried molecules. The field of application in medicine ranges from therapy to diagnostic (either *in vivo* or *in vitro*). Concerning their use in MR image there is a huge potential for Molecular Imaging application. As a matter of fact, Gadolinium contrast agents currently on the market require a tissue concentration in the order of 10^{-7} mol/g to obtain sufficient signal in the resulting MR image.¹⁵

Such a number is too high to be able to image sparse molecular biomarkers expressed in living organism since typical receptors are normally present in low concentrations (10^{-9} to 10^{-13} mol/g).¹⁶ Actually, the interest in nanosystems arose from the need to enhance the *in vivo* efficiency of many drugs, limited by low stability, poor selectivity, rapid clearance and metabolism.

Several nanosystem-based formulations have entered clinical trials and some of them are already applied in the cure of important diseases, mainly in the field of cancer therapy, but also as antibacterial and antifungal agents *e.g.* Doxil[®], DaunoXome[®] and Ambisome[®].¹⁷⁻²⁰

More recently, the ability of nanosystems to act as carriers of a great variety of molecules led up to the combination of therapeutics and diagnostics in a single particle, giving rise to theranostics agents. This term derives from the Greek words *therapeia* (to treat) and *gnosis* (knowledge), referring to the visualization of the response to a specific treatment.²¹ This innovative discipline lays the foundations for a more personalized and controlled medicine, as well as gives new opportunities in the preclinical and clinical development of new and improved therapies using molecular imaging.

So far, a wide variety of carriers have been investigated, including lipid-based self-assembled systems, polymeric/inorganic particles, *host-guest* supramolecular adducts, and naturally-occurring systems like lipoproteins, proteins, viral capsids and bacteria (Figure 1).

These carriers vary considerably in terms of size, composition, biocompatibility, use and costs.^{14,23} Moreover a precise design of the system could allow controlled release of the drug/activation of

Chapter 1: Introduction

the imaging probe just in presence of specific chemical or physical triggering stimuli like pH, enzymes, heat, ultrasound or magnetic forces.

Lipid-based nanosystems, including liposomes, are among the most used.^{22,24} Their biocompatibility and biodegradability have attracted much interest in the medical field, as carriers for the delivery of drugs to pathological tissues.^{25,26}

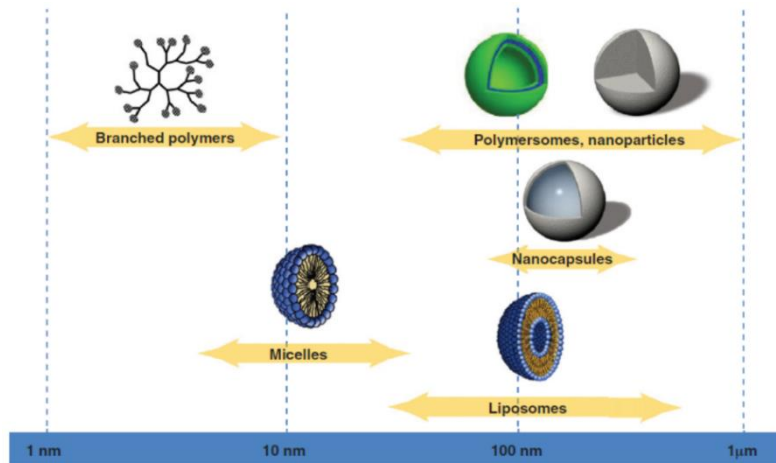
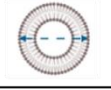
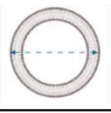


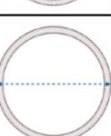


Figure 1. Schematic representation of different classes of nanosystems. Adapted from 22.

Liposomes are defined as nanosized artificial vesicles composed by an aqueous core entrapped by one or more bilayers made of natural or synthetic lipids, first by Bangham in 1964. They can be classified according to their lamellarity (uni-, oligo-, and multi-lamellar vesicles), size (small, large or giant) and preparation method (such as thin film method or reverse phase evaporation method). The selection of the appropriate method allows for the production of unilamellar vesicles, owing one lipid bilayer and diameters of 20–100 nm (Small Unilamellar Vesicles - SUVs), 100-1000 nm (Large Unilamellar Vesicles - LUVs) or > 1 μm (Giant Unilamellar Vesicles – GUV) or multilamellar vesicles (MLV), owing several concentric lipid bilayers in an onion-skin arrangement and diameters >500 nm (Table 2).

Table 2. Characteristics of different typologies of liposomes, size and lamellarity. Adapted from 27.

| | | |
|-----------------------------------|---|---------------|
| Small Unilamellar Vesicle (SUV) |  | 20 – 100 nm |
| Large Unilamellar Vesicle (LUV) |  | 100 nm – 1 μm |
| Large Multilamellar Vesicle (LMV) |  | > 500 nm |
| Oligolamellar Vesicle (OLV) |  | 100 nm – 1 μm |
| Giant Unilamellar Vesicle (GUV) |  | > 1 μm |

SUVs, LUVs and GUVs contain a large aqueous core and are preferentially used to encapsulate water-soluble molecules, while MLV are generally characterized by high lipid content thus being suitable to passively entrap lipid-soluble drugs.²⁸ The physicochemical properties of liposomes, such as net surface charge, hydrophobicity, size, fluidity and packing of the lipid bilayers, influence their stability. It has been demonstrated that nanoscale carriers with hydrophobic surfaces administered *in vivo* are taken up primarily by the reticuloendothelial system (RES), thus limiting the circulation time of the particles. Coating nanoparticles with hydrophilic molecules, such as poly(ethylene) glycol (PEG), is a commonly employed strategy to overcome the rapid reticuloendothelial system uptake.

Incorporation of therapeutic and diagnostic pharmaceuticals (*via* covalent or non-covalent bonds) to these carriers might be advantageous because of increased water solubility of sparingly soluble agents, enhanced permeability across the physiological barriers, substantial changes in the drug biodistribution, increased bioavailability, and reduction of adverse side effects. Moreover, targeting ligands can be attached to vesicles to specifically recognize and bind to overexpressed receptors. Finally, pH-, thermo-, ultrasound-, or light-sensitive block copolymers allow for controlled vesicles dissociation and triggered drug release.

The use of these systems in molecular imaging is of great interest, especially in MRI. As mentioned before, nanocarriers have the great power of bringing several molecules of contrast agent in a single particle thus increasing sensitivity. Moreover, liposomal formulations bearing appropriate phospholipids can reduce the exchange of the water molecules across the lipid membrane with the consequent modulation in the contrast detection. Then variations in pH, enzymatic activity, temperature and/or other parameters can impair membrane water permeability thus allowing the detection of a contrast that may report not only about the presence of the diagnostic tool in a certain region, but also about pH, enzymatic activity, or temperature conditions of that region. A scrupulous characterization of pathologic areas is thus possible just employing sensitive nanosystems.

1.4 Chemical Exchange Saturation Transfer (CEST) contrast agents for MRI

The first proof-of-principle study of Chemical Exchange Saturation Transfer (CEST) was demonstrated by Balaban and co-workers.²⁹ A CEST agent contains mobile protons in chemical exchange with bulk water protons. The MRI water proton signal intensity is modulated by the transfer of saturated magnetization from the CEST agents to the water around, upon irradiation with a proper radiofrequency (RF) that saturate CEST proton signal. Therefore, the application of the RF saturation pulse at the resonance frequency of the CEST protons pool allows indirectly saturating water proton signal. As a result, a decrease in water signal can be detected by standard MR imaging sequences and can provide an indirect measurement for the concentration of the species of interest (Figure 2).³⁰ For this reason, the CEST signal can be detectable also at millimolar and even sub-millimolar concentration, since the effect is transferred to the water protons (~110

M). This novel contrast mechanism soon becomes an attractive alternative to relaxation-based contrast, particularly at high magnetic field strengths when the relaxivity effects are lower.

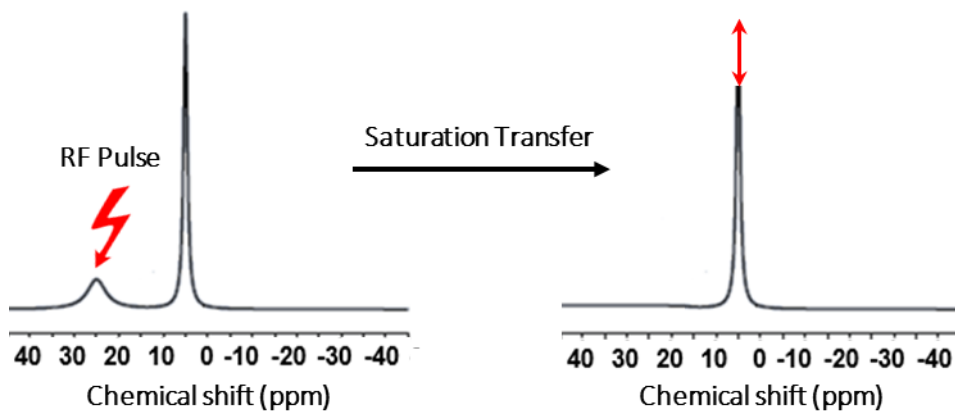


Figure 2. Mobile protons are saturated at their specific resonance frequency in the ^1H -NMR spectrum; then, the saturation is transferred to water and unsaturated protons. After a suitable period, this effect becomes visible on the water signal, which decreases over time.

Basic requirement to generate CEST contrast and distinguish the two groups of mobile protons is that the exchange rate (k_{ex}) between chemical substances and water is in the slow/intermediate regime, meaning that it has to be smaller than the chemical shift ($\Delta\omega$) between them: $k_{\text{ex}} \leq \Delta\omega$. The proton exchange process is dependent on molecule concentration, temperature and on pH: the exchange rate is slower at low pH than at high pH due to base catalysis of protons exchange.¹⁸ By plotting the acquired water signal intensity relative to the irradiated saturation frequency, a CEST spectrum is generated (Z-spectrum). It describes the water signal intensity in function of the applied RF offset. A decrease in water signal reflects the presence of specific mobile protons of a CEST system; the direct water saturation is set at 0 ppm (Figure 3).

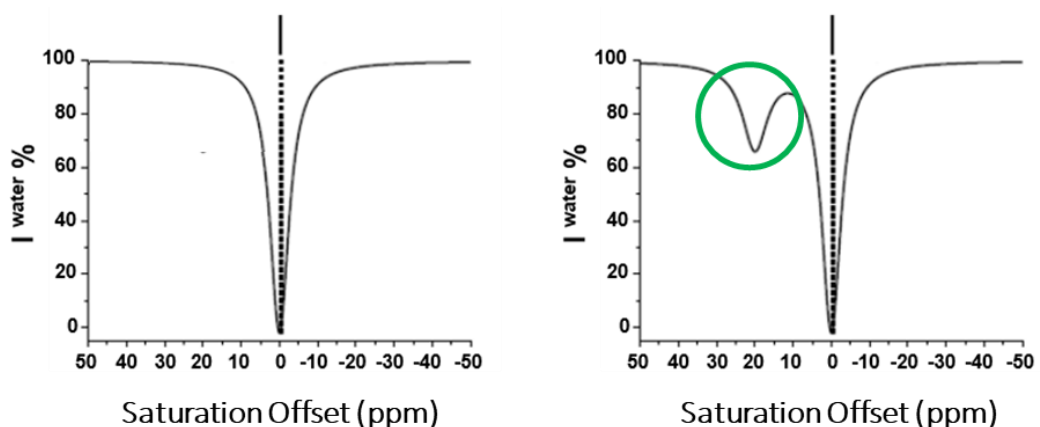


Figure 3. The measurement of normalized water saturation as function of irradiation frequency (from +50 to -50 ppm) generates a Z-spectrum (left); when irradiating the mobile protons at 25 ppm generates a Z-spectrum (right) where the signal decreases due to direct (water) saturation.

The CEST signal is quantified by the so called MT ratio (MTR) asymmetry analysis which is based on the comparison of the intensity of the water signal upon irradiation at two different symmetric

frequency offsets from the bulk water signal; one corresponds to the resonance frequency offset of the mobile protons of the CEST agent (SI_{ON}) and the other one corresponds to the water signal intensity at symmetric frequency (SI_{OFF}). This approach (MTR_{asym}) also explained in Figure 4, considers the symmetric effect on water signal caused by the application of RF pulse; thus, the saturation transfer efficiency is calculated as:

$$ST\% = \left(1 - \frac{SI_{ON}}{SI_{OFF}}\right) = \left(\frac{SI_{OFF} - SI_{ON}}{SI_{OFF}}\right) \times 100$$

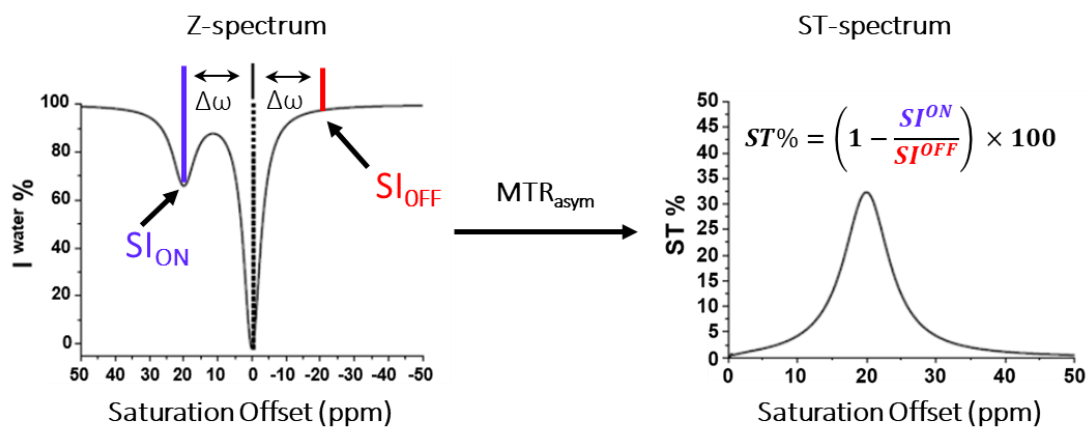


Figure 4. Representation on MTR_{asym} analysis applied on a Z spectrum (left) in order to generate the ST% spectrum used to evaluate the efficacy of a CEST agent.

Compared to conventional T_1 and T_2 contrast mechanism, the contrast generated by CEST agents can be switched “on” or “off” by modulating the saturation radiofrequency pulse. Moreover, the signal of the mobile protons of CEST agents is generally sharp and their frequencies are well defined. This frequency-encoding property of CEST allows to detect multiple contrast agents simultaneously in the same region in a single MRI scan. Moreover, the detection of CEST agents does not require a pre-contrast image, because the contrast is generated by the comparison between the water signal measured after the irradiation of the mobile protons of the CEST agent and that obtained by simply moving the irradiation frequency far from the absorption of the mobile protons.³²

CEST agents can be classified in two main groups: *diamagnetic CEST*, (diaCEST) that detect molecule which typical chemical shift is few ppm away of bulk water protons (5-10 ppm from the water signal) and *paramagnetic CEST*, (paraCEST) that involve complexes of lanthanide metal ions such as Eu, Dy, Ho, Er, Tm and Yb that increase the chemical shift separation between the pool of exchangeable proton and the bulk water (10-700 ppm).

A modern and more complete classification has been proposed by van Zijl and co-workers.³³ Three main classes can be distinguished by referring to different exchange mechanism: atom (proton) exchange, molecular exchange and compartmental exchange. The proton exchange class, where a single proton of the molecule is in exchange, is constituted by the majority part of diamagnetic CEST (diaCEST) compounds and several paramagnetic (paraCEST). In the second class a molecule

is in exchange; an example is the water molecules coordinated to paraCEST agent. The last class is made by systems in which there is a compartmental exchange. The most representative example is the one of lipoCEST; they are liposomes in which the water inside the compartment is shifted with respect to the water outside thanks to the presence of a paramagnetic agent loaded into the compartment and eventually by changing the shape of the compartment to induce a bulk magnetic susceptibility (BMS) anisotropy.

1.4.1 Improving the sensitivity of CEST agents: lipoCEST

The main determinants of the efficacy of CEST agents are: *i)* the number of exchangeable protons to be irradiated; *ii)* their exchange rate and *iii)* the T_1 value of solvent water protons in the solution containing the CEST agent. After the pivotal work of Ward and Balaban,³¹ who reported a number of diamagnetic molecules that act as potential CEST agents, a step ahead in terms of sensitivity enhancement was achieved with the introduction of paramagnetic CEST (paraCEST) agents.³⁴⁻³⁶ Indeed, the large chemical shift values of the mobile protons of a paramagnetic agent allow the selective irradiation of fast exchanging protons, thereby improving the efficiency of saturation transfer. However, despite the good progress attained, the sensitivity of CEST contrast is still lower than the contrast mechanism based on the paramagnetic effect on the T_1 relaxation of water protons.

The need to increase drastically the sensitivity of these probes led to the consideration of systems possessing a very large number of magnetically equivalent water molecules. Large amounts of water molecules can be found in the inner cavities of nanovesicular systems, such as liposomes. According to the size of the nanoparticles (50 – 250 nm in diameter), the number of exchangeable protons can reach as high as 10^6 – 10^8 . However, this pool cannot be used as such for the CEST experiment, because the $\Delta\omega$ separation between the inner water protons and the bulk water protons is too small to exceed the exchange rate. To remove the isochronicity between these two exchanging signals, it was suggested that a paramagnetic water shift reagent (SR) should be entrapped in the inner liposomal cavity. These agents were named lipoCEST agents.³⁷ Analogous to most paraCEST agents, the SRs used are Ln(III) complexes in which the ninth coordination site around the Ln ion is occupied by a water molecule; however, unlike paraCEST agents, the bound water must be in fast exchange with the intraliposomal water molecules. The coordinated water molecule and the intraliposomal water molecules, being in fast exchange, yield a single absorption whose chemical shift value ($\delta^{\text{intralipo}}$) is the sum of three contributions:

$$\delta^{\text{intralipo}} = \delta_{\text{DIA}} + \delta_{\text{BMS}} + \delta_{\text{HYP}} \quad [1]$$

where δ_{DIA} is the diamagnetic contribution (almost negligible), δ_{BMS} is the bulk magnetic susceptibility (BMS) contribution and δ_{HYP} is the hyperfine contribution. δ_{BMS} does not require a direct chemical interaction between the water molecules and the paramagnetic center, and is dependent on the shape and orientation of the compartment containing the paramagnetic SR, the concentration of the SR and the effective magnetic moment (μ_{eff}) of the paramagnetic center. In

a spherical compartment, such as conventional liposomes, the susceptibility effects average out to zero, and therefore the only contribution to the intraliposomal water shift is δ_{HYP} . Conversely, δ_{HYP} requires a chemical interaction between the paramagnetic center and the water molecule and can operate either through bond (contact shift) or space (pseudocontact or dipolar shift). The pseudocontact term is proportional to the molar fraction of metal-bound water molecules and to the shift of the water protons at the coordination site (δ_M):

$$\delta_{HYP} = \frac{[bound\ water] \times q(\delta_M)}{[bulk\ water]} \quad [2]$$

where q is the number of coordinated water molecules, and δ_M is directly proportional to the magnetic anisotropy of the complex ($\Delta\chi$) and a geometric factor (G) defined as follows:

$$\Delta\chi = C_J \times A_2^0 \langle r^{-2} \rangle$$

$$G \propto \frac{3\cos^2\theta - 1}{r^3}$$

where C_J is Bleaney's constant which characterizes each Ln(III) ion and can have a positive or negative value. In particular, C_J is positive for Europium (Eu), Erbium (Er), Thulium (Tm), Ytterbium (Yb) and negative for Cerium (Ce), Praseodymium (Pr), Neodymium (Nd), Samarium (Sm), Terbium (Tb), Dysprosium (Dy) and Holmium (Ho). C_J for Gd is equal to zero, thereby clarifying why Gd(III) complexes do not work as water SR, at least in spherical compartments.

The term $A_2^0 \langle r^{-2} \rangle$ refers to crystal field parameters of the complex and can assume positive or negative values, θ is the angle between the principal magnetic axes of the complex and the Ln–H bound water vector, and r is the distance between the paramagnetic center and the protons of the coordinated water molecule. Hence, the capability of an SR to shift the resonance of water protons depends on the Ln ion and the geometry of the complex.

On this basis, Tm(III) and Dy(III) complexes appear to be the candidates of choice because they have high C_J values with opposite sign (positive and negative, respectively). For a given ligand, the induced shift depends on the magnitude of the C_J values of the coordinated Ln(III) ion only, and therefore Dy(III) complexes induce a larger shift than their Tm(III) analogues.

The resonance frequency offset of the water protons inside liposomes may be modulated by changing the nature and concentration of the entrapped SR. However, the shift of the inner water resonance in this type of lipoCEST is limited by the maximum amount of SR that can be entrapped (for *in vivo* use, the osmolarity of the solution inside the vesicle must be isotonic with the physiological medium, *i.e.* 300 mOsm/L). Hence, using the most efficient mononuclear Ln(III) complexes, the maximum chemical shift separation between the inner and outer water resonance was *ca.* ± 4 ppm, according to the sign of the Bleaney's constant of the Ln(III) ion. Therefore, the *in vivo* application of these agents appears to be limited by the interference with the overlapping endogenous magnetization transfer contribution. To overcome this drawback, it is necessary to

explore other routes to attain larger separation between the inner water and the bulk water resonances.

Equation 1 shows that the shift of the intraliposomal water protons can be increased by acting on the BMS effect. However, to achieve this goal, the paramagnetic SR must be entrapped in a non-spherical compartment. The liposomal membrane is semipermeable, and this property can be exploited to modify the shape of liposomes by applying osmotic gradients. When a lipoCEST agent loaded with a hypo-osmotic solution of SR is added to a solution isotonic with the physiological fluids, the vesicles shrink and leak water to reach osmotic equilibrium, and this process induces a change in vesicle shape (Figure 5).³⁸

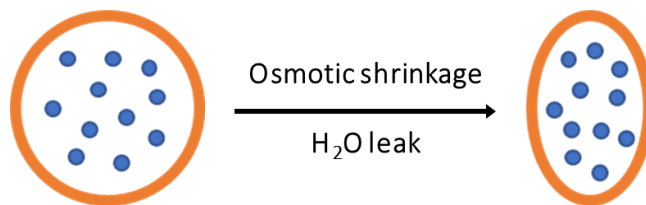


Figure 5. Osmotic shrinkage of spherical lipoCEST agents leads to a leakage in water and the consequent change in the shape; the formation of aspherical vesicles is appreciated.

The non-spherical lipoCEST agents obtained show large BMS contributions to the shift of the resonance of the water protons entrapped in the vesicles. Interestingly, this contribution is larger than the hyperfine term, thus allowing a dramatic increase (from 4 to 12 ppm) of the chemical shift separation between the two exchanging pools. In addition, the BMS effect depends on the concentration of the SR entrapped in the non-spherical liposomes and, again, the maximum payload of SR is limited by osmotic rules. Hence, consisting of the incorporation of amphiphilic SRs into the liposome membrane have been designed to further increase the concentration of SR without affecting the osmolarity of the intraliposomal cavity (Fig 6).³⁹

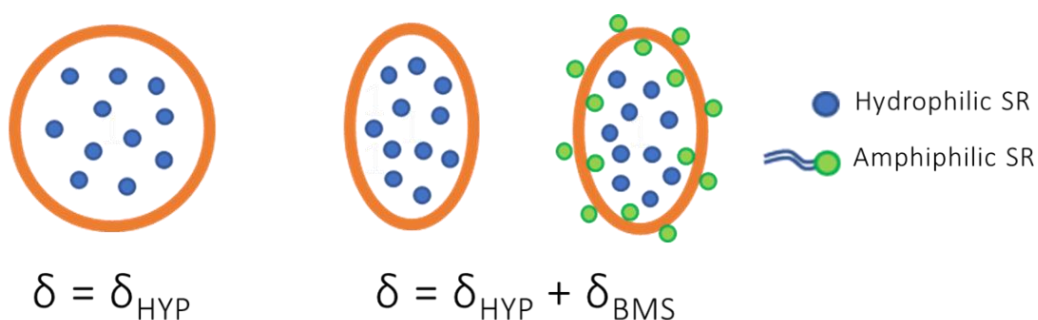


Figure 6. Schematic overview of the different generations of lipoCEST agents. On the left, lipoCEST of the first generation disfruted only the hyperfine contribution to the $\delta_{\text{intralipo}}$ due to the entrapping of hydrophilic SRs. On the right, second generation lipoCESTs are schematized: both in the case of the osmotic shrinkage and more upon the addition of amphiphilic SR in the membrane, $\delta_{\text{intralipo}}$ results higher due to the BMS contribution.

The sign of δ_{BMS} depends on the orientation of the non-spherical vesicle with respect to the external magnetic field B_0 . It is known that phospholipid-containing particles are naturally oriented in a magnetic field, and the driving force for the orientation is the sign of the magnetic susceptibility anisotropy ($\Delta\chi$) of the bilayer.⁴⁰ Hence, the orientation may be switched from

parallel to perpendicular by changing the sign of $\Delta\chi$. As phospholipidic membranes possess a negative $\Delta\chi$ value, the orientation change requires a switch of $\Delta\chi$ to a positive value. This result can be achieved on incorporation of an amphiphilic paramagnetic complex with a positive magnetic susceptibility anisotropy into the liposome bilayer.⁴¹

Thanks to the exploitation of the BMS effect, the window of the accessible irradiation frequency values can be extended considerably from *ca.* 4 ppm observed for spherical vesicles to *ca.* \pm 30 ppm extending the possibility to visualize multiple lipoCEST probes.⁴²

Despite the impressive improvements achieved *in vitro*, one of the major drawbacks for the *in vivo* translation of nanoparticles is represented by their sequestration from organs of the mononuclear phagocytic system (MPS), such as the liver and spleen. This general issue, which obviously holds for other classes of MRI probe, is even more problematic for CEST particles, as it leads to the degradation of the particles or to their compartmentalization, both processes converging to hamper the CEST response.⁴³ As for most MRI reporters, the targets for CEST particles are in the vascular and extracellular matrix. The possibility of the simultaneous visualization of several biomarkers in the same anatomical region is a tremendous driving force for investing efforts in this class of MRI agent.

In Chapter 2, a new micrometric system based on Giant Unilamellar Vesicles is designed and studied as a paramagnetic LipoCEST agent. Different formulations englobing hydrophilic Tm- and Dy-complexes and incorporating amphiphilic ones are produced and compared. Further comparisons were also made with analogous nanometric LipoCEST.

1.5 Magnetization Transfer Contrast (MTC) in MRI

Magnetization Transfer Contrast (MTC) is an MRI procedure that has been shown to be particularly useful in several clinical applications.⁴⁴⁻⁵⁴ It does not require the use of exogenous agents but exploits off-resonance RF pulses that induce an energy exchange process, mediated by dipolar interaction between macromolecules and bulk water.

Since different tissues have diverse macromolecular compositions, the degree of interaction, can differ widely, generating high tissue contrast. MTC is obtained by combining saturation transfer techniques with standard MRI protocols.

The use of the saturation transfer technique in MR spectroscopy was described in 1963 by Forsén and Hoffman, who used it to calculate the exchange rate of specific chemical reactions.⁵⁵ In the 1970's Edzes and Samulski proposed that cross-relaxation between ¹H pools was the main relaxation mechanism in biological systems such as collagen and muscles.^{56,57} However, it was in 1989 that Wolf and Balaban first applied these principles to *in vivo* measurements.⁵⁸

In biological systems, protons can be described as being part of two pools as reported in Figure 7. The so-called *free pool* consists of mobile protons in free bulk water. This pool has a narrow signal (10-100 Hz), a relatively long T₂ (> 10-100 ms) and in standard MRI it provides the bulk of the signal.

Chapter 1: Introduction

The second pool or *bound pool* consists of restricted protons bound in proteins or other large macromolecules and cellular membranes. This pool has a very broad signal (10-50 kHz), a very short T_2 (< 0.1 ms) and with conventional MRI its signals are not directly detectable due to the very short T_2 ; therefore, these protons do not contribute to the image.

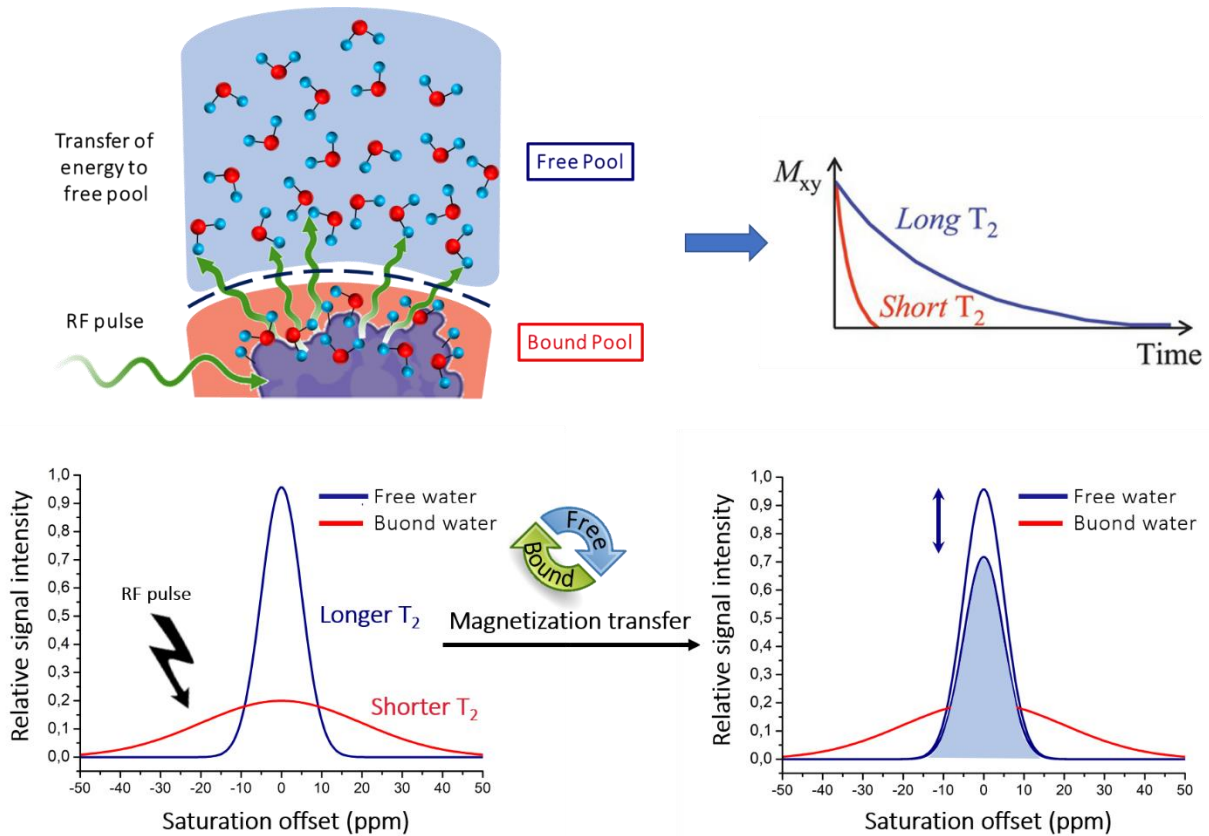


Figure 7. Top) Schematic representations of protons in biological systems and consequent behaviour in terms of relaxation times. Bottom) Schematic representation of Magnetization Transfer (MT); the 'bound' pool is selectively saturated without affecting the free water pool; the magnetization is transferred between bound and free water protons and led to a decrease of the net magnetization of bulk water, thus decreasing the signal e generating MT contrast.

Note that both pools have approximately the same central resonance frequency (Fig. 7) and that the only difference is the larger spread in resonance frequencies of the restricted protons. Under normal MR conditions magnetization is exchanged from the 'free pool' to the 'bound pool' and vice versa, resulting in an equilibrium situation characteristic for that type of tissue. A special situation occurs when the 'bound pool' is selectively saturated. This will result in no net magnetization of the 'bound pool' and thus a difference in magnetization between the pools is created. If we irradiate selectively the macromolecular pool (without affecting the bulk water pool) using a specially designed RF pulse (called the MT Pulse), the free water pool could serve as the final "lattice" or reservoir to disperse the injected energy.

By stimulating the bound pool of protons, the Boltzmann distribution would be upset in favour of higher energy states. To return to equilibrium, this energy would need to be transferred to nearby unaffected spins, some of which are in the free water pool. These free water protons would be driven to higher energy states, partially saturating and hence reducing the net magnetization of

the free water pool. If a second RF pulse were applied to the free water pool to generate an NMR signal, that signal would be smaller than it would have otherwise due to magnetization transfer of energy from the MT pulse (Figure 7).

The objective of this MTC is to saturate and suppress selective signals from specific tissues to increase the contrast.

Prior to the beginning of the imaging acquisition cycle a saturation pulse is applied at a frequency that is different from the resonant frequency of the “free” protons. Therefore, it does not have a direct effect on the protons that are producing the signals. However, the saturation pulse is within the broader resonant frequency of the “bound” protons. It produces saturation of the longitudinal magnetization in the “bound” pool.

The effect of the saturation is now transferred to the longitudinal magnetization of the “free” pool by the magnetization transfer process. The key is that the transfer is not the same for all tissues. Only the tissues with a relatively high magnetization transfer coupling and a significant bound pool concentration will experience the saturation and have their signals reduced in intensity. Fluids, fat, and bone marrow have very little, if any, magnetization transfer. Therefore, they will not experience the transferred saturation, and will remain relatively bright in the images.

Most other tissues have some, but varying degrees of, magnetization transfer. When the MTC technique is used, the saturation produced by the RF pulse applied to the “bound” protons will be transferred to the “free” protons, but only in those tissues that have a significant magnetization transfer capability. The result is that these tissues will be saturated to some degree and their signal intensities will be reduced. Therefore, MTC is a way of enhancing contrast in an image by suppressing the signals from tissues that have a relatively high magnetization transfer.

The magnitude of this MT effect can be quantified by obtaining two sets of images (one with an MT pulse and one without it) and then digitally subtracting them. The magnetization transfer ratio (MTR) for a given voxel may then be defined and computed as:

$$MTR = \frac{(S_0 - S_{MT})}{S_0}$$

where S_0 is the magnitude of tissue signal before the MT pulse and S_{MT} is the signal after the MT pulse has been applied. The relative difference in signal between two adjacent tissues (A and B) is known as magnetization transfer contrast (MTC).

In clinical MRI, MT pulses are used prior to certain sequences to improve contrast; the common method of RF excitation is to apply an MT pulse with a bandwidth of a few hundred hertz and centre frequency shifted from the water resonance by 1000 to 25,000 Hz. This off-resonance pulse has enough power to saturate protons in the immobile pool without directly affecting those in free water.

Several useful clinical applications of MTC have already been demonstrated. This suppression of background tissue by MT pulses makes the technique especially useful as an adjunct to MR angiography (MRA). Small vessel detail and overall image contrast are significantly improved when MT pulses are employed.⁵⁹

Another potential use of MT pulses is together with T_2 -weighted images when early demyelination or protein destruction may be detected before its appearance on routine images. In this application, diseased tissues with altered protein-water interactions are less suppressed by MT pulses, rendering them more conspicuous on T_2 -weighted images.⁶⁰⁻⁶²

Finally, a potential use of MT pulses is in conjunction with contrast-enhanced T_1 -weighted images. A paramagnetic contrast agent works by reducing the T_1 of the lesion that it enters, thereby resulting in a relative signal intensity increase in the lesion in T_1 -weighted scans. If MTC techniques are applied in conjunction with the contrast agent, then the MT effect on the lesion will be greatly reduced since MTC is T_1 driven, i.e., the shorter T_1 , the less signal loss due to a fixed MT irradiation. However, the signal from the surrounding tissue experiences a significant MT effect, and consequently the lesion to normal tissue contrast is further enhanced.

In Chapter 4, a new contrast-enhanced MRI strategy based on fluorescent targeted Gd-containing GUVs is reported; it has been developed to increase the sensitivity threshold for the detection of T_1 contrast agents. It has been demonstrated that, in some cases, MTC can be a more sensitive way to detect the presence of low amounts of a T_1 contrast agent. The described methodology increases the collection of the MRI tools, and may have a great potential for applications of paramagnetic Gd-complexes in molecular imaging investigations.

1.6 Liposomes in *in vitro* diagnostic assays

Liposomes could be exploited in *in vitro* assays, either as amplification entities or as molecular recognition agents, thanks to the functional moieties which could be introduced on their membrane and the huge payload in the inner cavity.⁶³

In principle, any bioassay based on the detection of a molecular recognition event can be amplified by replacing the reporting agent with a vesicle containing many copies of a given molecule. Moreover, further amplification can be achieved when the liposomal payload is represented by an enzyme. An important step in the set-up of a liposome-based assay deals with the effective separation of vesicles bound to the target from the unbound ones. The detection stage often involves the release of the payload from the targeted liposome which is easily pursued by the application of different kind of external stimuli such as US, heat, surfactants or enzymes.

The peculiar properties of liposomes make them interesting systems for novel applications in biology and medicine. First, they can provide large amplification effects thanks to the reporter payload and moreover, their size makes them suitable tools for multiple interactions to enhance the binding to biological entities, from proteins to nucleic acid, to exosomes, viruses, and bacteria. Much attention has been devoted to the synthetic methodologies related to the attachment of antibodies or other ligands to the surface of the liposomes.

Different chemically active groups (including groups for coupling to biomolecules) can easily be incorporated on the liposome surface. It is important to say that the properties and the amount of such groups can be varied over a wide range enabling a strong control of vesicle properties (e.g.,

size of the liposomes and surface density of covalently bound biomolecules). The application of liposomes for analysis was reviewed by Edwards and Baeumner.⁶⁴ Thanks to the ability of liposomes to encapsulate very high amounts of such labels, the detectable analyte concentration can be reduced by 2 - 3 orders of magnitude.⁶⁵ Comparison of biotin-enzyme-tagged liposomes with a biotin-tagged enzyme showed a 100–1000-fold increase in signal with liposomes for different immuno-systems and different ways of signal generation.⁶⁴ A 500-fold lower LOD was found measuring the fluorescence of lysed dye-encapsulated liposomes versus a single-labelled probe.⁶⁶

The hugest field of *in vitro* diagnostic assays liposomes are used in is immunoassay. Immunoassays are biological analytical techniques where the dosing of the analyte relies on the specificity of the interaction between an antigen and an antibody. The use of liposomes whose surface is functionalized with antibodies is under intense scrutiny as it seems to offer promising strategies in many diagnostic and therapeutic fields including cancer, as well as inflammatory, cardiovascular, infectious, autoimmune and neurodegenerative diseases.^{67,68}

Furthermore, the design of the nanocarrier may include the possibility of a triggered release of its payload through a proper responsive design of the liposome characteristics.

When the liposomes are loaded with imaging agents, immunoliposomes are of great interest for diagnostic applications within a molecular imaging approach. On this basis, immunoliposomes have been considered in the context of different signal amplification strategies to improve the detection sensitivity of immunoassays.^{69,70} Thus, liposomes have then been utilized as signal enhancers in analytical biochemical assays for decades in various formats, with antibodies being the most powerful antigen recognition vectors.⁶⁹⁻⁷¹

In immunoassays, the liposomes are loaded with many types of signal-generating labels, such as fluorescent probes, metals, and chelates. Loading liposomes with enzymes is also a possibility, especially when a further improvement of signal amplification and sensitivity is needed.⁷² In liposome immunoassays (LIA), liposome-encapsulated markers (e.g., a fluorescent dye) are prepared as phospholipid compositions coupled with either an analyte or antibody using standardized procedures.⁷³

One of the first proposed immunoassays consisted of an agglutination assay, where liposomes carrying an antigen of interest on their surface are made to interact with antibodies against a certain pathogen in order to assess the presence of a given disease.⁷⁴

Over the years, much progress has been made, in particular, in the development of immunoliposome-coupled enzyme-linked immunosorbent assay (ELISA) where liposomes are used in the common ELISA protocol setting as signal amplifiers, compared to Abs conjugated with single reporter molecules.⁷⁵ Some examples of lateral-flow tests were also described and for application in lateral-flow tests, liposomes could be targeted with DNA,⁶⁶ RNA,⁷⁶ and antigens.⁷⁷⁻⁷⁹

Liposomes are also used, since decays, in the biosensor and bioanalysis field, thanks to their excellent ability of encapsulate signal marker compounds across a wide spectrum of sensing modalities, as extensively reviewed by Liu and Boyd.⁸⁰

Chapter 1: Introduction

In Chapter 3 an early study about a novel application of fluorescent GUVs as *in vitro* molecular recognition agents is reported. In particular, it is demonstrated how fluorescent Folate-targeted GUVs will remain anchored to cell surface without internalization and they could be visualized by fluorescent microscopy.

In Chapter 5, a low cost *in vitro* diagnostic kind of application of LUVs and GUVs is studied and reported. They were exploited as probes to assess a pH readout-based ligand/anti-ligand assay.

References

1. Massoud, T. F., Gambhir, S. S. (2003) Molecular imaging in living subjects: seeing fundamental biological processes in a new light. *Genes & Development*, 17(5), 545-80.
2. Weissleder, R., & Mahmood, U. (2001). Molecular imaging. *Radiology*, 219(2), 316-333.
3. Brindle, K. (2008). New approaches for imaging tumour responses to treatment. *Nature Reviews Cancer*, 8(2), 94-107.
4. Weissleder, R., & Pittet, M. J. (2008). Imaging in the era of molecular oncology. *Nature*, 452(7187), 580-589.
5. Gambhir, S. S. (2002). Molecular imaging of cancer with positron emission tomography. *Nature Reviews Cancer*, 2(9), 683-693.
6. Srinivas, M., Heerschap, A., Ahrens, E. T., Figdor, C. G., & de Vries, I. J. M. (2010). 19F MRI for quantitative in vivo cell tracking. *Trends in biotechnology*, 28(7), 363-370.
7. Martí-Bonmatí, L., Sopena, R., Bartumeus, P., & Sopena, P. (2010). Multimodality imaging techniques. *Contrast media & molecular imaging*, 5(4), 180-189.
8. Boros, E., Gale, E. M., & Caravan, P. (2015). MR imaging probes: design and applications. *Dalton transactions*, 44(11), 4804-4818.
9. Jasanoff, A. (2007). MRI contrast agents for functional molecular imaging of brain activity. *Current opinion in neurobiology*, 17(5), 593-600.
10. Terreno, E., Uggeri, F., & Aime, S. (2012). Image guided therapy: the advent of theranostic agents. *Journal of controlled release*, 161(2), 328-337.
11. Lammers, T., Aime, S., Hennink, W. E., Storm, G., & Kiessling, F. (2011). Theranostic nanomedicine. *Accounts of chemical research*, 44(10), 1029-1038.
12. Pan, D., Schmieder, A. H., Wickline, S. A., & Lanza, G. M. (2011). Manganese-based MRI contrast agents: past, present and future. *Tetrahedron*, 67(44), 8431.
13. Waterton, J. C., & Pylkkanen, L. (2012). Qualification of imaging biomarkers for oncology drug development. *European journal of cancer*, 48(4), 409-415.
14. Villaraza, A. J., Bumb, A., & Brechbiel, M. W. (2010). Macromolecules, dendrimers, and nanomaterials in magnetic resonance imaging: the interplay between size, function, and pharmacokinetics. *Chemical reviews*, 110(5), 2921-2959.
15. Gupta, H., Weissleder, R. (1996). Targeted contrast agents in MR imaging. *Magnetic Resonance Imaging Clinics of North America*. 4(1):171-184.

Chapter 1: Introduction

16. Strijkers, G. J., Mulder, W. J. M., Van Heeswijk, R. B., Frederik, P. M., Bomans, P., Magusin, P. C. M. M., & Nicolay, K. (2005). Relaxivity of liposomal paramagnetic MRI contrast agents. *Magnetic Resonance Materials in Physics, Biology and Medicine*, 18(4), 186-192.
17. Chan, S., Davidson, N., Juozaityte, E., Erdkamp, F., Pluzanska, A., Azarnia, N., ... & Myocet Study Group. (2004). Phase III trial of liposomal doxorubicin and cyclophosphamide compared with epirubicin and cyclophosphamide as first-line therapy for metastatic breast cancer. *Annals of Oncology*, 15(10), 1527-1534.
18. Bulbake, U., Doppalapudi, S., Kommineni, N., & Khan, W. (2017). Liposomal formulations in clinical use: an updated review. *Pharmaceutics*, 9(2), 12.
19. Allen, T. M., & Cullis, P. R. (2013). Liposomal drug delivery systems: from concept to clinical applications. *Advanced drug delivery reviews*, 65(1), 36-48.
20. Ambati, S., Ferarro, A. R., Kang, S. E., Lin, J., Lin, X., Momany, M., ... & Meagher, R. B. (2019). Dectin-1-targeted antifungal liposomes exhibit enhanced efficacy. *MSphere*, 4(1).
21. Bentzen, S. M. (2005). Theragnostic imaging for radiation oncology: dose-painting by numbers. *The lancet oncology*, 6(2), 112-117.
22. Beija, M., Salvayre, R., Lauth-de Viguerie, N., & Marty, J. D. (2012). Colloidal systems for drug delivery: from design to therapy. *Trends in biotechnology*, 30(9), 485-496.
23. Terreno, E., Uggeri, F., & Aime, S. (2012). Image guided therapy: the advent of theranostic agents. *Journal of controlled release*, 161(2), 328-337.
24. Botta, M., & Tei, L. (2012). Relaxivity enhancement in macromolecular and nanosized GdIII-based MRI contrast agents. *European Journal of Inorganic Chemistry*, 2012(12), 1945-1960.
25. Sercombe, L., Veerati, T., Moheimani, F., Wu, S. Y., Sood, A. K., & Hua, S. (2015). Advances and challenges of liposome assisted drug delivery. *Frontiers in pharmacology*, 6, 286.
26. Bozzuto, G., & Molinari, A. (2015). Liposomes as nanomedical devices. *International journal of nanomedicine*, 10, 975.
27. Sforzi, J., Palagi, L., & Aime, S. (2020). Liposome-Based Bioassays. *Biology*, 9(8), 202.
28. Immordino, M. L., Dosio, F., & Cattel, L. (2006). Stealth liposomes: review of the basic science, rationale, and clinical applications, existing and potential. *International journal of nanomedicine*, 1(3), 297.
29. Ward, K. M., Aletras, A. H., & Balaban, R. S. (2000). A new class of contrast agents for MRI based on proton chemical exchange dependent saturation transfer (CEST). *Journal of magnetic resonance*, 143(1), 79-87.

Chapter 1: Introduction

30. Liu, G., Song, X., Chan, K. W., & McMahon, M. T. (2013). Nuts and bolts of chemical exchange saturation transfer MRI. *NMR in Biomedicine*, 26(7), 810-828.
31. Ward, K. M., & Balaban, R. S. (2000). Determination of pH using water protons and chemical exchange dependent saturation transfer (CEST). *Magnetic Resonance in Medicine: An Official Journal of the International Society for Magnetic Resonance in Medicine*, 44(5), 799-802.
32. Terreno, E., Stancanello, J., Longo, D., Castelli, D. D., Milone, L., Sanders, H. M., ... & Aime, S. (2009). Methods for an improved detection of the MRI-CEST effect. *Contrast media & molecular imaging*, 4(5), 237-247.
33. Van Zijl, P. C., & Yadav, N. N. (2011). Chemical exchange saturation transfer (CEST): what is in a name and what isn't?. *Magnetic resonance in medicine*, 65(4), 927-948.
34. Zhang, S., Winter, P., Wu, K., & Sherry, A. D. (2001). A novel europium (III)-based MRI contrast agent. *Journal of the American Chemical Society*, 123(7), 1517-1518.
35. Yoo, B., & Pagel, M. D. (2006). A PARACEST MRI contrast agent to detect enzyme activity. *Journal of the American Chemical Society*, 128(43), 14032-14033.
36. Aime, S., Barge, A., Delli Castelli, D., Fedeli, F., Mortillaro, A., Nielsen, F. U., & Terreno, E. (2002). Paramagnetic lanthanide (III) complexes as pH-sensitive chemical exchange saturation transfer (CEST) contrast agents for MRI applications. *Magnetic Resonance in Medicine: An Official Journal of the International Society for Magnetic Resonance in Medicine*, 47(4), 639-648.
37. Aime, S., Delli Castelli, D., & Terreno, E. (2005). Highly sensitive MRI chemical exchange saturation transfer agents using liposomes. *Angewandte Chemie International Edition*, 44(34), 5513-5515.
38. Terreno, E., Cabella, C., Carrera, C., Delli Castelli, D., Mazzon, R., Rollet, S., ... & Aime, S. (2007). From spherical to osmotically shrunken paramagnetic liposomes: an improved generation of LIPOCEST MRI agents with highly shifted water protons. *Angewandte Chemie International Edition*, 46(6), 966-968.
39. Delli Castelli, D., Terreno, E., Carrera, C., Giovenzana, G. B., Mazzon, R., Rollet, S., ... & Aime, S. (2008). Lanthanide-loaded paramagnetic liposomes as switchable magnetically oriented nanovesicles. *Inorganic chemistry*, 47(8), 2928-2930.
40. Ottiger, M., & Bax, A. (1998). Characterization of magnetically oriented phospholipid micelles for measurement of dipolar couplings in macromolecules. *Journal of biomolecular NMR*, 12(3), 361-372.
41. Burdinski, D., Pikkemaat, J. A., Emrullahoglu, M., Costantini, F., Verboom, W., Langereis, S., ... & Huskens, J. (2010). Targeted lipoCEST contrast agents for magnetic resonance imaging:

Chapter 1: Introduction

alignment of aspherical liposomes on a capillary surface. *Angewandte Chemie International Edition*, 49(12), 2227-2229.

42. Terreno, E., Castelli, D. D., Milone, L., Rollet, S., Stancanello, J., Violante, E., & Aime, S. (2008). First ex-vivo MRI co-localization of two LIPOCEST agents. *Contrast media & molecular imaging*, 3(1), 38-43.
43. Delli Castelli, D., Dastrù, W., Terreno, E., Cittadino, E., Mainini, F., Torres, E., ... & Aime, S. (2010). In vivo MRI multicontrast kinetic analysis of the uptake and intracellular trafficking of paramagnetically labeled liposomes. *Journal of Controlled Release*, 144(3), 271-279.
44. Horsfield, M. A. (2005). Magnetization transfer imaging in multiple sclerosis. *Journal of Neuroimaging*, 15, 58S-67S.
45. Bagley, L. J., Grossman, R. I., & McGowan, J. C. (1999). Magnetization transfer contrast: its utility as a technique and its application to central nervous system pathology. *Neurology*, 53(5 Suppl 3), S49-51.
46. Lee, J. S., Xia, D., Ge, Y., Jerschow, A., & Regatte, R. R. (2014). Concurrent saturation transfer contrast in in vivo brain by a uniform magnetization transfer MRI. *Neuroimage*, 95, 22-28.
47. Giulietti, G., Bozzali, M., Figura, V., Spanò, B., Perri, R., Marra, C., ... & Cercignani, M. (2012). Quantitative magnetization transfer provides information complementary to grey matter atrophy in Alzheimer's disease brains. *Neuroimage*, 59(2), 1114-1122.
48. Dousset, V., Grossman, R. I., Ramer, K. N., Schnall, M. D., Young, L. H., Gonzalez-Scarano, F., ... & Cohen, J. A. (1992). Experimental allergic encephalomyelitis and multiple sclerosis: lesion characterization with magnetization transfer imaging. *Radiology*, 182(2), 483-491.
49. Rausch, M., Tofts, P. S., Lervik, P., Walmsley, A. R., Mir, A., Schubart, A., & Seabrook, T. (2009). Characterization of white matter damage in animal models of multiple sclerosis by magnetization transfer ratio and quantitative mapping of the apparent bound proton fraction f. *Multiple Sclerosis Journal*, 15(1), 16-27.
50. Rovira, À., & León, A. (2008). MR in the diagnosis and monitoring of multiple sclerosis: an overview. *European journal of radiology*, 67(3), 409-414.
51. Rovira, A., Alonso, J., Cucurella, G., Nos, C., Tintoré, M., Pedraza, S., ... & Montalban, X. (1999). Evolution of multiple sclerosis lesions on serial contrast-enhanced T1-weighted and magnetization-transfer MR images. *American journal of neuroradiology*, 20(10), 1939-1945.
52. Ropele, S., Schmidt, R., Enzinger, C., Windisch, M., Martinez, N. P., & Fazekas, F. (2012). Longitudinal magnetization transfer imaging in mild to severe Alzheimer disease. *American journal of neuroradiology*, 33(3), 570-575.

Chapter 1: Introduction

53. Bigot, C., Vanhoutte, G., Verhoye, M., & Van der Linden, A. (2014). Magnetization transfer contrast imaging reveals amyloid pathology in Alzheimer's disease transgenic mice. *Neuroimage*, 87, 111-119.
54. Pérez-Torres, C. J., Reynolds, J. O., & Pautler, R. G. (2014). Use of magnetization transfer contrast MRI to detect early molecular pathology in Alzheimer's disease. *Magnetic resonance in medicine*, 71(1), 333-338.
55. Forsén, S., & Hoffman, R. A. (1963). Study of moderately rapid chemical exchange reactions by means of nuclear magnetic double resonance. *The Journal of Chemical Physics*, 39(11), 2892-2901.
56. Edzes, H. T., & Samulski, E. T. (1977). Cross relaxation and spin diffusion in the proton NMR of hydrated collagen. *Nature*, 265(5594), 521-523.
57. Edzes, H. T., & Samulski, E. T. (1978). The measurement of cross-relaxation effects in the proton NMR spin-lattice relaxation of water in biological systems: hydrated collagen and muscle. *Journal of Magnetic Resonance (1969)*, 31(2), 207-229.
58. Wolff, S. D., & Balaban, R. S. (1989). Magnetization transfer contrast (MTC) and tissue water proton relaxation in vivo. *Magnetic resonance in medicine*, 10(1), 135-144.
59. Henkelman, R. M., Stanisiz, G. J., & Graham, S. J. (2001). Magnetization transfer in MRI: a review. *NMR in Biomedicine: An International Journal Devoted to the Development and Application of Magnetic Resonance In Vivo*, 14(2), 57-64.
60. Elster, A. D., King, J. C., Mathews, V. P., & Hamilton, C. A. (1994). Cranial tissues: appearance at gadolinium-enhanced and nonenhanced MR imaging with magnetization transfer contrast. *Radiology*, 190(2), 541-546.
61. Elster, A. D., Mathews, V. P., King, J. C., & Hamilton, C. A. (1994). Improved detection of gadolinium enhancement using magnetization transfer imaging. *Neuroimaging Clinics of North America*, 4(1), 185-192.
62. Mathews, V. P., Elster, A. D., King, J. C., Ulmer, J. L., Hamilton, C. A., & Strottmann, J. M. (1995). Combined effects of magnetization transfer and gadolinium in cranial MR imaging and MR angiography. *AJR. American journal of roentgenology*, 164(1), 169-172.
63. Goryacheva, I. Y., Lenain, P., & De Saeger, S. (2013). Nanosized labels for rapid immunotests. *TrAC Trends in Analytical Chemistry*, 46, 30-43.
64. Edwards, K. A., & Baeumner, A. J. (2006). Liposomes in analyses. *Talanta*, 68(5), 1421-1431.
65. Chun, P., in: Lateral Flow Immunoassay, Humana Press, New York, USA, (2009), Wong, R.C., Tse, H.Y. (Editors), p.75.

Chapter 1: Introduction

66. Edwards, K. A., & Baeumner, A. J. (2006). Optimization of DNA-tagged dye-encapsulating liposomes for lateral-flow assays based on sandwich hybridization. *Analytical and bioanalytical chemistry*, 386(5), 1335-1343.
67. Zalipsky, S., Hansen, C. B., de Menezes, D. E. L., & Allen, T. M. (1996). Long-circulating, polyethylene glycol-grafted immunoliposomes. *Journal of Controlled Release*, 39(2-3), 153-161.
68. Manjappa, A. S., Chaudhari, K. R., Venkataraju, M. P., Dantuluri, P., Nanda, B., Sidda, C., ... & Murthy, R. S. R. (2011). Antibody derivatization and conjugation strategies: application in preparation of stealth immunoliposome to target chemotherapeutics to tumor. *Journal of Controlled Release*, 150(1), 2-22.
69. Khreich, N., Lamourette, P., Boutal, H., Devilliers, K., Créminon, C., & Volland, H. (2008). Detection of Staphylococcus enterotoxin B using fluorescent immunoliposomes as label for immunochromatographic testing. *Analytical biochemistry*, 377(2), 182-188.
70. Park, S., & Durst, R. A. (2000). Immunoliposome sandwich assay for the detection of Escherichia coli O157: H7. *Analytical biochemistry*, 280(1), 151-158.
71. Shin, J. H., & Kim, M. H. (2008). Development of liposome immunoassay for Salmonella spp. using immunomagnetic separation and immunoliposome. *Journal of microbiology and biotechnology*, 18(10), 1689-1694.
72. Chaize, B., Colletier, J. P., Winterhalter, M., & Fournier, D. (2004). Encapsulation of enzymes in liposomes: high encapsulation efficiency and control of substrate permeability. *Artificial cells, blood substitutes, and biotechnology*, 32(1), 67-75.
73. Kim, C. K., & Park, K. M. (1994). Liposome immunoassay (LIA) for gentamicin using phospholipase C. *Journal of immunological methods*, 170(2), 225-231.
74. Kung, V. T., Vollmer, Y. P., & Martin, F. J. (1986). Large liposome agglutination technique for the serological detection of syphilis. *Journal of immunological methods*, 90(2), 189-196.
75. Shukla, S., Leem, H., & Kim, M. (2011). Development of a liposome-based immunochromatographic strip assay for the detection of Salmonella. *Analytical and bioanalytical chemistry*, 401(8), 2581-2590.
76. Zaytseva, N. V., Montagna, R. A., Lee, E. M., & Baeumner, A. J. (2004). Multi-analyte single-membrane biosensor for the serotype-specific detection of Dengue virus. *Analytical and bioanalytical chemistry*, 380(1), 46-53.
77. Ho, J. A., & Wauchope, R. D. (2002). A strip liposome immunoassay for aflatoxin B1. *Analytical chemistry*, 74(7), 1493-1496.

Chapter 1: Introduction

78. Ho, J. A. A., Wu, L. C., Chang, L. H., Hwang, K. C., & Hwu, J. R. R. (2010). Liposome-based immunoaffinity chromatographic assay for the quantitation of immunoglobulin E in human serum. *Journal of Chromatography B*, 878(2), 172-176.
79. Ho, J. A. A., Zeng, S. C., Tseng, W. H., Lin, Y. J., & Chen, C. H. (2008). Liposome-based immunostrip for the rapid detection of Salmonella. *Analytical and bioanalytical chemistry*, 391(2), 479-485.
80. Liu, Q., & Boyd, B. J. (2013). Liposomes in biosensors. *Analyst*, 138(2), 391-409.

- Chapter 2 -

Multilamellar LipoCEST Agents Obtained from Osmotic Shrinkage of Paramagnetically Loaded Giant Unilamellar Vesicles (GUVs)

Martina Tripepi, Giuseppe Ferrauto, Paolo Oronzo Bennardi, Silvio Aime, Daniela Delli Castelli*

Published as Communication: *Angewandte Chemie*, **2020**, *132*(6), 2299-2303.

Abstract

Moving from nano- to micro-systems may not just be a matter of scale, but it might imply changes in the properties of the systems that can open new routes for the development of efficient MRI contrast agents. This is the case reported in the present paper, where giant liposomes (Giant Unilamellar Vesicles, GUVs) loaded with Ln(III) complexes have been studied as MRI CEST contrast agents. The comparison between nanosized liposomes (Small Unilamellar Vesicles, SUVs) and GUVs sharing the same formulation led to differences that could not be accounted only in term of the mere increase in size (from 100-150 nm to 1-2 μm). Upon osmotic shrinkage GUVs yielded a Saturation Transfer effect of three order of magnitude higher than SUVs consistent with the increase in vesicles volume. Confocal microscopy showed that the shrinkage of GUVs resulted in multilamellar particles whereas SUVs are known to yield asymmetrical, discoidal shape.

Keywords: Giant • LipoCEST • Liposomes • Osmotic stress • Vesicles

Introduction

MRI takes great advantage from the use of contrast agents as they may add functional information to the outstanding anatomical resolution attainable by this technique.^{1,2}

Along the years, most attention has been devoted to relaxation enhancers that affect the relaxation rates of water protons in the region where they distribute.³⁻⁵

In recent years, much attention has been devoted to chemicals that allow their detection through procedures based on frequency encoding.^{6,7} In this context the most interesting class is represented by CEST agents that are chemicals that affect the signal intensity of the water proton resonance through the transfer of saturated magnetization from their exchangeable proton pool.⁸⁻

¹¹ A drawback of the CEST agents is represented by their relatively low sensitivity as their detection in a MR image requires the number of exchangeable protons to be in the millimolar range.^{12,13}

An important step ahead along the improvement of the attainable sensitivity was achieved with the introduction of LipoCEST in which the exchangeable pool of protons is represented by the large ensemble of water molecules contained in the liposomal inner aqueous cavity whose NMR resonance is properly shifted by the presence of paramagnetic shift reagents.^{12,14-17}

A further sensitivity enhancement has been achieved on passing from spherical liposomes to osmotically shrunken ones that yield highly shifted values for the intraliposomal water resonance.¹⁸ Up to now these are among the most sensitive CEST agents (hundreds pM for the spherical vesicles to tents pM for the shrunken ones). According to their membrane formulation, the shrunken LipoCEST are able to orient themselves when exposed to a magnetic field providing markedly large effects on the chemical shift of the intravesicular water molecules.^{19,20}

Despite the huge potential of these systems, the *in vivo* use has been hampered from macrophagic uptake or cell internalization. In fact, paramagnetic liposomes can work as LipoCEST agents as long as their content remains inside the vesicles whereas it became CEST-invisible when the vesicles undergo a degradation.²¹

In this work we have tried to overcome some of the limitations and to improve the potential shown by the paramagnetic SUVs by increasing their size.

Results and discussion

Giant Unilamellar Vesicles (GUVs) are liposomes of micron size; they have been known for over half a century and have been used as cell mimicking systems but no use as imaging agents has yet been reported. These systems have dimensions ranging from 0.8 μm to 2 μm or even higher depending on the methodology of preparation or on the membrane formulation. GUVs and SUVs bearing the same paramagnetic cargo were prepared to assess their differences when they act as LipoCEST agents. Giant liposomes were prepared following the so-called “natural swelling” method reported in literature with some modifications.²² Chart 1 summarizes liposomes’ components in the membrane and in the internal cavity.

Chapter 2: Giant Unilamellar Vesicles as LipoCEST agents

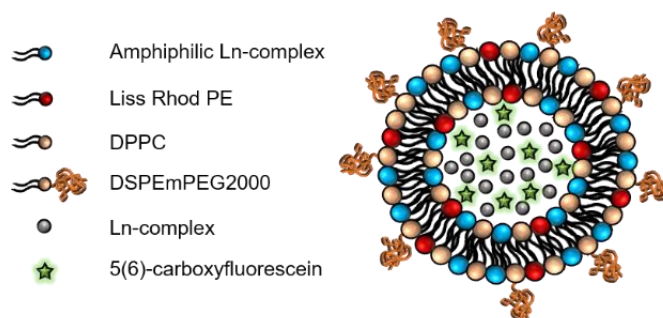


Chart 1. Components of the membrane and molecules engulfed into GUVs.

Table 1 reports the composition of the vesicles used in this work.

Table 1. Characteristics of the studied liposomes

| Name | Formulation | Content |
|-----------------|--|---|
| Lipo-1 (SUV) | DPPC/Amphiphilic Tm-complex/Liss Rhod PE/ DSPEmPEG2000 81.95/15/0.05/3 | 40 mM TmHPDO3A 20 μ M carboxyfluorescein |
| Lipo-2 (GUV) | DPPC/Amphiphilic Tm-complex/Liss Rhod PE/ DSPEmPEG2000 81.95/15/0.05/3 | 40 mM TmHPDO3A 20 μ M carboxyfluorescein |
| Lipo-3 (GUV) | DPPC/Amphiphilic Dy-complex/Liss Rhod PE/ DSPEmPEG2000 81.95/15/0.05/3 | 40 mM DyHPDO3A 20 μ M carboxyfluorescein |

Because the size of GUVs was expected to range between 1 and 3 μ m, the most common techniques used to characterize the particles size (*e.g.* DLS or FACS) could not be used as their reliability fall in a lower or higher range of detection, respectively. Therefore, confocal fluorescence microscopy sampling was exploited as the technique for assessing the size of the herein prepared giant liposomes and fluorescent formulations were prepared for this purpose.

Figure 1 shows a representative fluorescence microscopy image of a spherical GUV and the size distribution; the mean size of these giant particles resulted to be $1.22 \pm 0.15 \mu$ m.

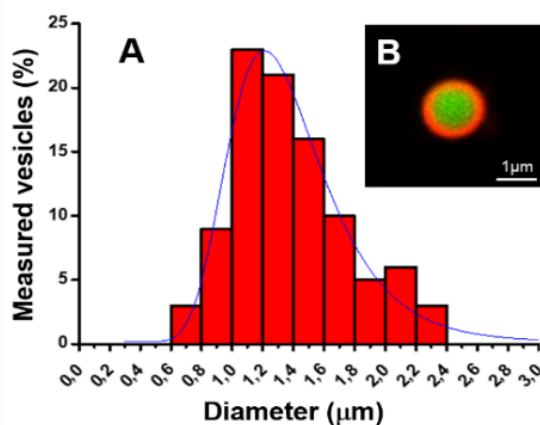


Figure 1. A) Size distribution of fluorescent giant liposomes as measured by acquiring confocal fluorescent microscopy images. B) representative confocal fluorescence microscopy image of a fluorescent spherical giant liposome.

As reported in Figure 1B, the phospholipidic membrane can be easily detected by the presence of rhodamine-B-bearing phospholipids (red) and the inner aqueous cavity can be visualized by the presence of the water soluble 5(6)-carboxyfluorescein (green).

To investigate the potential of giant liposomes as CEST agents (GiantCEST) different formulations were prepared. In particular, small and giant liposomes suspensions containing 40 mM TmHPDO3A (Experimental, Fig. 6) in the aqueous cavity and 15% of amphiphilic Tm-complex (Experimental, Fig.7) in the membrane were prepared and characterized. All the samples were resuspended in HEPES/NaCl 0.15 M buffer 300 mOsm/L to induce an osmotic stress (shrunken liposomes).^{8,18}

Z-spectra were acquired at 600 MHz at different presaturation powers. Z-spectra of small and giant liposome suspensions sharing the same formulation are reported in Figure 2A and B, respectively.

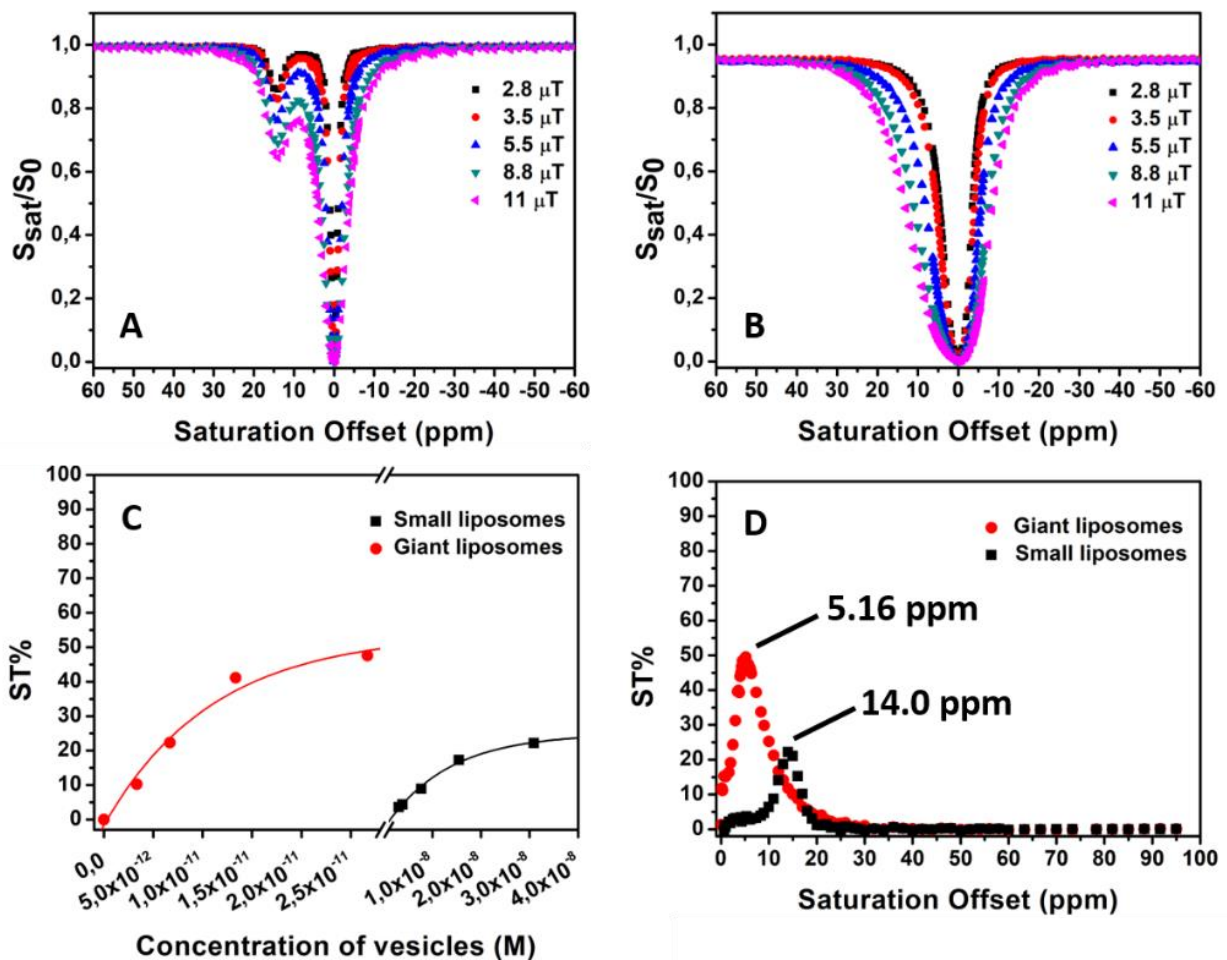


Figure 2. Z-spectra of suspensions containing 3.1×10^{-8} M of small Lipo-1 (A) and 2.7×10^{-11} M of giant Lipo-2 (B) vesicles acquired at 600 MHz at different presaturation powers. C) ST% in function on the concentration of vesicles (calculated) for a Lipo-1 (black squares) and Lipo-2 (red circles) suspension. D) ST% effect in function of the saturation offset for Lipo-1 (black squares) and Lipo-2 (red circles) suspension.

The intensity of the irradiating field B_1 that represented the best compromise between maximizing the LipoCEST efficacy and minimizing SAR (Specific Absorption Rate)²³ issues was $5.5 \mu\text{T}$. At this B_1 value the small liposomes suspension resulted to have a ST% of 22.15% related to a molar concentration of vesicles of 3.1×10^{-8} M whereas the giant liposomes suspension resulted in a ST%

of 47.56% related to a molar concentration of vesicles of 2.7×10^{-11} M. This means that at the same concentration of vesicles, GiantCEST sensitivity is at least three order of magnitude higher with respect to nanosized LipoCEST, as shown in Figure 2C where the ST% is reported as a function of vesicles concentration. It is worth noting that the sensitivity threshold is about 1.5 pM. The enhanced CEST-MRI sensitivity of GUVs with respect to SUVs was clearly assessed by comparing phantoms containing similar concentration of vesicles (*ca.* 7×10^{-11} M). Whereas the SUVs-containing sample did not display any CEST effect, the GUVs-containing one showed a ST% enhancement higher than 50% (Experimental, Fig. 8). Figure 2D displays the saturation transfer peaks measured at $B_1=5.5 \mu\text{T}$.

It is possible to observe that even though giant and small vesicles share the same membrane composition and inner core payload, the corresponding intraliposomal water shift is quite different, *i.e.* 5.16 ppm and 14.0 ppm, respectively. As reported in literature, osmotically stressed small liposomes have a strongly anisotropic cigar-like shape^{8,18,20} and this feature allow them to orient in the main magnetic field, hence exploiting the BMS contribution to the intraliposomal water shifts.²⁰ The BMS contribution is larger with respect to the dipolar one^{24,25} so for these vesicles it is expected to induce a shift larger than 10 ppm.^{18,25} From the obtained results, giant liposomes intraliposomal shift didn't appear to be affected by the BMS contribution to the same extent as it was observed for the small ones.

To get more insight into the understanding of this unexpected behavior, a giant liposome containing 40 mM Dy-HPDO3A in the cavity and 15% amphiphilic Dy-complex in membrane was prepared and characterized. Changing the lanthanide metal ion from Tm(III) to Dy(III) of the amphiphilic complex inserted in the membrane, one goes to vary the sign of the magnetic anisotropy of the phospholipidic membrane.²⁶ In the case of the small shrunken vesicles the analogous Dy/Tm resulted in a dramatic change of their orientation towards the external magnetic field.¹⁸ The evidence that a variation in the orientation has occurred is provided from a change in the sign of the BMS contribution to the shift (from positive to negative). The two formulations of giant vesicles with 15% of amphiphilic Ln-complex in the membrane, where Ln is Tm or Dy, were compared. Figure 3 reports the Z-spectra acquired at 600 MHz at different presaturation powers.

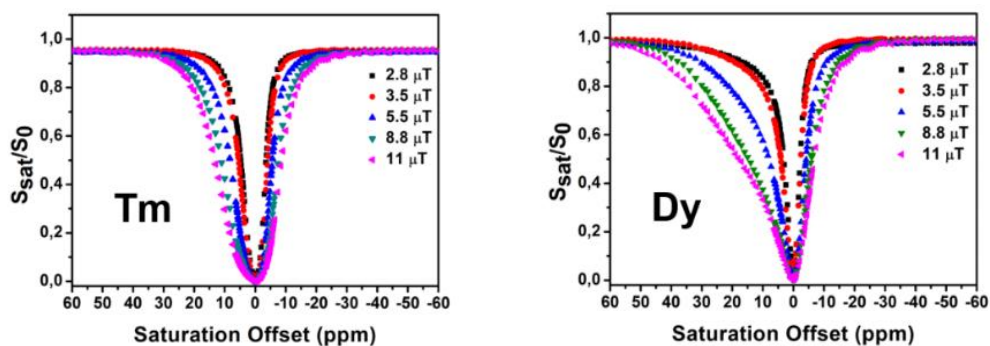


Figure 3. Z-spectra of giant Lipo-2 (left) and giant Lipo-3 (right) suspensions acquired at 600 MHz at different presaturation powers in order to evaluate the BMS contribute.

Surprisingly, in case of giant liposomes containing amphiphilic Tm- or Dy- complexes in the membrane, the chemical shift is positive in both cases, thus suggesting that the change in the orientation observed for the analogous SUVs did not take place.²⁷ This behavior could be explained

hypothesizing that the shape of giant liposomes might not be the same as that observed for the smaller ones.

To investigate this possibility, confocal fluorescence microscopy images were acquired. To be visualized by confocal fluorescence microscopy rhodamine-B-carrying giant liposomes entrapping 5(6)-carboxyfluorescein were prepared. Two different aliquots were put against isotonic and hypertonic HEPES/NaCl buffer to generate a spherical and a shrunken liposomes suspension, respectively. Osmotically stressed nanosized liposomes react towards hypertonic medium changing their spherical shape into a cigar-like shape, as reported in literature.²⁰

In Figure 4A an image of an isotonic giant liposome in which it is possible to appreciate the red burden containing the rhodamine-B and the green internal cavity due to 5(6)-carboxyfluorescein is reported; as expected, the vesicle resulted to be spherical. Figures 4B and 4C report to examples of osmotically stressed GUVs either as two-dimensional or three-dimensional section, respectively.

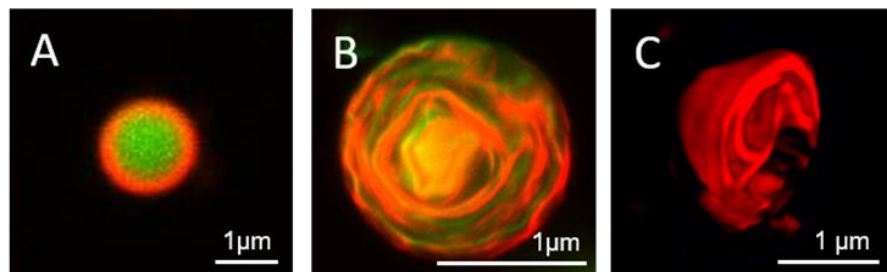


Figure 4. Confocal fluorescence microscopy images of A) a spherical isotonic giant liposome, B) an osmotically stressed globe spiral-like shaped giant liposome C) a 3D section of an osmotically stressed GUV. Both giant formulations contain 0.05% Liss Rhod PE in membrane and 20 μ M 5(6)-carboxyfluorescein in the internal cavity.

It is possible to appreciate the strongly anisotropic but amorphous shape of the vesicle with several invaginations due to the osmotic stress.

In order to evaluate the magnetic behavior of giant liposomes toward progressive osmotic stress, a giant liposomes suspension containing 40 mM TmHPDO3A in the aqueous cavity and 15% of amphiphilic Tm-complex in the membrane was prepared and suspended in HEPES/NaCl with increasing osmolarity from an isotonic to a highly hypertonic environment (40÷400 mOsm/L). In Figure 5, it is clearly visible how the peak of intraliposomal water shifts away from the bulk water upon increasing the osmolarity of the external medium. At the highest osmotic stress, an intraliposomal value of about 30 ppm is reached.

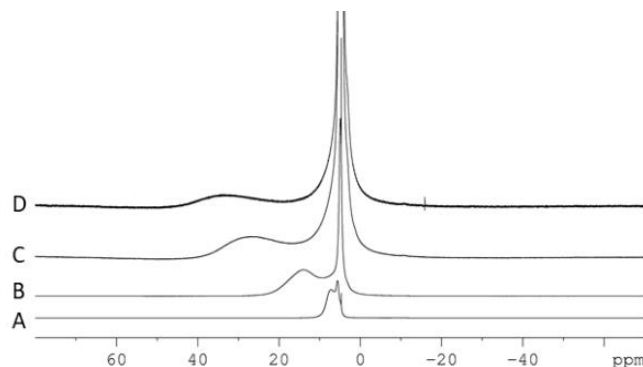


Figure 5. ¹H NMR spectra (600 MHz, 298 K) of a suspension of Lipo-2 suspended in HEPES/NaCl (pH 7.4) with increasing osmolarity: A) 40 mOsm/L (isotonic), B) 150 mOsm/L, C) 300 mOsm/L, D) 400 mOsm/L.

Together with the shift, the osmotic stress also resulted in a decrease of the intraliposomal water signal, which is associated with a line broadening of the peak. The decrease in the signal intensity is the consequence of the osmotic shrinkage of the vesicle that, besides losing entrapped water, increases the concentration of the paramagnetic molecules in the aqueous core, thus leading to the shortening of the T_2 relaxation time, responsible for the broadening of the peak.²⁰

Finally, insights into the compatibility of using GUVs as an alternative to SUVs for future *in vivo* applications have been gained by *in vitro* experiments on cellular systems. In particular, it has been found that *i)* internalization of GUVs by macrophages is markedly lower than the one reported for SUVs (Experimental, Fig. 9 and Fig. 10) and *ii)* cells viability in presence of GUVs is very similar to the one reported for SUVs (Experimental, Fig. 11). These findings make GUVs potential good candidates as CEST MRI CAs for *in vivo* preclinical applications.

Conclusions

The herein reported results show that paramagnetically loaded GUVs display a CEST sensitivity enhancement of three order of magnitude in respect to analogous LipoCEST agents based on nanosized SUVs. Interestingly this expected change does not occur as simple follow-up of the difference in size between SUVs and GUVs because their response to the osmotic changes resulted quite different. Actually, the changes induced on liposomes by osmotic shrinkage is a topic extensively investigated over the years as the effects of changes in osmotic pressure on liposomes membrane have been used to mimic the transformation of biological membranes in response to a number of environmental factors. The changes induced on liposomes by osmotic shrinkage have been investigated by means of many techniques (TEM, SAXS, Fluorescent microscopy, etc.). In general, it has been found that, after the initial decrease of the area/lipid ratio, a variety of deformations may occur including the increase of membrane area, phase shrinkage, up to partial solubilization or pore formation and fusion. The osmotic shrinkage is first driven by the water outflow through the bilayer. The decrease in size implies a decrease of the area/lipid ratio which is accommodated with a deformation that for the small SUVs results in a passage from spherical to lens/cigar-shaped ones. Likely in the case of GUVs the deformation results in close contact of opposite bilayers which yield to an extensive rearrangement that, in turn, appears to lead to a multilamellar system. However, we cannot exclude that the multi-lamellar structure is the result of an extensive breaking of the liposome membrane in response to the increased osmotic pressure. It was reported that under osmotic stress, the vesicles are often broken and large holes open without membrane shrinking.²⁸

As far as concern the development of new MRI CEST agents, the finding that such paramagnetically labelled multilamellar-structures yields systems analogous to the previously reported LipoCEST agents may open new routes for the design of innovative contrast agents. In addition to the markedly enhanced sensitivity displayed by these systems in comparison with the previously reported LipoCESTs, *in vitro* experiments showed a very limited uptake of GUVs from macrophages. This finding appears very promising in terms of overcoming issues that hampered LipoCESTs *in vivo* applications.

Experimental

Chemicals: Gd-HPDO3A was provided by Bracco Imaging S.p.A. (Colleretto Giacosa (TO), Italy). The synthesis of Tm(III)- and Dy(III)-complexes (Figure 6) was carried out mixing the lanthanide oxide Ln_2O_3 and the ligand HPDO3A (1:2 molar ratio) in water. The mixture has been let to react for two weeks under stirring and heating at 80°C .

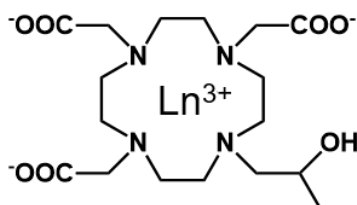


Figure 6. Chemical structure of LnHPDO3A where Ln^{3+} is Tulum or Dysprosium and HPDO3A is 10-(2-hydroxypropyl)-1,4,7,10-tetraazacyclododecane-1,4,7-triacetic acid.

Amphiphilic Ln-complexes (Figure 7) were synthesized according to the procedure reported in the literature for the Gd(III) analogue.²⁹

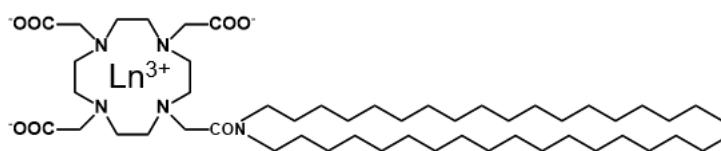


Figure 7. Chemical structure of Amphiphilic Ln-complexes used in this work where Ln^{3+} is Tulum or Dysprosium.

For all the synthesized complex, the purity of the compounds was around 80-90% as evaluated by measuring the Bulk Magnetic Susceptibility (BMS) shifts of ^1H NMR resonance signals of solution (*tert*-butanol in water) containing the compound with respect to the same solution without paramagnetic compound (Evans' Method).³⁰

Free Ln-ions has been checked to be lower than 0.3% mol/mol as assessed by applying the Orange xlenol procedure.³¹

1,2-dipalmitoyl-*sn*-glycero-3-phosphocholine (DPPC), 1,2-distearoyl-*sn*-glycero-3-phosphoethanolamine-N-[methoxy(polyethylene glycol)-2000] (ammonium salt) (DSPE-mPEG2000), 1,2-dioleoyl-*sn*-glycero-3-phosphoethanolamine-N-(lissamine rhodamine B sulfonyl) (ammonium salt) (Liss Rhod PE) were purchased from Avanti Polar Lipids Inc.

Sodium chloride, HEPES (4-(2-hydroxyethyl)-1-piperazineethane-sulfonic acid), sodium hydroxide, hydrochloric acid, 5(6)-carboxyfluorescein, chloroform and all the other chemicals were acquired from Sigma Aldrich Co. LLC.

Liposomes preparation and characterization: Giant liposomes were prepared according to a procedure reported in literature with some modifications.²² The suitable mixture of phospholipids (0.0224 mmol) dissolved in chloroform is distributed on the bottom of a 2 L Erlenmeyer flask and it is dried for 15 minutes with a flux of inert gas (Argon). The hydration solution (25 mL) is then carefully added and the flask is set for 2 h at 60°C without any mechanical stress. Next, the flask is mildly swirled, the cloudy suspension recuperated and cooled to room temperature. The

suspension is centrifuged 30 minutes at 6500 rpm in a fixed 45° angle centrifuge with the purpose of purifying the giant liposomes from impurities and small liposomes populations eventually present. The supernatant is removed, fresh HEPES/NaCl buffer is added and 4 cycles of centrifugation and resuspension are accomplished in order to extensively wash the giant vesicles. The size of giant liposomes was characterized by fluorescence microscopy images and a suspension of giant liposomes of DPPC/Liss Rhod PE/DSPE-mPEG2000 96.95/0.05/3 molar ratio membrane and 20 μM 5(6)-carboxyfluorescein in the aqueous phase was produced for this goal. Z-stack images were acquired on a Leica SP8 confocal system (Leica Microsystems) in order to centre every vesicle in its main diameter to be appropriately measured. The following wavelengths were considered for the microscopy visualization: 1) $\lambda^{\text{ex}}=492$ nm, $\lambda^{\text{em}}=517$ nm for 5(6)-carboxyfluorescein, 2) $\lambda^{\text{ex}}=545$ nm, $\lambda^{\text{em}}=567$ nm for rhodamine-B. The size distribution of giant vesicles was fitted with Landau function. Dynamic Light Scattering (DLS) measurements were obtained at 298 K (Zetasizer NanoZS, Malvern, UK) to ensure there was no evidence of populations of liposomes between 50 nm and 800 nm.

Small liposomes were prepared by using the usual thin lipidic film method.³² Briefly, the desired mixture of phospholipids dissolved in chloroform is slowly evaporated to take off the solvent, until a thin film is formed on a round bottom flask. The film is then hydrated at 55°C with the hydration solution (1 mL). The resulting suspension of multilamellar vesicles is extruded (Lipex extruder, Northern Lipids Inc., Canada) four times on polycarbonate filters with a pore diameter of 400 nm and six times on polycarbonate filters with a pore diameter of 200 nm. The final suspension of vesicles was purified from the non-encapsulated metal complex by exhaustive dialysis carried out at 4°C against HEPES/NaCl buffer. The vesicles were characterized by using DLS to define the mean hydrodynamic diameter and the polydispersity of the system.

The molar concentration of small and giant vesicles was evaluated by using the following relation [Eq. (1)]:

$$[Liposomes] = \frac{[Ln]_{TOT} \times 1 L}{V_i \times [Ln]_{intra\text{lipo}}} = \frac{[Ln]_{TOT} \times 1 L}{\frac{4}{3}\pi r^3 \times [Ln]_{intra\text{lipo}}} \quad (1)$$

where $[Ln]_{TOT}$ is determined by Evans' method,³⁰ r is the radius of the vesicle and $[Ln]_{intra\text{lipo}}$ is assumed to be the same of the hydration solution.²⁷

Chemical Exchange Saturation Transfer measurements: $\Delta_{intra\text{lipo}}$ values were measured at 298 K on a Bruker Avance 600 spectrometer operating at 14.1 T by taking the shift difference between the intraliposomal and *bulk* water protons. The liposomes suspensions were put in a capillary coaxially inserted in a 5 mm NMR tube containing D₂O as the lock solvent. Z-spectra were acquired using a 2D noediff.2 sequence with different presaturation powers ($B_1=2.8$ μT, 3.5 μT, 5.5 μT, 8.8 μT, 11 μT), irradiation time of 1 second and a frequency offset range of $\delta\pm 60$ ppm. The ST% values were calculated by using the following relation [Eq. (2)]:

$$ST\% = \left(1 - \frac{I^\omega}{I^{-\omega}}\right) \times 100$$

(2)

in which I^{ω} and $I^{-\omega}$ refer to the *bulk* water signal intensity at two frequency offsets (ω and $-\omega$) symmetrically distributed with respect to the zero offset of the *bulk* water resonance. ω is the frequency offset corresponding to the resonance of the intraliposomal water protons (i.e., corresponding to $\Delta_{\text{intralipo}}$).

CEST-MRI of phantom containing GUVs and SUVs: Representative CEST-MR image of phantom containing GUVs and SUVs was acquired on two suspensions containing SUVs and GUVs at 7.28×10^{-11} M concentration, respectively. Z-spectra were acquired at 21°C, 7.1 T on a Bruker Avance 300 spectrometer equipped with a microimaging probe. A frequency offset range of ± 50 ppm was investigated. A typical RARE spin-echo sequence with TE= 3 ms, TR= 5 s and RF= 4 was used. An isotropic 64×64 acquisition matrix with a FOV of 10 mm and a slice thickness of 1 mm was used. The whole sequence was preceded by a saturation scheme consisting of a continuous rectangular wave pulse 2 s long with a radiofrequency B_1 field of 6 μ T. The Z-spectra was interpolated by smoothing splines to identify the zero-offset on a pixel-by-pixel basis of the bulk water and, then, to assess the correct ST% value over the entire range of frequency offsets investigated. Custom-made software, compiled in the Matlab platform (Mathworks Inc., Natick, MA), was used. The extent of CEST effect is calculated as follows:

$$ST\% = \left(1 - \frac{M_S}{M_0}\right) \times 100$$

where M_S is the intensity of the bulk water NMR signal after the irradiation on resonance ($\Delta\omega$) of the mobile proton pool and M_0 is the intensity of the bulk water NMR signal after the irradiation at the opposite frequency ($-\Delta\omega$).

CEST-MR image was obtained by mapping the ST% effect both at 7 (Figure 8) and 14 ppm. The CEST effect could be detected only for GUVs.

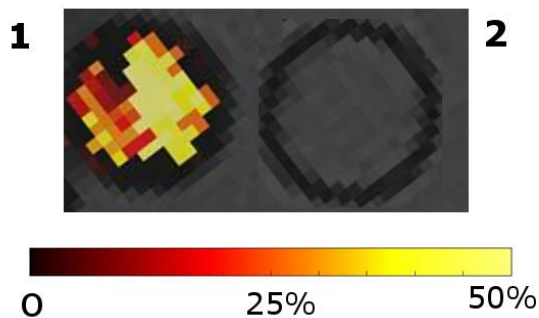


Figure 8. Representative CEST-MR image ($\Delta\delta = 7$ ppm) of glass tubes containing GUVs (sample 1) or SUVs (sample 2), respectively. [Vesicles] is 7.28×10^{-11} M.

Assessment of macrophage uptake of GUVs and SUVs: Preliminary experiments aimed at comparing GUVs and SUVs uptake from macrophages were carried using murine J774A.1 macrophage cells. For this purpose, two different tests were carried out.

In the first set of experiments, J774A.1 cells were incubated in the presence of GUVs or SUVs (for both systems the actual concentration of metal complex in the considered suspension volume was 100 μM) for variable times (0.5, 1 or 2 h). At the end of the incubation period, the cells were washed three times with fresh PBS, mechanically detached with the cell scraper, collected and pelleted by centrifugation (1200 rpm, 5 min). Then, the cellular pellets were re-suspended in fresh PBS and lysed by sonication in an ice containing bath (30 s, 30% of power by using a Bandelin Sonoplus sonicator operating at 20 KHz). The total number of cells was assessed via the quantification of the total protein content by the Bradford assay (1 mg of proteins corresponds to 2.5×10^6 J774A.1 cells)³³. Finally, the amounts of internalized liposomes (GUVs or SUVs) were assessed on the basis of the quantification of the total metal content by ICP-MS. For this purpose, specimens were digested by addition of concentrated HNO_3 (70%) and microwave heating (Milestone MicroSYNTH, Microwave lab station equipped with an optical fiber temperature control and HPR-1000/6M six position high-pressure reactor, Bergamo, Italy). After digestion, the volume of each sample was brought to 2 mL with ultrapure water and analyzed by ICP-MS, using a Thermo Scientific ELEMENT 2 ICP-MS-Finnigan, Rodano (MI) to measure the Gd concentrations. By knowing the total moles of Gd entrapped in each liposome (GUV or SUV) and the total moles of Gd for cell, it is possible to calculate the total number of liposomes entrapped inside cells. Results are reported as Figure 9. The internalization of metal complex is much higher by using SUVs in comparison to GUVs. This reports about a lower internalization efficiency of GUVs.

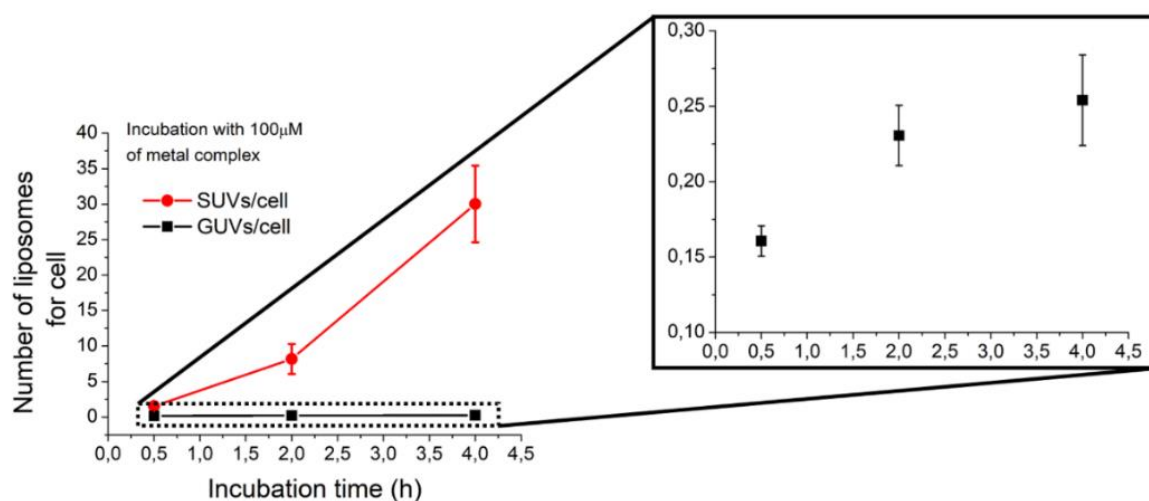


Figure 9. Assessment of the cellular uptake of GUVs and SUVs by J774A.1 macrophages in function of the incubation time. The overall concentration in the incubation medium of Gd-HPDO3A entrapped in the liposomal vesicles is 0.1 mM.

In order to double check the occurrence of the largely enhanced internalization of SUVs in comparison to GUVs, an analogous macrophagic uptake experiment was carried out using fluorescently labelled liposomes with the acquisition of confocal fluorescence microscopy images. For this purpose, 1.5×10^4 J774A.1 cells were seeded into μ -Slide 8 well in presence of complete medium. The day after, the cellular suspensions were added with carboxyfluorescein-labelled SUVs or GUVs (green) (*ca.* 5×10^6 vesicles *per* plate). After 30', the cells were extensively and gently

washed to remove non-internalized liposomes and stained with Vybrant™ DiD Cell-Labeling Solution (blue) to be visualized by confocal microscopy.

Confocal microscopy images were carried out by using a Leica SP8 confocal system (Leica Microsystems). The following wavelengths were considered for the microscopy visualization: 1) $\lambda^{\text{ex}}=492$ nm, $\lambda^{\text{em}}=517$ nm for 5(6)-carboxyfluorescein (*green*), 2) $\lambda^{\text{ex}}=644$ nm, $\lambda^{\text{em}}=665$ nm for Vybrant™ DiD (*blue*).

As reported in Figure 10A, when cells were incubated in presence of SUVs, an extensive internalization of carboxyfluorescein took place. This is detectable as a strong green signal (Figure 10A) which is mainly compartmentalized inside endosomes-like vesicles but in part also diffuses in the cytoplasmic region. On the contrary, when cells were incubated in the presence of GUVs, a negligible internalization of carboxyfluorescein occurred (Figure 10B).

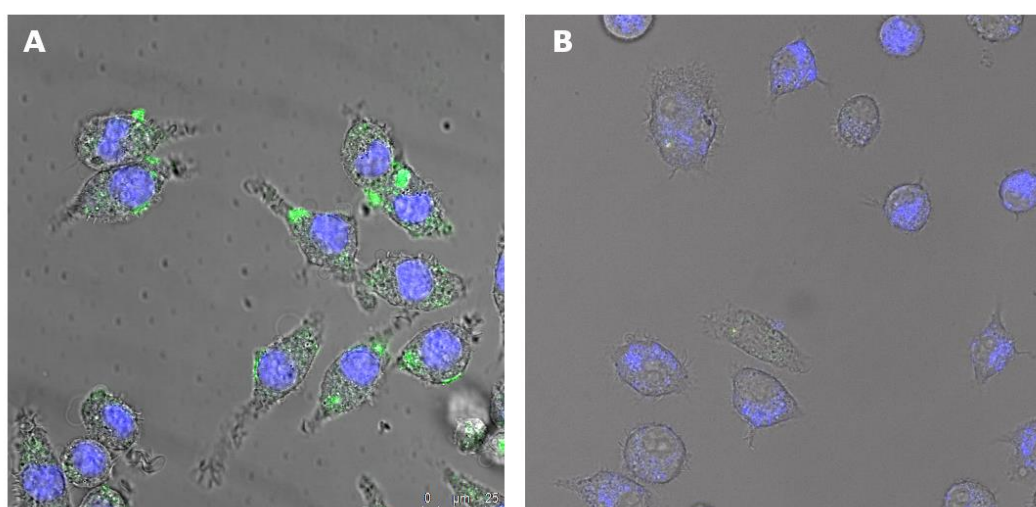


Figure 10. Confocal fluorescent microscopy images of J774A.1 cells after incubation in presence of carboxyfluorescein loaded-SUVs (A, left) or GUVs (B, right) Blue: J774A.1 cells stained with Vybrant™ DiD Cell-Labeling Solution; Green: Carboxyfluorescein loaded in the liposomes.

Cytotoxicity assay: Preliminary tests to assess the eventual toxicity of GUVs were carried out by using IGROV-1 human ovarian cancer cells and applying MTT assay (Figure 11). IGROV-1 human ovarian carcinoma cells were obtained from American Type Culture Collection (ATCC, Manassass, VA). They were grown in RPMI¹⁰⁶⁴ supplemented with 10% (v/v) heat-inactivated fetal bovine serum (FBS), 2 mM glutamine, 100 U/ml penicillin and 100 mg/ml streptomycin (purchased from Lonza Sales AG, Verviers, Belgium). Cells were seeded in 75-cm² flasks at density of *ca.* 2×10⁴ cells/cm² in a humidified 5% CO₂ incubator at 37°C. When cells reached confluence, they were detached by adding 1 ml of Trypsin-EDTA solution (0.25 % w/v Trypsin-0.53 mM EDTA). Cells were negative for mycoplasma as tested by using MycoAlert™ Mycoplasma Detection Kit by Lonza (Lonza Sales AG, Verviers, Belgium). For cytotoxicity assay, IGROV-1 cells were seeded into 96-well tissue culture plate (10⁴ cells for plate) 24 h before the experiment. Then, they were incubated with fresh complete RPMI medium in presence of Gd-HPDO3A-containing-GUVs or –SUVs. In particular, increasing amounts of GUVs or SUVs were tested, both in terms of concentration of vesicles (0 ÷ 15 pM) and concentration of Gd-complex (0 ÷ 3.7 mM). After the incubation time,

medium was removed, cells washed and re-incubated in presence of fresh RPMI medium supplemented with 0.5 mg/ml MTT (Thiazolyl Blue Tetrazolium Bromide, Sigma Aldrich) for 4 h in a humidified 5% CO₂ incubator at 37°C. Then, MTT solution was removed and plates were filled with DMSO (0.1 mL for plate) for ½ h at room temperature, under gentle agitation, for allowing solubilization of formazan crystals. The absorbance of the resulting colored solutions was quantified using a 96-multiwell iMark Bio-Rad microplate Reader (λ= 570nm). The percentage of viable cells was calculated on the basis of control blank cells by using the following formula:

$$Viable\ cells\ \% = \frac{Abs_T}{Abs_{cnt}} \times 100$$

where Abs_T is the mean absorbance of treated cells and Abs_{cnt} is the mean absorbance of control untreated cells (after subtraction of absorption of empty plates as background).

Cells experiments were repeated in triplicate and data reported as mean ± standard deviation. Blank was repeated 10 times.

Results are reported as Figure 11. GUVs display a cellular toxicity well comparable to the one shown by SUVs. Cells viability, in the presence of GUVs or SUVs is higher than 80% for all tested concentrations. This observation is indicative of a good biocompatibility of GUVs, comparable to the one reported for SUVs.

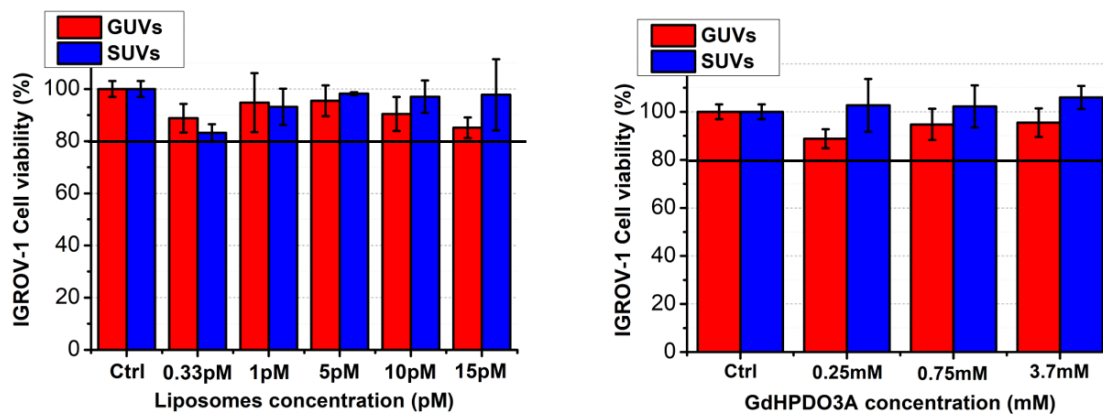


Figure 11. Assessment of IGROV-1 ovarian cancer cells viability upon the incubation with GdHPDO3A-containing GUVs and SUVs. (Left) Increasing concentrations of GUVs and SUVs in the cells containing medium (0 ÷ 15 pM). (Right) Increasing concentrations of GdHPDO3A in GUVs and SUVs incubated in the cells containing medium (0 ÷ 3.7 mM).

References

1. Merbach, A. S., Helm, L., & Toth, E. (2013). *The chemistry of contrast agents in medical magnetic resonance imaging*. John Wiley & Sons.
2. Caravan, P. (2006). Strategies for increasing the sensitivity of gadolinium based MRI contrast agents. *Chemical Society Reviews*, 35(6), 512-523.
3. Geraldes, C. F., & Laurent, S. (2009). Classification and basic properties of contrast agents for magnetic resonance imaging. *Contrast media & molecular imaging*, 4(1), 1-23.
4. De León-Rodríguez, L. M., Martins, A. F., Pinho, M. C., Rofsky, N. M., & Sherry, A. D. (2015). Basic MR relaxation mechanisms and contrast agent design. *Journal of Magnetic Resonance Imaging*, 42(3), 545-565.
5. Sherry, A. D., Caravan, P., & Lenkinski, R. E. (2009). Primer on gadolinium chemistry. *Journal of Magnetic Resonance Imaging: An Official Journal of the International Society for Magnetic Resonance in Medicine*, 30(6), 1240-1248.
6. Lacerda, S., & Tóth, É. (2017). Lanthanide complexes in molecular magnetic resonance imaging and theranostics. *ChemMedChem*, 12(12), 883-894.
7. Srivastava, K., Ferrauto, G., Young Jr, V. G., Aime, S., & Pierre, V. C. (2017). Eight-coordinate, stable Fe (II) complex as a dual ¹⁹F and CEST contrast agent for ratiometric pH imaging. *Inorganic chemistry*, 56(20), 12206-12213.
8. Ferrauto, G., Aime, S., McMahon, M. T., Morrow, J. R., Snyder, E. M., Li, A., & Bartha, R. (2017). Chemical exchange saturation transfer (CEST) contrast agents. In *Contrast Agents for MRI* (pp. 243-317).
9. Van Zijl, P. C., & Yadav, N. N. (2011). Chemical exchange saturation transfer (CEST): what is in a name and what isn't?. *Magnetic resonance in medicine*, 65(4), 927-948.
10. Jones, K. M., Pollard, A. C., & Pagel, M. D. (2018). Clinical applications of chemical exchange saturation transfer (CEST) MRI. *Journal of Magnetic Resonance Imaging*, 47(1), 11-27.
11. Vinogradov, E., Sherry, A. D., & Lenkinski, R. E. (2013). CEST: from basic principles to applications, challenges and opportunities. *Journal of magnetic resonance*, 229, 155-172.
12. Ferrauto, G., Delli Castelli, D., Di Gregorio, E., Terreno, E., & Aime, S. (2016). LipoCEST and cellCEST imaging agents: opportunities and challenges. *Wiley Interdisciplinary Reviews: Nanomedicine and Nanobiotechnology*, 8(4), 602-618.

13. Ferrauto, G., Carniato, F., Tei, L., Hu, H., Aime, S., & Botta, M. (2014). MRI nanoprobe based on chemical exchange saturation transfer: Ln III chelates anchored on the surface of mesoporous silica nanoparticles. *Nanoscale*, 6(16), 9604-9607.
14. Aime, S., Delli Castelli, D., & Terreno, E. (2005). Highly sensitive MRI chemical exchange saturation transfer agents using liposomes. *Angewandte Chemie International Edition*, 44(34), 5513-5515.
15. Chahid, B., Vander Elst, L., Flament, J., Boumezbeur, F., Medina, C., Port, M., ... & Lesieur, S. (2014). Entrapment of a neutral Tm (III)-based complex with two inner-sphere coordinated water molecules into PEG-stabilized vesicles: towards an alternative strategy to develop high-performance LipoCEST contrast agents for MR imaging. *Contrast media & molecular imaging*, 9(6), 391-399.
16. Zhao, J. M., Har-el, Y. E., McMahon, M. T., Zhou, J., Sherry, A. D., Sgouros, G., ... & Van Zijl, P. C. (2008). Size-induced enhancement of chemical exchange saturation transfer (CEST) contrast in liposomes. *Journal of the American Chemical Society*, 130(15), 5178-5184.
17. Chan, K. W., Bulte, J. W., & McMahon, M. T. (2014). Diamagnetic chemical exchange saturation transfer (diaCEST) liposomes: physicochemical properties and imaging applications. *Wiley Interdisciplinary Reviews: Nanomedicine and Nanobiotechnology*, 6(1), 111-124.
18. Terreno, E., Cabella, C., Carrera, C., Delli Castelli, D., Mazzon, R., Rollet, S., ... & Aime, S. (2007). From spherical to osmotically shrunken paramagnetic liposomes: an improved generation of LIPOCEST MRI agents with highly shifted water protons. *Angewandte Chemie International Edition*, 46(6), 966-968.
19. Burdinski, D., Pikkemaat, J. A., Emrullahoglu, M., Costantini, F., Verboom, W., Langereis, S., ... & Huskens, J. (2010). Targeted lipoCEST contrast agents for magnetic resonance imaging: alignment of aspherical liposomes on a capillary surface. *Angewandte Chemie International Edition*, 49(12), 2227-2229.
20. Aime, S., Castelli, D. D., & Terreno, E. (2009). Lanthanide-loaded paramagnetic liposomes as switchable magnetically oriented nanovesicles. *Methods in enzymology*, 464, 193-210.
21. Deissler, V., Rüger, R., Frank, W., Fahr, A., Kaiser, W. A., & Hilger, I. (2008). Fluorescent liposomes as contrast agents for in vivo optical imaging of edemas in mice. *Small*, 4(8), 1240-1246.
22. Reeves, J. P., & Dowben, R. M. (1969). Formation and properties of thin-walled phospholipid vesicles. *Journal of cellular physiology*, 73(1), 49-60.

23. Roeloffs, V., Meyer, C., Bachert, P., & Zaiss, M. (2015). Towards quantification of pulsed spinlock and CEST at clinical MR scanners: an analytical interleaved saturation–relaxation (ISAR) approach. *NMR in Biomedicine*, 28(1), 40-53.
24. Ferrauto, G., Di Gregorio, E., Baroni, S., & Aime, S. (2014). Frequency-encoded MRI-CEST agents based on paramagnetic liposomes/RBC aggregates. *Nano letters*, 14(12), 6857-6862.
25. Peters, J. A., Huskens, J., & Raber, D. J. (1996). Lanthanide induced shifts and relaxation rate enhancements. *Progress in Nuclear Magnetic Resonance Spectroscopy*, 28(3-4), 283-350.
26. Ferrauto, G., Delli Castelli, D., Di Gregorio, E., Langereis, S., Burdinski, D., Gröll, H., ... & Aime, S. (2014). Lanthanide-loaded erythrocytes as highly sensitive chemical exchange saturation transfer MRI contrast agents. *Journal of the American Chemical Society*, 136(2), 638-641.
27. Ferrauto, G., Di Gregorio, E., Ruzza, M., Catanzaro, V., Padovan, S., & Aime, S. (2017). Enzyme-Responsive LipoCEST Agents: Assessment of MMP-2 Activity by Measuring the Intra-liposomal Water ¹H NMR Shift. *Angewandte Chemie*, 129(40), 12338-12341.
28. Ohno, M., Hamada, T., Takiguchi, K., & Homma, M. (2009). Dynamic behavior of giant liposomes at desired osmotic pressures. *Langmuir*, 25(19), 11680-11685.
29. Anelli, P. L., Lattuada, L., Lorusso, V., Schneider, M., Tournier, H., & Uggeri, F. (2001). Mixed micelles containing lipophilic gadolinium complexes as MRA contrast agents. *Magnetic Resonance Materials in Physics, Biology and Medicine*, 12(2-3), 114-120.
30. Corsi, D. M., Platas-Iglesias, C., Bekkum, H. V., & Peters, J. A. (2001). Determination of paramagnetic lanthanide (III) concentrations from bulk magnetic susceptibility shifts in NMR spectra. *Magnetic Resonance in Chemistry*, 39(11), 723-726.
31. Barge, A., Cravotto, G., Gianolio, E., & Fedeli, F. (2006). How to determine free Gd and free ligand in solution of Gd chelates. A technical note. *Contrast media & molecular imaging*, 1(5), 184-188.
32. V. P. Torchilin, V. Weissig, in *Liposomes: Practical Approach*, (2003). Oxford University Press, NY, USA, 2nd ed., pp. 4-7.
33. Di Gregorio, E., Ferrauto, G., Gianolio, E., & Aime, S. (2013). Gd loading by hypotonic swelling: an efficient and safe route for cellular labeling. *Contrast media & molecular imaging*, 8(6), 475-486.

- Chapter 3-

**Challenging the Sensitivity of Imaging Probes Targeting
Epitopes on the External Surface of Cellular Membranes**

Martina Tripepi, Giuseppe Ferrauto, Paolo Oronzo Bennardi, Silvio Aime and Daniela Delli Castelli*

Submitted

Abstract

Targeting of receptors on the outer surface of cells is a task of outstanding importance. Herein, folate-functionalized giant (microsized) liposomes have been developed. They efficiently bind the external surface cells, without internalization. Both confocal fluorescence microscopy and MRI have been employed for detecting giant liposomes, upon proper loading with fluorescent dyes or paramagnetic compounds, respectively. Confocal Images displays that folate-functionalized GUVs selectively recognize the receptors at the surface of the target cells and appears clustered in a defined region of the cellular membrane. MRI study revealed a significant T_2^* contrast between labeled and unlabelled cells with paramagnetically loaded folate-functionalized giant liposomes.

Introduction

In the era of molecular medicine, it is highly relevant to develop imaging probes able to reveal a pathological condition. MRI stands out for the superb spatial resolution but the available contrast enhancers lack in sensitivity.

It is well established that one of the consequences of the limited sensibility of MRI targeting probes implies their accumulation at the targeted site.¹ On the basis with the common practice with nuclear medicine tracers, this task is often accomplished by pursuing the internalization of the imaging probes inside the targeting cells.² However, the number of molecular imaging probes that are required in order to visualize a single cell by MRI is very high. It was early reported that, in the case of paramagnetic T₁-relaxation Gd-containing enhancers, this number is of the order of 10⁸ *per cell*.^{2,3}

The use of Iron Oxide superparamagnetic particles (SPIO) as T₂ agents results in an improvement of the sensitivity.^{4,5} However, in terms of number of iron atoms *per cell*, the use of SPIOs leads to the cellular entrapment of a number of metal ions that is in an analogous order of magnitude the ones needed for T₁-visualization. The large number of metal ions that need to be internalized into cells has strongly limited the clinical translation of MRI cellular agents. The intracellular accumulation of such large payloads of metal containing species does not appear compatible with the maintenance of the physiological functions of the targeted cells. Therefore, in MRI, one needs to pursue strategies that allow the visualization of diseased tissues without requiring the internalization of the imaging probes.

In this context much work has been done by targeting epitopes in the extracellular matrix.⁶⁻¹⁰ However, targeting of receptors on the outer surface of the cellular membrane is still of huge interest because this approach offers the link to relate molecular information associated to the cellular transformation to *in vivo* imaging detection.

Herein, we report our observations aimed at tackling the issue of sensitivity threshold for MRI cellular detection by targeting Folate Receptors (FRs) on IGROV-1 cells. To avoid the internalization step, as FRs are known to yield receptor-mediated endocytosis,¹¹ we made use of Giant Unilamellar Vesicles (GUV)¹² endowed with the proper payload of imaging reporters. GUVs have a mean diameter of 1-2 micron, *i.e.* much larger than the largely used liposomes (endowed with diameters in the range of 100-200 nanometers) often referred as Small Unilamellar Vesicles (SUV). The latter systems have been shown to be efficiently taken up by cells upon their binding to the targeted receptors.¹³ Larger systems as GUVs are expected to not undergo the process of endocytosis.

Results and discussion

GUVs and SUVs were prepared as previously reported with some modifications.^{12,14} The loading of magnetic and fluorescent imaging reporters was carried out by adding the selected molecule to the hydration medium (for encapsulation in the inner aqueous cavity) and to the lipidic phase (for the incorporation in the liposomal membrane).

Figure 1 reports the confocal microscopic image of a GUV containing rhodamine in the membrane and carboxyfluorescein in the inner aqueous cavity.

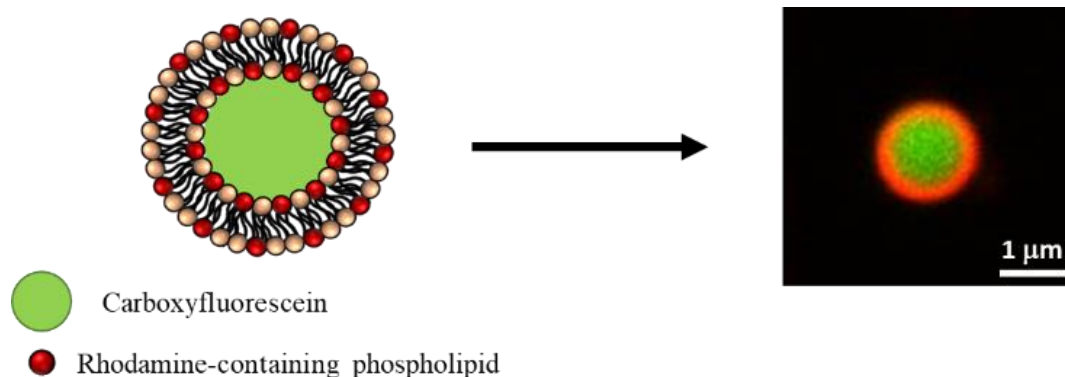


Figure 1. Representative confocal fluorescence microscopy image of a fluorescent GUV; the red burden of the particle represents the rhodamine-labelled membrane whereas the green inside is due to carboxyfluorescein in the aqueous phase of the inner cavity.

Magnetic labelling was carried out by encapsulating Gd-HPDO3A (Gadoteridol, clinically approved as ProHance, Bracco Imaging srl) in the aqueous cavity at the concentration of 300 mM. T_1 -relaxivity (per Gd) resulted to be equal to $1.04 \text{ mM}^{-1}\text{s}^{-1}$ at 0.5 T, *i.e.* much lower than the value reported for Gd-HPDO3A solutions ($4.6 \text{ mM}^{-1}\text{s}^{-1}$)¹⁵. This result was accounted in terms of a limited water exchange across the liposomal membrane thus leading to a substantial "quenching" of the observed relaxivity. It follows that these Gd-loaded GUVs could not have been used as T_1 -relaxation agents.

Conversely, the same Gd-loaded GUVs act as excellent T_2^* agents because of the marked change of the magnetic susceptibility associated to the large size of these highly loaded paramagnetic vesicles.¹⁶ The r_2^* (*per Gd*) resulted to be $6.19 \text{ mM}^{-1}\text{s}^{-1}$ at 0.5 T and $60.76 \text{ mM}^{-1}\text{s}^{-1}$ at 7 T, at room temperature, respectively. For comparison, SUVs with the same Gd-HPDO3A concentration in the inner aqueous cavity yielded r_2^* (*per Gd*) of $0.52 \text{ mM}^{-1}\text{s}^{-1}$ and $10.16 \text{ mM}^{-1}\text{s}^{-1}$ at 0.5 and 7 T, respectively.

The folate-targeting vector was introduced by including a small fraction of properly functionalized phospholipid (DSPE-PEG2000-Folate) in the lipidic phase of the liposome. The targeting moiety is conjugated to a long chain PEG spacer that is covalently bound to the phosphoester moiety of the phosphatidylcholine component.

IGROV-1 human cancer cells were chosen for testing folate-functionalized GUVs because of their overexpression of folate receptors.¹⁷

First, confocal fluorescent microscopy images of targeted fluorescent GUVs incubated cells were acquired. As reported in Figure 2A, rhodamine- (in the membrane) and carboxyfluorescein- (in the inner cavity) loaded GUVs recognize the folate receptors on the outer surface of the IGROV-1 cells but their large size does not allow to proceed along the internalization pathway.

The specificity of the binding has been assessed by two control experiments: i) an excess of free folate ($2.5 \text{ }\mu\text{M}$) was added to the incubation medium. As expected, the binding of the folate-functionalized GUVs to folate receptors appears largely hampered (Figure 2B), ii) the incubation of cells was carried out with GUVs deprived of the targeting moiety. No evidence of the presence of fluorescent materials at the cells' surface was detected (Figure 2C).

The obtained results clearly showed that the folate-functionalized GUVs behave very differently from the analogously functionalized SUVs which enter the cells by receptor-mediated endocytosis.¹⁸ Figure 2A clearly shows that folate-functionalized GUVs selectively recognize the receptors at the surface of the target cells. FRs appears clustered in a defined region of the cellular membrane. Likely this region is rich in caveolae that, in the case of smaller systems, are committed to initiate the endocytic process.¹⁹

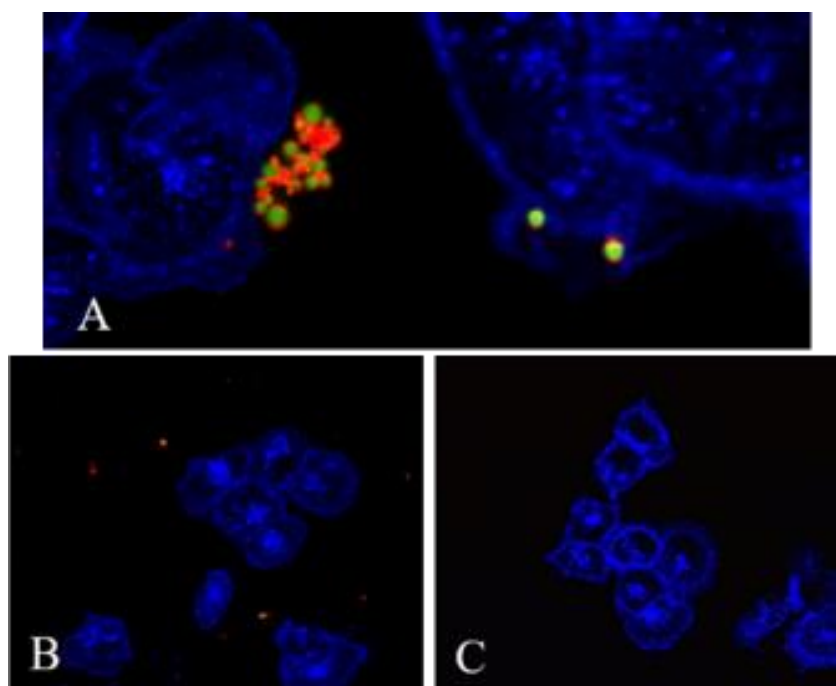


Figure 2. Confocal fluorescent microscopy images of A) folate-targeted fluorescent GUVs bound to IGROV-1 cancer cells in folate-free cell medium, B) folate-targeted fluorescent GUVs incubated with IGROV-1 cancer cells in presence of folate-containing cell culture medium, C) untargeted fluorescent GUVs incubated with IGROV-1 cancer cells in presence of folate-free cell culture medium. Cells were stained in blue with Vybrant™ DiD dye (Experimental).

Herein, caveolae (50-60 nanometer plasma membrane invaginations) cannot afford their natural function and the functionalized GUVs remain just anchored at the receptor sites on the outer space of the cellular membrane. From these observations we draw the conclusion that these GUV-based systems represent a useful model for investigating the MR imaging reporting capabilities of paramagnetic probes that label the cells remaining on their external side (thus not interfering with the intracellular machinery).

The above described binding protocol was replicated for the MRI assessment using targeted GUVs labelled with Gd-HPDO3A. As anticipated above, the MRI sensitivity test was carried out using T_2^* as the parameter of choice. Folate-bearing GUVs labelled cells were mixed with unlabelled cells at different ratios to assess the sensitivity threshold for these imaging reporters, as previously reported in literature.²⁰

In Figure 3A, T_2^* -weighted images of cellular pellets are reported while Figure 3B reports the corresponding T_2^* changes.

These results show that it is possible to appreciate a difference in T_2^* contrast between labelled and unlabelled cells up to a dilution of 10% of GUVs labelled cells into control cells.

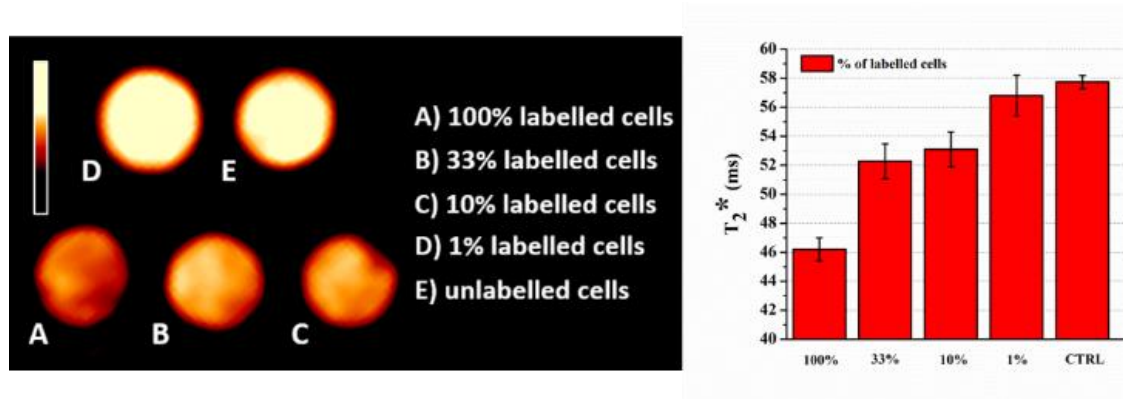


Figure 3. Left) T_2^* -weighted images of IGROV-1 cells pellets at different dilutions of targeted cells in control cells. Right) T_2^* values (ms) reported for the different samples.

From T_2^* measurement of the 100% labelled sample, known the number of cells and the millimolar relaxivity (r_{2p}) of the giant vesicles, it was possible to estimate approximately the number of liposomes bound *per* cell. Due to the fact that FRs cycle between the cell surface and an internal compartment, we have observed in the confocal microscopy images a heterogeneous distribution of bound GUVs among cells.²¹ In this experiment, it was found an average of 1.5 bound fluorescent folate-targeted GUVs *per* cell. Thus T_2^* appears a sufficiently sensitive parameter to detect targeting of a small number of cells.

Conclusions

In summary one may draw the following conclusions:

- 1) GUVs represent good candidates for cellular labelling by exploiting the binding to extracellular receptors even when their expression is very low. When translated to *in vivo* conditions we might envisage a limitation due to the lack of extravasation of such large particles. Likely, endothelial cells lining the vasculature may represent the most suitable target for GUVs.
- 2) The herein tested paramagnetic GUVs resulted suitable as T_2^* agents. Since, in general, positive contrast in MRI is favorable with respect to negative one, efforts have to be devoted to design GUVs as high sensitivity T_1 agents. One possibility is to exploit enhancement of the water exchange rate across the liposomal membrane.
- 3) The observed binding of targeting GUVs at the selected receptor sites may provide new opportunities for the development of "theranostic" agents. The application of proper *stimuli* can trigger the release of the drug and of the contrast agent eventually present in the inner aqueous cavity. Finally, the availability of targeting systems loaded with very high payloads of Gd(III) complexes may find applications in the emerging Spectral CT imaging modality where a high local density of heavy Gd ions is mandatory for the design of dedicated targeting contrast agents.²²

Experimental

Chemicals: Gd-HPDO3A was kindly provided by Bracco Imaging SpA (Colleretto Giacosa (TO), Italy). 1,2-dipalmitoyl-sn-glycero-3-phosphocholine (DPPC), 1,2-distearoyl-sn-glycero-3-phosphoethanolamine-N-[methoxy(polyethylene glycol)-2000] (ammonium salt) (DSPE-mPEG2000), 1,2-distearoyl-sn-glycero-3-phosphoethanolamine-N-[folate(polyethylene glycol)-2000] (ammonium salt) (DSPE-PEG2000 Folate), 1,2-dioleoyl-sn-glycero-3-phosphoethanolamine-N-(lissamine rhodamine B sulfonyl) (ammonium salt) (Liss Rhod PE) were purchased from Avanti Polar Lipids Inc. Vybrant™ DiD cell-labelling solution was purchased from Thermo Fisher Scientific. NaCl, HEPES (4-(2-hydroxyethyl)-1-piperazineethane-sulfonic acid), NaOH, HCl, 5(6)-Carboxyfluorescein, chloroform and all the other chemicals were purchased from Sigma Aldrich Co. LLC.

Liposomes preparation and characterization: Giant liposomes were prepared according to a procedure reported in literature with modifications.¹² The desired blend of phospholipids (0.0224 mmol) dissolved in chloroform (1 ml) is spread on the bottom of a 2 L Erlenmeyer flask and it is dried for 15 minutes with a flux of Argon. The hydration solution (25 ml) is then gently added and the flask is set for 2 h at 60°C without any mechanical stress. After that, the flask is gently swirled, the cloudy suspension recovered and cooled to room temperature. The suspension recovered from the flask is centrifuged 30 minutes at 6500 rpm in a fixed 45° angle centrifuge in order to purify the giant liposomes suspension from impurities and small liposomes populations eventually present. The supernatant is discarded, fresh HEPES/NaCl buffer is added and 4 cycles of centrifugation and resuspension are performed in order to extensively wash the giant liposomes. The size of giant liposomes was characterized by confocal fluorescence microscopy images. A formulation of giant liposomes of DPPC/Liss Rhod PE/DSPE-mPEG2000 96.95/0.05/3 molar ratio membrane and 20 μM 5(6)-carboxyfluorescein in the aqueous phase was prepared for this purpose.

Z-stack images were acquired on a Leica SP8 confocal system (Leica Microsystems) in order to center every vesicle in its main diameter to be suitably measured. The following wavelengths were considered for the microscopy visualization: 1) $\lambda^{\text{ex}}=492$ nm, $\lambda^{\text{em}}=517$ nm for 5(6)-carboxyfluorescein, 2) $\lambda^{\text{ex}}=545$ nm, $\lambda^{\text{em}}=567$ nm for Rhodamine-B. Dynamic Light Scattering (DLS) measurements were acquired at 298 K (Zetasizer NanoZS, Malvern, UK) to make sure there was no evidence of populations of liposomes between 50 nm and 800 nm.

Folate-targeted giant liposomes were prepared according to the above-mentioned protocol using a blend of phospholipids of DPPC/DSPE-PEG2000 Folate/Liss Rhod PE 96.95/3/0.05 molar ratio entrapping 300 mM Gd-HPDO3A and 20 μM 5(6)-carboxyfluorescein.

Small liposomes were prepared by using the conventional thin lipidic film method.¹⁴ Briefly, the desired blend of phospholipids dissolved in chloroform was slowly evaporated to remove the solvent until a thin film was formed on a round bottom flask. The film was then hydrated at 55°C with the hydration solution (1 ml). The resulting suspension of multilamellar vesicles was extruded (Lipex extruder, Northern Lipids Inc., Canada) four times on polycarbonate filters with a pore diameter of 400 nm and six times on polycarbonate filters with a pore diameter of 200 nm. The

final suspension of liposomes was purified from the non-encapsulated metal complex by exhaustive dialysis carried out at 4°C against HEPES/NaCl buffer. The vesicles were characterized by using DLS to assess the mean hydrodynamic diameter and the polydispersity of the system. The molar concentration of small and giant vesicles was evaluated by using Equation 1:

$$[Liposomes] = \frac{[Gd]_{TOT} \times 1 L}{V_i \times [Gd]_{inralipo}} = \frac{[Gd]_{TOT} \times 1 L}{\frac{4}{3}\pi r^3 \times [Gd]_{inralipo}} \quad (1)$$

where $[Gd]_{TOT}$ is determined either by acidic digestion of the sample and quantification of Gadolinium, r is the radius of the vesicle and $[Gd]_{inralipo}$ is assumed to be the same of the hydration solution.¹⁶

Transverse relaxation time (T_2): The transverse water proton relaxation times were measured by using a Stelar SpinMaster relaxometer (Stelar, Mede (PV), Italy) operating at 0.5 T (21.5 MHz Proton Larmor Frequency), by mean of the standard Carr-Purcell-Meiboom-Gill (CPMG) sequence. The temperature was controlled with a Stelar VTC-91 air-flow heater equipped with a copper constantan thermocouple (uncertainty 0.1°C). T_2 measurements were also acquired at 7 T on a Bruker Avance 300 spectrometer.

Cells cultures: Cellular experiments were performed using IGROV-1 human ovarian carcinoma cells obtained from American Type Culture Collection (ATCC, Manassass, VA).

IGROV-1 cells were grown in RPMI¹⁰⁶⁴ supplemented with 10% (v/v) heat-inactivated fetal bovine serum (FBS), 2 mM glutamine, 100 U/ml penicillin and 100 mg/ml streptomycin.

For cell labelling experiment, IGROV-1 cells were grown for 48h in folate-free RPMI medium supplemented with 10% (v/v) heat-inactivated fetal bovine serum (FBS), 2 mM glutamine, 100 U/ml penicillin and 100 mg/ml streptomycin.

Cells were seeded in 75-cm² flasks at density of *ca.* 2×10^4 cells/cm² in a humidified 5% CO₂ incubator at 37 °C. When cells reached confluence, they were detached by adding 1 ml of Trypsin-EDTA solution (0.25% (w/v) Trypsin-0.53 mM EDTA).

All the used cells were negative for mycoplasma as tested by using MycoAlert™ Mycoplasma Detection Kit by Lonza (Lonza Sales AG, Verviers, Belgium).

RPMI, folate-deficient RPMI, FBS, Trypsin/EDTA, glutamine, penicillin-streptomycin mixture, MycoAlert™ Mycoplasma Detection Kit and non-enzymatic cell dissociation solution were purchased from Lonza (Lonza Sales AG, Verviers, Belgium).

Cell targeting for MRI detection: For labelling experiments, 1×10^6 IGROV-1 cells were seeded into 6-cm Petri dishes 48 h before the experiment in presence of folate-free medium, changed every day. Then, they were incubated for 30 min at 37°C in presence of folate-targeted-GUVs (*ca.* 1×10^8 vesicles *per* plate). As control, unlabelled IGROV-1 cells were used. After the labelling, cells were extensively washed with fresh PBS to remove unbound liposomes and detached by means of non-enzymatic cell dissociation solution (2 ml for each Petri dish). It was avoided the use of Trypsin to prevent degradation of membrane FOLRs. Folate-GUVs-labelled cells were diluted with

unlabelled control cells to different extent (1% ÷ 100%), then collected with PBS and pelleted by centrifugation (1200 rpm, 5 min, 25°C). Finally, cells were collected by using 50 µL of PBS, loaded into glass capillaries and centrifuged to obtain pellets for MR imaging.

IGROV-1 cell targeting for confocal fluorescence microscopy analysis: For labelling experiments, 1.5×10^4 IGROV-1 cells were seeded into µ-Slide 8 Well (Ibidi, Martinsried, Germany) two days before the imaging and cultivated in presence of folate-free medium. Then they were incubated for 30 min at 37°C in presence of fluorescent folate-targeted-GUVs (*ca.* 5.2×10^6 vesicles *per* plate). Two controls were considered. The first one was carried out by labelling cells with untargeted-GUVs in presence of folate-free cell medium. The second one was carried out by labelling cells with folate-targeted-GUVs in presence of folate-containing cell medium ([Folate]=2.5 µM). After the labelling, cells were extensively and gently washed with fresh PBS to remove unbound liposomes. The staining of cells was carried out by using the Vybrant™ DiD Cell-Labeling Solution (Thermo Fisher) as suggested by the provider ($\lambda^{\text{ex}}=644$ nm, $\lambda^{\text{em}}=665$ nm). Briefly, staining medium was prepared by adding 5 µL of the fluorescent dye solution to 1 mL of cell medium. Each cell-containing well was treated with 0.3 mL of the obtained solution at 37°C for 5 min. Then the solution was removed, cells washed with PBS, covered with fresh medium and used for confocal fluorescent microscopy observation, carried out by using the Leica SP8 confocal system (Leica Microsystems). The following wavelengths were considered for the microscopy visualization: 1) $\lambda^{\text{ex}}=492$ nm, $\lambda^{\text{em}}=517$ nm for 5(6)-carboxyfluorescein, 2) $\lambda^{\text{ex}}=545$ nm, $\lambda^{\text{em}}=567$ nm for Rhodamine-B and 3) $\lambda^{\text{ex}}=644$ nm, $\lambda^{\text{em}}=665$ nm for Vybrant™ DiD).

MRI experiments: For MRI acquisition, the incubated cells were detached, extensively washed with PBS, collected in 50 µL of PBS, transferred into glass capillaries (diameter *ca.* 1 mm) and then centrifuged at 1200 rpm for 5 min. The capillaries were placed in water-containing tube (diameter *ca.* 1 cm) for image acquisition. MRI scans were acquired at 7 T on a Bruker Avance 300 spectrometer equipped with the Micro 2.5 microimaging probe.

T_{2w} images were acquired by using a standard MSME (multislice multiechoes) sequence with the following parameters (TR = 2000 ms, TE = 152.5msec, FOV = 1 cm x 1 cm, slice thickness = 1 mm, matrix size 128 x 128, spatial resolution 0.078x0.078 mm²/voxel). T_2 values were measured by using a MSME sequence (TR = 2000 ms, 20 variable TE ranging from 11 to 500 ms, FOV = 1 cm x 1 cm, slice thickness = 1 mm, matrix size 128 x 128, spatial resolution 0.078 x 0.078 mm²/voxel).

References

1. Vithanarachchi, S. M., & Allen, M. J. (2012). Strategies for target-specific contrast agents for magnetic resonance imaging. *Current Molecular Imaging (Discontinued)*, 1(1), 12-25.
2. Gianolio, E., Stefania, R., Di Gregorio, E., & Aime, S. (2012). MRI paramagnetic probes for cellular labeling. *European Journal of Inorganic Chemistry*, 2012(12), 1934-1944.
3. Aime, S., Cabella, C., Colombatto, S., Geninatti Crich, S., Gianolio, E., & Maggioni, F. (2002). Insights into the use of paramagnetic Gd (III) complexes in MR-molecular imaging investigations. *Journal of Magnetic Resonance Imaging: An Official Journal of the International Society for Magnetic Resonance in Medicine*, 16(4), 394-406.
4. Hsu, F. T., Sun, R., & Hsieh, C. L. (2019). Cellular Magnetic Resonance Imaging with Superparamagnetic Iron Oxide: Methods and Applications in Cancer. In *Spin* (Vol. 9, No. 02, p. 1940007). World Scientific Publishing Company.
5. Ramaswamy, S., Schornack, P. A., Smelko, A. G., Boronyak, S. M., Ivanova, J., Mayer Jr, J. E., & Sacks, M. S. (2012). Superparamagnetic iron oxide (SPIO) labeling efficiency and subsequent MRI tracking of native cell populations pertinent to pulmonary heart valve tissue engineering studies. *NMR in Biomedicine*, 25(3), 410-417.
6. Caravan, P. (2009). Protein-targeted gadolinium-based magnetic resonance imaging (MRI) contrast agents: design and mechanism of action. *Accounts of chemical research*, 42(7), 851-862.
7. Pagoto, A., Tripepi, M., Stefania, R., Lanzardo, S., Livio Longo, D., Garello, F., ... & Terreno, E. (2019). An efficient MRI agent targeting extracellular markers in prostate adenocarcinoma. *Magnetic resonance in medicine*, 81(3), 1935-1946.
8. Andia, M. E., Saha, P., Jenkins, J., Modarai, B., Wiethoff, A. J., Phinikaridou, A., ... & Botnar, R. M. (2014). Fibrin-targeted magnetic resonance imaging allows in vivo quantification of thrombus fibrin content and identifies thrombi amenable for thrombolysis. *Arteriosclerosis, thrombosis, and vascular biology*, 34(6), 1193-1198.
9. Chow, A. M., Tan, M., Gao, D. S., Fan, S. J., Cheung, J. S., Man, K., ... & Wu, X. (2013). Molecular MRI of Liver Fibrosis by a Peptide Targeted Contrast Agent in an Experimental Mouse Model. *Investigative radiology*, 48(1), 46.
10. Uppal, R., Medarova, Z., Farrar, C. T., Dai, G., Moore, A., & Caravan, P. (2012). Molecular imaging of fibrin in a breast cancer xenograft mouse model. *Investigative radiology*, 47(10).
11. Lee, R. J., & Low, P. S. (1994). Delivery of liposomes into cultured KB cells via folate receptor-mediated endocytosis. *Journal of Biological Chemistry*, 269(5), 3198-3204.

12. Reeves, J. P., & Dowben, R. M. (1969). Formation and properties of thin-walled phospholipid vesicles. *Journal of cellular physiology*, 73(1), 49-60.
13. Langereis, S., Geelen, T., Grüll, H., Strijkers, G. J., & Nicolay, K. (2013). Paramagnetic liposomes for molecular MRI and MRI-guided drug delivery. *NMR in Biomedicine*, 26(7), 728-744.
14. V. P. Torchilin, V. Weissig, in *Liposomes: Practical Approach*, (2003). Oxford University Press, NY, USA, 2nd ed., pp. 4-7.
15. Delli Castelli, D., Caligara, M. C., Botta, M., Terreno, E., & Aime, S. (2013). Combined high resolution NMR and ¹H and ¹⁷O relaxometric study sheds light on the solution structure and dynamics of the lanthanide (III) complexes of HPDO3A. *Inorganic chemistry*, 52(12), 7130-7138.
16. Mulas, G., Ferrauto, G., Dastrù, W., Anedda, R., Aime, S., & Terreno, E. (2015). Insights on the relaxation of liposomes encapsulating paramagnetic Ln-based complexes. *Magnetic resonance in medicine*, 74(2), 468-473.
17. Lutz, R. J. (2015). Targeting the folate receptor for the treatment of ovarian cancer. *Transl Cancer Res*, 4(1), 118-126.
18. Chaudhury, A., & Das, S. (2015). Folate receptor targeted liposomes encapsulating anti-cancer drugs. *Current pharmaceutical biotechnology*, 16(4), 333-343.
19. Pelkmans, L., & Helenius, A. (2002). Endocytosis via caveolae. *Traffic*, 3(5), 311-320.
20. Delli Castelli, D., Ferrauto, G., Di Gregorio, E., Terreno, E., & Aime, S. (2015). Sensitive MRI detection of internalized T1 contrast agents using magnetization transfer contrast. *NMR in Biomedicine*, 28(12), 1663-1670.
21. Kamen, B. A., & Smith, A. K. (2004). A review of folate receptor alpha cycling and 5-methyltetrahydrofolate accumulation with an emphasis on cell models in vitro. *Advanced drug delivery reviews*, 56(8), 1085-1097.
22. Feuerlein, S., Roessl, E., Proksa, R., Martens, G., Klass, O., Jeltsch, M., ... & Schlomka, J. P. (2008). Multienergy photon-counting K-edge imaging: potential for improved luminal depiction in vascular imaging. *Radiology*, 249(3), 1010-1016.

- Chapter 4 -

Detection of U-87 tumor cells by RGD-functionalized/ Gd-containing Giant Unilamellar Vesicles (Gd-GUVs) in Magnetization Transfer Contrast (MTC)-MR images

Giuseppe Ferrauto*, Martina Tripepi, Enza Di Gregorio, Valeria Bitonto, Silvio Aime, Daniela Delli Castelli

Published as Full Paper: *Investigative Radiology*, 2020

Abstract

The targeting of tumor cells and their visualization with MRI is an important task in biomedicine. The low sensitivity of this technique is a significant drawback, and one that may hamper the detection of the imaging reporters used.

To overcome this sensitivity issue, this work explores the synergy between two strategies: *i*) RGD-functionalized Giant Unilamellar Vesicles (GUVs) loaded with Gd-complexes to accumulate large amounts of MRI contrast agent at the targeting site; and *ii*) the use of Magnetization Transfer Contrast (MTC), which is a sensitive MRI technique for the detection of Gd-complexes in the tumor region.

GUVs were prepared using the gentle swelling method, and the cyclic RGD targeting moiety was introduced onto the external membrane. Paramagnetic Gd-containing complexes were both part of the vesicle membranes and were the payload within the inner aqueous cavity together with the fluorescent probe, rhodamine. GUVs that were loaded with the imaging reporters, but devoid of the RGD targeting moiety, were used as controls. U-87 MG human glioblastoma cells, which are known to overexpress the targets for RGD moieties, were used. In the *in-vivo* experiments, U-87 MG cells were subcutaneously injected into *nu/nu* mice and the generated tumors were imaged using MRI, 15 days after cell administration. MRI was carried out at 7 T, and T_{2w} , T_{1w} and MTC/Z-spectra were acquired. Confocal microscopy images and ICP-MS were used for result validation. *In-vitro* results show that RGD GUVs specifically bind to U-87 MG cells. Microscopy demonstrates that: *i*) RGD GUVs were anchored onto the external surface of the tumor cells without any internalization; *ii*) a low number of GUVs per cell were clustered at specific regions; *iii*) there is no evidence for macrophage uptake or cell toxicity. The MRI of cell pellets after incubation with RGD GUVs and untargeted ctrl-GUVs was performed. No difference in T_1 signal was detected, whereas a 15% difference in MT contrast is present between the RGD-GUV-treated cells and the ctrl-GUV-treated cells.

MR images of tumor-bearing mice were acquired before and after ($t=0$, 4 h and 24 h) the administration of RGD GUVs and ctrl-GUVs. A roughly 16% MTC difference between the two groups was observed after 4 h. Immunofluorescence analyses and ICP-MS analyses (for Gd-detection) of the explanted tumors confirmed the specific accumulation of RGD GUVs in the tumor region.

RGD GUVs appear to be interesting carriers that can facilitate the specific accumulation of MRI contrast agents at the tumor region. However, the concentration achieved is still below the threshold needed for T_{1w} -MRI visualization. Conversely, MTC proved to be sufficiently sensitive for the visualization of detectable contrast between pre- and post-targeting images.

Keywords: Gd-contrast agents • Giant liposomes • Imaging agents • Magnetization Transfer Contrast (MTC) • Magnetic Resonance Imaging (MRI) • T_1 agents • RGD tumor targeting

Introduction

Cancer is currently considered to be one of the most dangerous threats to human health, with more than 18 million new cases and 9 million deaths per year worldwide.¹ Early diagnosis and personalized medicine are currently considered to be the main tools for oncologists in the battle to fight cancer.

Magnetic Resonance Imaging (MRI) is one of the most powerful of the available diagnostic techniques for the *in-vivo* imaging of cancer because of its high spatial resolution (in the order of μm), the possibility of visualizing soft deep tissues and the absence of ionizing radiation.² The use of exogenous Gd-based contrast agents (GBCAs) often enhances the potential of the technique as it adds physio-pathological information to the superb spatial resolution that can be obtained from MR images.³⁻⁷ Unfortunately, the intrinsically low sensitivity of MRI requires the presence of relatively high amounts of GBCAs, making their use in molecular-imaging protocols problematic. It was established quite early in the technique's lifetime that the accumulation of *ca.* 10^8 gadolinium atoms per cell is required to reach the MRI detection threshold.⁸

Caution in the use of GBCAs has recently been advised. Although they are highly water soluble complexes that have been chemically designed for complete elimination from the body after intravenous administration, it has been widely demonstrated that the metal can accumulate in many organs (*e.g.* brain, kidney, liver, muscles, etc.).⁹⁻¹⁴

One of the most important goals, that of early diagnosis, can therefore be achieved by developing GBCAs that can specifically accumulate at the pathological tissue, via binding to epitopes that identify the tumor cells, even when the disease is at the preliminary stages. This can reduce the dose of GBCAs and improve the diagnostic potential of MRI. However, this task is often hampered by the small number of targeting sites that allow differentiation between healthy and tumor tissues.¹⁵

The issue of overcoming the sensitivity threshold that is associated with the presence of a limited number of targeted epitopes may be tackled using the synergic combination of two approaches: *i)* the use of targeted nano- or micro-sized systems that carry a high number of GBCAs;¹⁶⁻²⁰ and *ii)* the use of highly sensitive MRI procedures/sequences for detecting those same GBCAs.²¹

A large *portfolio* of targeted nano- or micro-sized systems that can carry MRI CAs is available.¹⁶⁻²⁰ In general, such systems have to display: *i)* high biocompatibility; *ii)* a long *in-vivo* half-life so that as many targets as possible can be reached; and *iii)* the capacity to carry a high payload of GBCAs. Of the available nano-/micro-systems, liposomes are largely considered to be the candidates of choice, as seen in several successful cases reported in pre-clinical studies.¹⁶⁻²⁰ The use of micro-sized liposomes (Giant Unilamellar Vesicles, GUVs, mean diameter in the micrometric range) appears to represent a further step forward, both in terms of the delivery of higher amounts of GBCAs and their particular binding to extracellular epitopes, as their large size hampers cell internalization and uptake by macrophages.^{22,23} GUVs can be easily prepared and characterized and, recently, have been formulated with Ln-complexes either loaded into their inner cavity (hydrophilic complexes) or incorporated into the phospholipidic membrane (hydrophobic or amphiphilic systems).²²⁻²⁴

Both linear and macrocyclic Gd-complexes are currently being used as CAs in clinical MRI applications. Their presence is detected by acquiring T_{1w} -MR images, *i.e.* by exploiting the relaxation enhancement they yield on bulk water protons (longitudinal relaxation time, T_1) (Fig. S1, Supplementary figures). The detection of GBCAs via T_1 contrast requires the accumulation of high amounts of Gd-complexes in the voxels of interest (of the order of 5 - 50 μM). This concentration is not easily attainable in targeting MRI experiments.²⁵

Some years ago, we reported the use of Magnetization Transfer Contrast (MTC) as a means of improving the MRI detection of T_1 relaxation agents.²⁰

The method is based on the T_1 dependence of MT contrast, and we discovered that tiny amounts of GBCAs, not enough to affect the T_{1w} images, are sufficient to affect the MTC readout.

Magnetization Transfer Contrast (MTC) is a MRI procedure that has been shown to be particularly useful in several clinical applications.²⁶⁻²⁹

It is based on the radiofrequency saturation of resonances of protons that belong to immobilized, semi-solid macromolecules (*e.g.* proteins in the cytoskeleton or bound to biomembranes) and of the water molecules that are tightly bound to them, which are not detectable in NMR spectra because of their very short T_2 relaxation times. Upon radiofrequency irradiation (at a chemical shift that is far from *bulk* water resonance), the saturated protons may enter the free bulk water proton pool, and thus transfer their saturated magnetization to the free water protons.

The magnetization transfer lead to a decrease of the MR signal and consequently to the generation of contrast due to the difference between the signal acquired with and without the saturation pulse. The MT amount is directly proportional to the longitudinal relaxation time (T_1) of the *bulk* water protons (*i.e.* the longer the T_1 the higher is the associated MTC effect), (Fig.S1, Supplementary figures).²⁰ Thus, it is expected that the presence of paramagnetic GBCAs (causing a reduction of T_1) would result in a decrease of the MT amount. The herein reported contrast relies in the difference between MR signals acquired with a MT based protocol before and after GBCAS administration. In particular, the MR signal increases after GBCAs administration. This behavior was earlier reported in cells and the sensitivity showed to be higher with respect to conventional T_{1w} contrast.²⁰ Starting from the above reported considerations, herein we investigated the synergic advantage of using Gd-containing-GUVs and MTC-MRI methodology for targeting tumor cells.

RGD GUVs loaded with Gd complexes, both in the membranes and in the inner cavity, able to bind integrins, were synthesized for this purpose. This study deals with *in vitro* and *in vivo* investigations, using U-87 MG human glioblastoma cells, which are known to overexpress beta-integrins.

Results

The aim of this work is to develop a MRI methodology that can detect tumors using Gd-loaded-targeting-GUVs and the MTC-MRI modality. U-87 MG human glioblastoma cells that overexpress integrin receptors were used as the target cancer cells. For this purpose, c(RGDfC) was used as the targeting vector as it is able to bind integrin receptors. In order to target GBCAs to U-87 tumor

cells, giant unilamellar vesicles were functionalized with cyclic-RGD and loaded with an amphiphilic Gd-complex in the membrane and Gd-HPDO3A in the internal aqueous cavity (RGD-Gd GUVs).

Gd-HPDO3A is widely used in clinical and preclinical experiments and shows no toxicity.^{39,40}

Fig.1A provides a representation of RGD-Gd GUVs. GUVs were prepared as reported in the literature,^{23,33} and the c(RGDfC) peptide was attached to the DSPE-PEG2000Maleimide phospholipid component of the GUVs.³⁵

Gd-GUVs *w/o* the c(RGDfC) peptide (ctrl-Gd GUVs) were prepared by incorporating DSPE-mPEG2000 phospholipids, instead of DSPE-PEG2000Maleimide, into the membrane composition, and were used as controls.

The main features of the two GUV preparations are summarized in Table 1. They display quite similar size (hydrodynamic diameter is 2.0 ± 0.3 and $1.5 \pm 0.2 \mu\text{m}$, for RGD-Gd GUVs and ctrl-Gd GUVs, respectively, Fig.1B), surface ζ -potential (-5.9 ± 0.6 mV and -2.2 ± 0.2 mV, for RGD-Gd GUVs and ctrl-Gd GUVs, respectively) and longitudinal relaxation rate (r_1 normalized for 1 mM of Gd-concentration). The relaxivities were *ca.* $5.5 \text{ mM}^{-1}\text{s}^{-1}$ and *ca.* $1.8 \text{ mM}^{-1}\text{s}^{-1}$ for RGD-Gd GUVs and ctrl-Gd GUVs at 0.5 and 7 T, respectively).

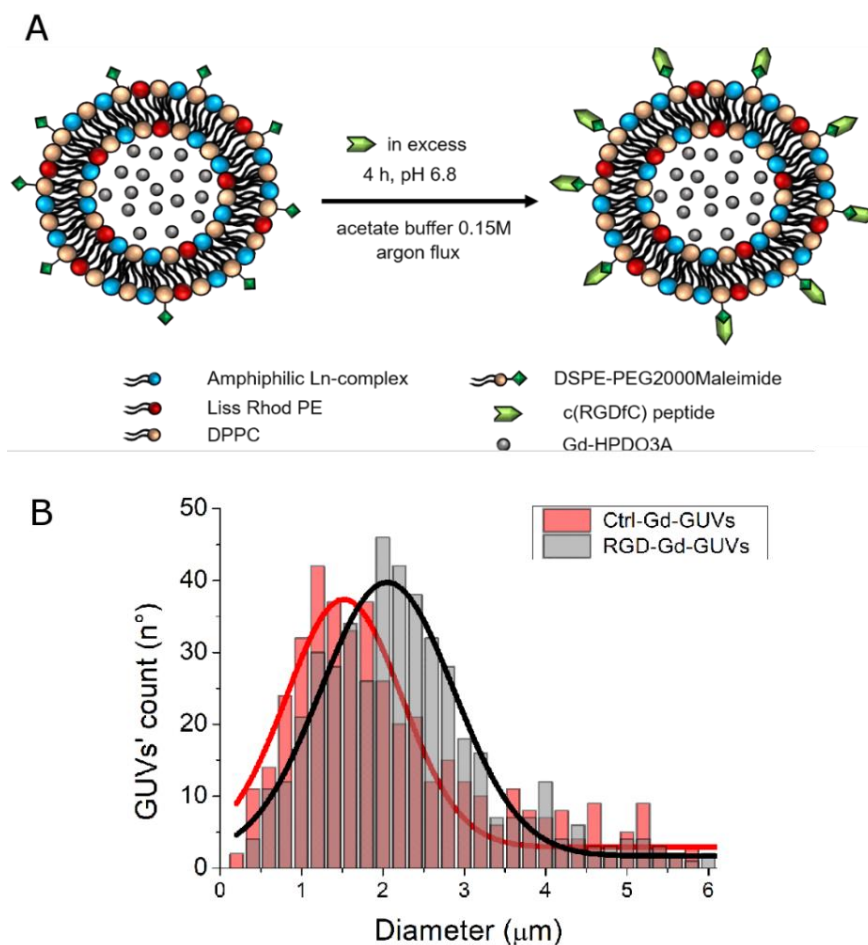


Figure 1. (A) Schematic representation of RGD-Gd-GUV formulation and the chemical addition of the targeting vector (the relative amount and size of the different chemicals is not to scale); (B) GUV diameter size distribution as assessed by confocal microscopy analysis.

Chapter 4: MTC-MRI visualization of Gd-GUVs

Table 1. Main features of RGD-Gd GUVs and ctrl-Gd GUVs.

| | RGD-Gd GUVs | Ctrl-Gd GUVs |
|--|---|---|
| Membrane formulation | DPPC 86.95% Amphiphilic Gd-complex 10% Liss Rhod PE 0.05% DSPE-PEG2000Maleimide 3% | DPPC 86.95% Amphiphilic Gd-complex 10% Liss Rhod PE 0.05% DSPE-mPEG2000 3% |
| Hydration solution | 40 mM Gd-HPDO3A in HEPES/NaCl buffer (3.8 mM HEPES, 0.15 M NaCl) | 40 mM Gd-HPDO3A in HEPES/NaCl buffer (3.8 mM HEPES, 0.15 M NaCl) |
| Hydrodynamic diameter (mean \pm σ) | 2.0 \pm 0.3 μ m | 1.5 \pm 0.2 μ m |
| Surface ζ-potential (mean \pm SD) | -5.9 \pm 0.6 mV | -2.2 \pm 0.2 mV |
| Longitudinal relaxation rate (r_1) | ca. 5.5 mM ⁻¹ s ⁻¹ (at 0.5 T, 25°C) ca.1.8 mM ⁻¹ s ⁻¹ (at 7 T, 25°C) | ca. 5.5 mM ⁻¹ s ⁻¹ (at 0.5 T, 25°C) ca.1.8 mM ⁻¹ s ⁻¹ (at 7 T, 25°C) |

As the synthesized Gd-GUVs display good paramagnetic and fluorescent properties, making them suitable for MRI and fluorescence microscopy applications, they were tested for their ability to target U-87 MG cells in cultures.

Firstly, the potential cytotoxicity of the GUVs was assessed *in vitro* using a MTT cell viability test.³⁶ As reported in Fig.2A, only a small effect on glioblastoma cell viability was detected upon incubation with RGD-Gd GUVs and ctrl-Gd GUVs (cell viability is higher than 90% for [GUVs] up to ca. 10 pM). Moreover, no significant difference was detected in the two GUV formulations (Fig.2A). Overall, the observed toxicity appears to be acceptable, as expected considering the well-established tolerability of Gd-HPDO3A, which is the main GBCA in the formulations.^{39,40}

Confocal microscopy images of the cells were acquired to gain further insight into the specific binding of RGD-Gd GUVs to U-87 MG cells. The cells were stained using Phalloidin-FITC (*green*). Fig.2B and C report representative images of U-87 glioblastoma cells after 30 min of incubation either in the presence of RGD-Gd GUVs (Fig.2B), or in the presence of ctrl-Gd GUVs (Fig.2C). As expected, GUVs are only bound to glioblastoma cells when the RGD moiety is present.

The binding is specific without any evidence of the GUVs or their imaging reporters being internalized within the targeted cells. Furthermore, it can be noted that only a low number of GUVs are present per cell, and that there is evident vesicle clustering in discrete cell regions (mainly in cell spines) (Fig.2D, E and F magnification of U-87 MG cells incubated in the presence of RGD-Gd GUVs).

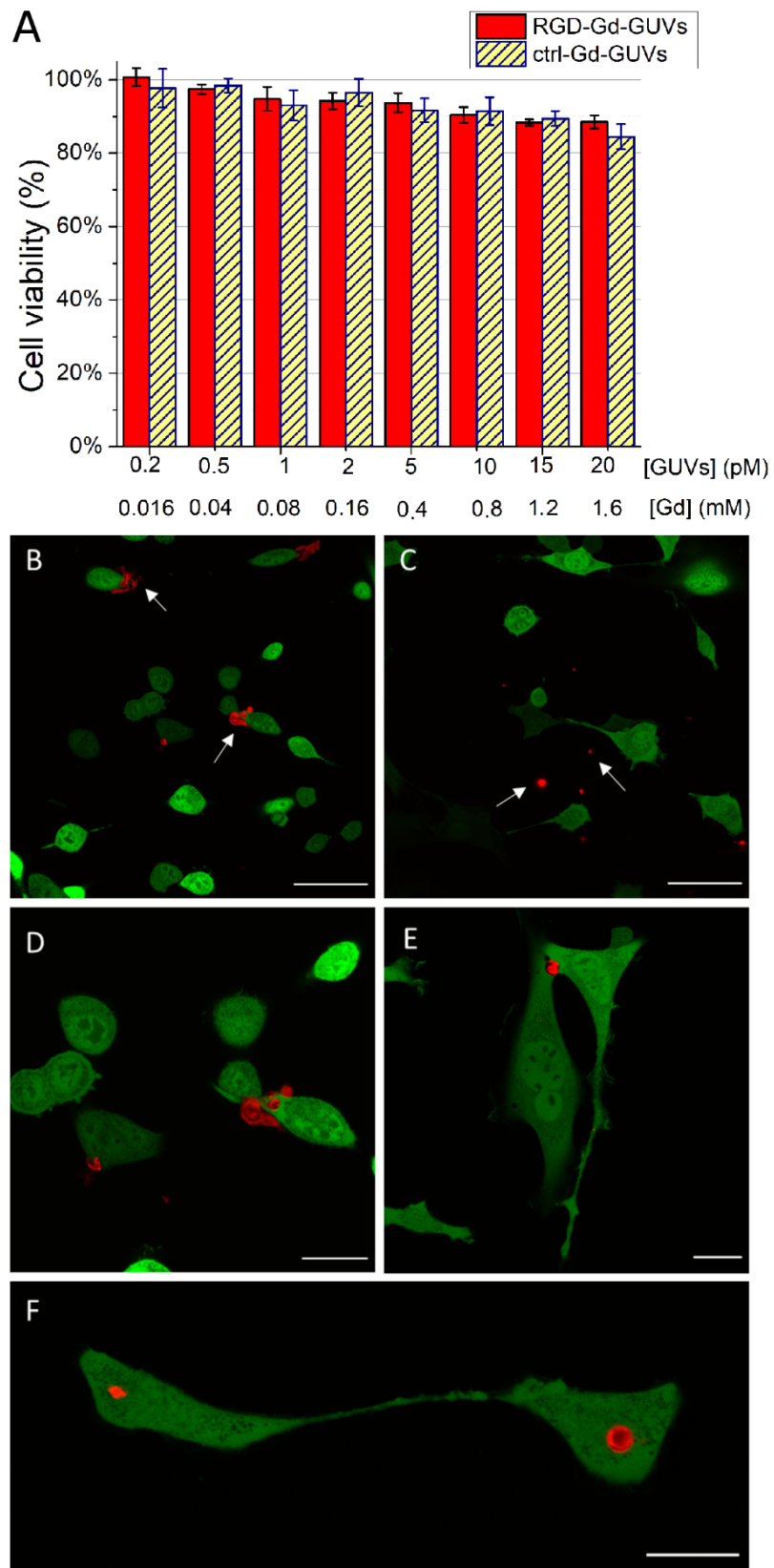


Figure 2. (A) U-87 MG cell viability upon 30 min incubation with RGD-Gd GUVs and ctrl-Gd GUVs. (B) Confocal fluorescence microscopy of live glioblastoma cells incubated in the presence of RGD-Gd GUVs, and (C) in the presence of ctrl-Gd GUVs (scale bar = 50 μ m). Arrows indicate RGD-Gd GUVs and ctrl-Gd GUVs. (D, E, F) Magnification of cells incubated in the presence of RGD-Gd GUVs (*red* = rhodamine-GUVs; *green* = Phalloidin-FITC) Scale bars = 20 μ m.

Considering the positive results for the cytotoxicity and specific binding of RGD-Gd GUVs to U-87 MG cells, the *in-vitro* targeting experiments for MRI detection were carried out. For this purpose, glioblastoma cells were incubated in the presence of either RGD-Gd GUVs or ctrl-Gd GUVs (particle concentration *ca.* 1 pM) for 30 min at 37°C. Then, after extensive washing with fresh PBS buffer, the cells were detached using a non-enzymatic cell-dissociation solution and centrifuged inside glass capillaries to give pellets for MRI acquisition, and in order to assess T_1 , T_2 and MTC responses. Fig.3A reports representative MRI results for the U-87 MG cell pellets (T_{2w} , T_{1w} and MTC images). Three specimens were considered: *i*) untreated U-87 MG cells (*negative control*); *ii*) U-87 MG cells incubated in the presence of ctrl-Gd GUVs (*second negative control*); and *iii*) U-87 MG cells incubated in the presence of RGD-Gd GUVs. The R_2 value of the cells incubated in the presence of ctrl-Gd GUVs was very similar to that of the specimen containing the unlabeled blank cells (19.37 ± 0.64 vs. 19.31 ± 0.19 s⁻¹, respectively) (Fig.3B).

Consequently, no T_2 contrast can be detected in the T_{2w} -MR images of the cells incubated in the presence of ctrl-Gd GUVs (Fig.3A *top*). In the case of incubation in the presence of targeted RGD-Gd GUVs, only a small increase in the R_2 value was detected (*i.e.* 22.62 ± 1.22 s⁻¹, corresponding to *ca.* 17% R_2 Enhancement) (Fig.3B). This slight increase in the R_2 value was barely detectable as contrast in the T_{2w} -MR images (Fig.3A *top*).

Furthermore, no differences in T_1 value nor T_1 contrast were observed in the T_{1w} -MR images (Fig.3C, A *middle*). Hence, the T_1 modality cannot be considered suitable for the detection of Gd-GUV-targeted cells in the applied experimental set-up. The Z-spectra of the U-87 MG cell specimens were then acquired using several B_1 pulses.

Representative MTC results obtained with $B_1 = 6$ μ T are reported in Fig.3A *bottom*, Fig.3D (Z-spectra), Fig.3E (magnification of Z-spectra) and Fig.3F (MTC^{enh%}). A MT contrast of MTC^{enh%} = 15.2 ± 1.9 % was found for pellets of the cells treated with RGD-Gd GUVs with respect to the pellets made of untreated cells, and a of MTC^{enh%} = 14.8 ± 2.3 % was found compared to the pellets of cells treated with ctrl-Gd GUVs. Comparable results were obtained using a $B_1 = 3$ and 12 μ T (Fig.S2-S5, Supplementary figures).

An ICP-MS determination of the Gd content in the cell specimens upon incubation in the presence of either RGD-Gd GUVs or ctrl-Gd GUVs showed a significantly higher amount (*ca.* 15 times) of Gd in the cell specimens incubated in the presence of targeting RGD-Gd GUVs, compared to cells treated with ctrl-Gd GUVs (1.2×10^8 vs. 8.2×10^6 Gd³⁺/cell, respectively). Data are reported in Fig.3G).

U-87 MG cells were incubated in the presence of empty RGD GUVs for use as controls (*i.e.* GUVs containing RGD moiety, but with no Gd-complexes either in the membrane or inner cavity), and their Z-spectrum was quite analogous to that of the untreated cells (Fig.S6, Supplementary figures), indicating that the presence of Gd-complexes is needed for the MTC effect.

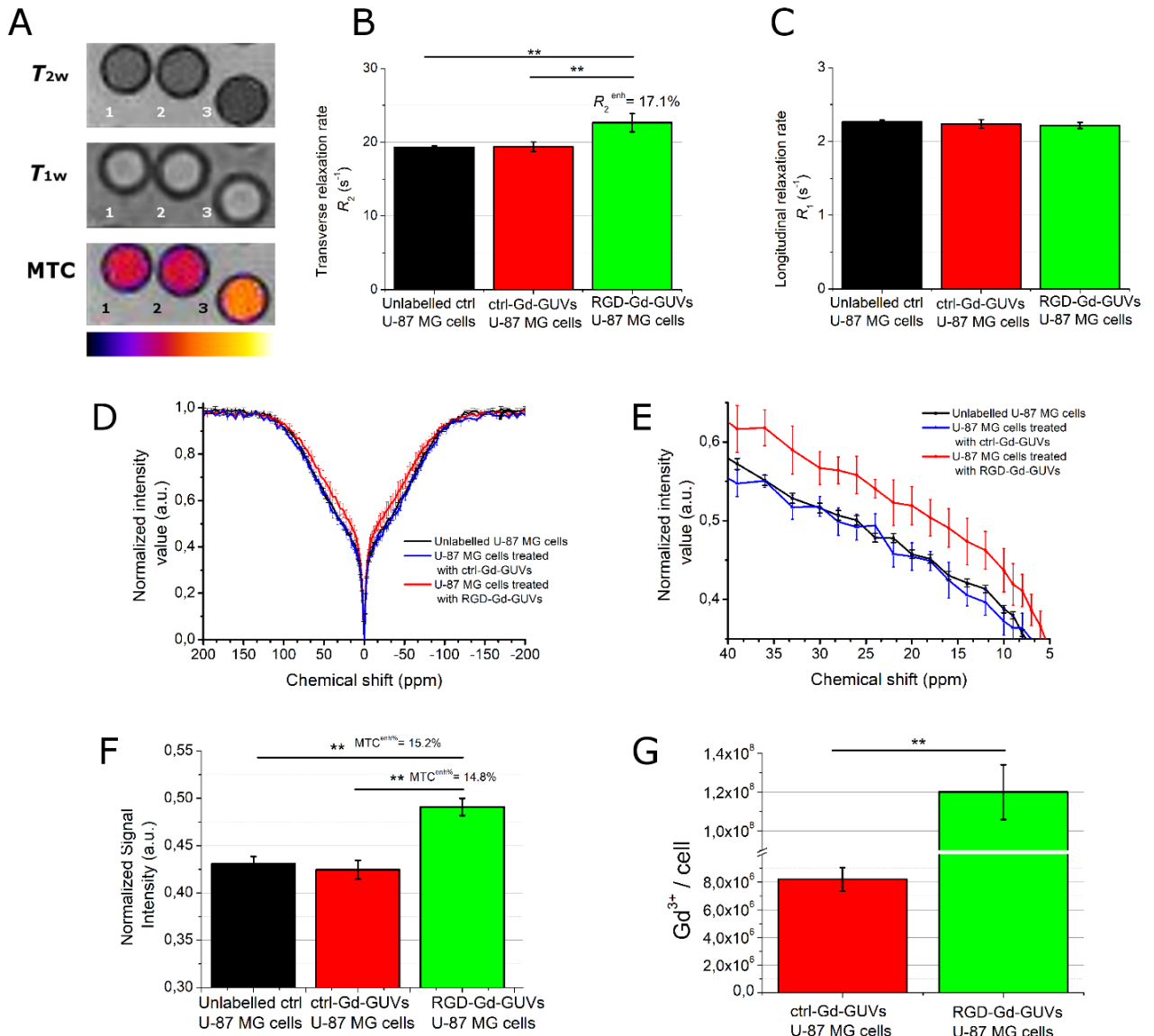


Figure 3. (A) T_{2w} (top), T_{1w} (middle) and MTC (bottom) MR images from representative phantoms composed of three glass capillaries filled with: 1) untreated U-87 MG cells, 2) U-87 MG cells incubated in the presence of ctrl-Gd GUVs and 3) U-87 MG cells incubated in the presence of RGD-Gd GUVs. (B) R_2 values of the three specimens. (C) R_1 values of the three specimens. (D) Z-spectra of the three specimens ($B_1=6 \mu T$). (E) Magnification of the Z-spectra in the 5-40 ppm region. (F) Normalized signal intensity of the three specimens from the Z-spectra (for calculating $MTC^{enh\%}$), $B_1=6 \mu T$. (G) ICP-MS quantification of Gd-content in cells.

The positive data obtained in cell cultures drove us to perform the *in-vivo* targeting experiments. The experimental protocol is reported in Fig.4A.

Representative T_{2w} - and T_{1w} MRI of tumors are reported in Fig.4B (tumors are indicated by the white arrows). The presence of the two tumor masses is clearly visible. Mice were divided into two groups. Group1 received ctrl-Gd GUVs (0.05 mmol_{Gd}/kg, slow infusion), whereas Group2 was treated with the same dose of RGD-Gd GUVs under analogous administration conditions. MRI was carried out before and after (t=0, 4 h and 24 h) GUV administration.

From these acquisitions, it was evident that both T_2 and T_1 contrast are not able to distinguish the tumors in Group1 mice from those of Group2 mice.

Chapter 4: MTC-MRI visualization of Gd-GUVs

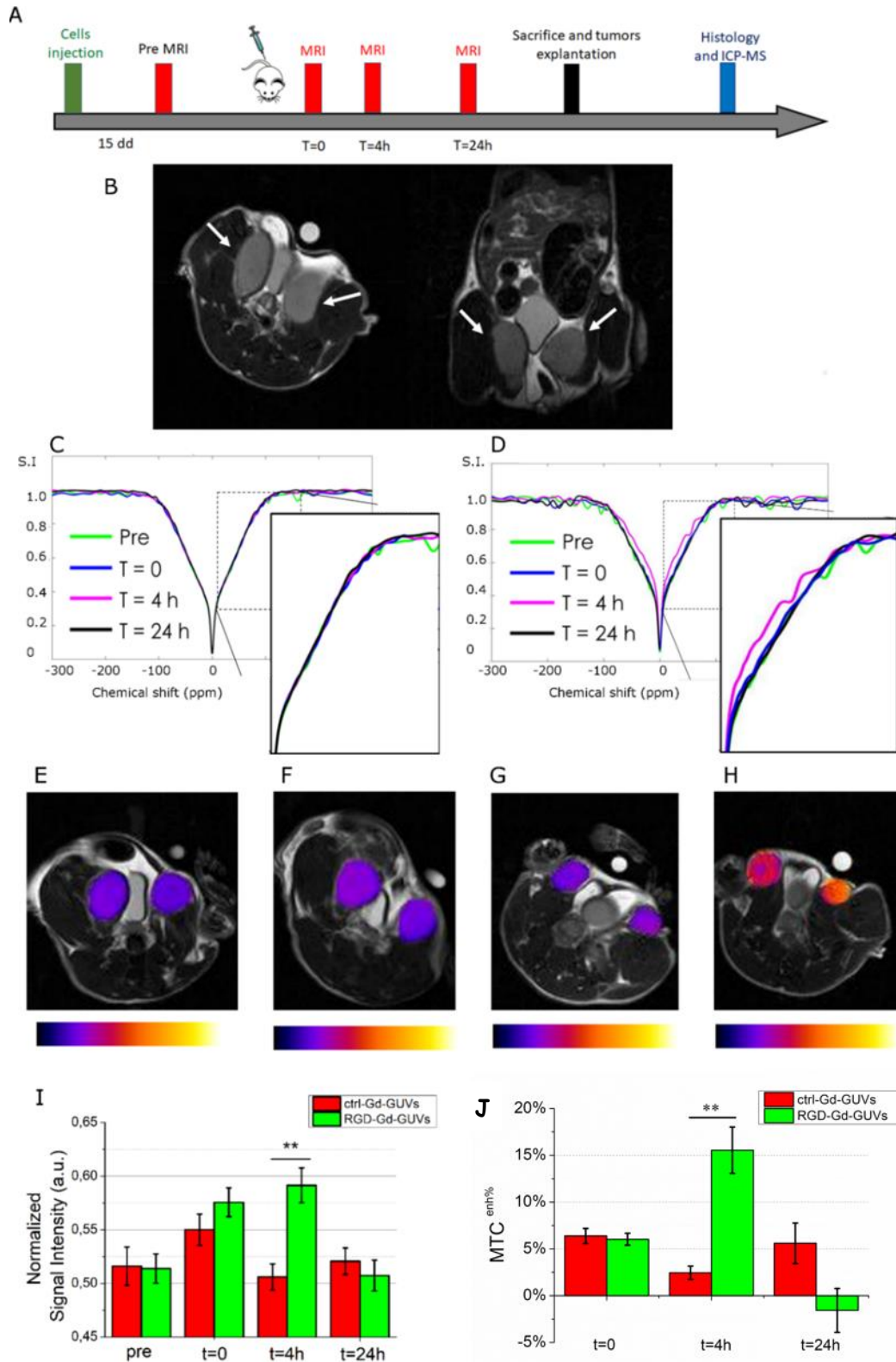


Figure 4. (A) Experimental set-up for *in-vivo* studies. (B) Representative axial and coronal T_{2w} and T_{1w} images of tumor-bearing mice. (White arrows indicate transplanted tumors). (C) Z-spectra from the tumor region before and after treatment with ctrl-Gd GUVs (t=0, 4h and 24h, Group1). (D) Z-spectra from the tumor region before and after treatment with RGD-Gd GUVs (t=0, 4h and 24h, Group2). (E) Representative MTC image of ctrl-Gd-GUV-treated mice t=0. (F) Representative MTC image of ctrl-Gd-GUV-treated mice t=4h. (G) Representative MTC image of RGD-Gd-GUV-treated mice t=0. (H) Representative MTC image of RGD-Gd-GUV-treated mice at t=4h. (I) Normalized signal intensity of tumor ROI pre- (t=0) and post-treatment (t=4h or 24h) with ctrl-Gd GUVs or RGD-Gd GUVs. (J) MTC^{enh%} of the tumor region at t=0, 4h and 24h.

As far as the Z-spectra are concerned, no difference can be detected between pre and post ctrl-Gd-GUV administration in Group1 (Fig.4C). On the other hand, in the case of Group2 (administration of RGD-Gd GUVs), a clear difference in the Z-spectra is present at t=4 h post administration. At t=0 and t=24 h post injection, the Z-spectra almost completely overlap with the pre-administration ones (Fig.4D).

Fig.4E-H report representative MTC MR images of mice treated with either ctrl-Gd GUVs or RGD-Gd GUVs at t=0 and t=4h. The normalized signal intensities obtained from the Z-spectra of tumor ROIs are reported in Fig.4I. There is only a significant increase in signal, *i.e.* a reduction in the MT effect, at t=4h for the RGD-Gd-GUV-treated mice. A quantitative analysis was carried out by measuring the MTC enhancement, and the results are reported in Fig.4J. At t=0 there is a very small MTC% contrast (*ca.* 5%), which is comparable for the two groups. At t=4 h the difference between the two groups is significant (16% vs. 2%, P-value < 0.05). At t=24 h, the MTC% of Group1 decreases and, in general, the difference between the two groups is no longer significant. The observed behavior suggests that the MTC data are indicative of the binding of RGD-Gd GUVs to glioblastoma tumor cells, with a maximum effect that corresponds to the maximum Gd accumulation (*vide infra*), at around t=4 h.

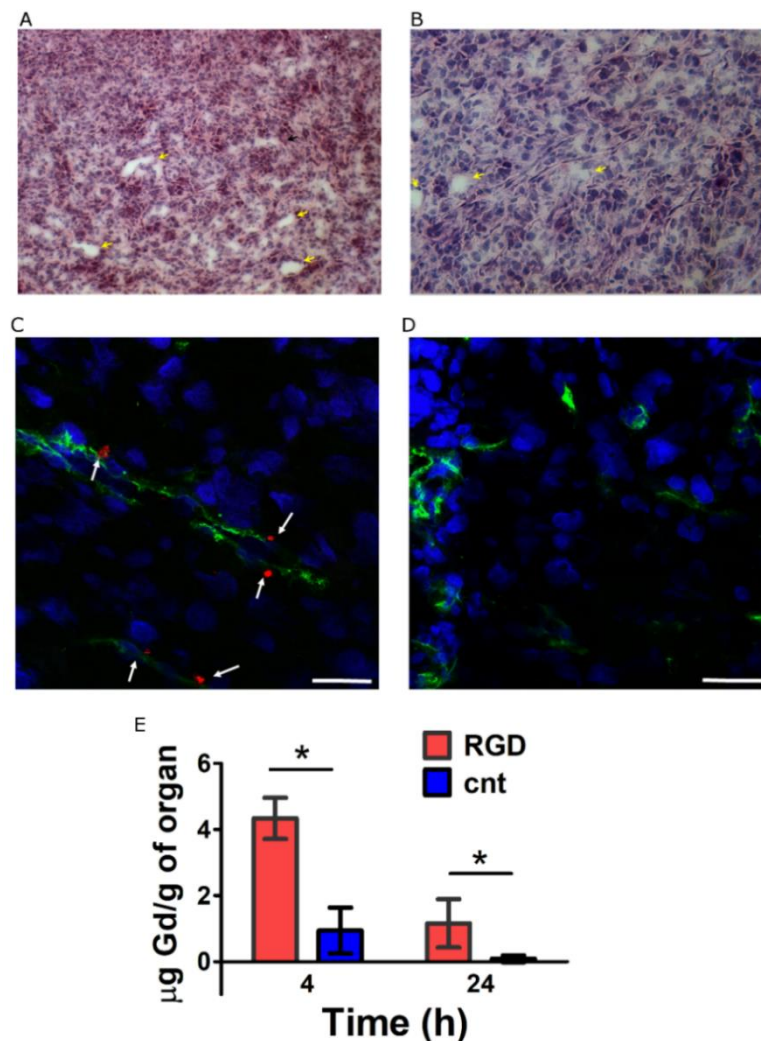


Figure 5. (A,B) H/E histology of representative tumors (10X and 20X, respectively). (C, D) CD-31 fluorescence staining of representative tumors from mice treated with either RGD-Gd GUVs or ctrl-Gd GUVs, respectively. *Green*=Vessels (CD-31/NG-2/CD-105), *Blue*=Nuclei (To-Pro) and *Red*=GUVs (rhodamine). Scale bar=10 μm. (E) ICP-MS quantification of Gd-content in tumors.

After the completion of the MRI experiments, the mice were sacrificed and tumors were explanted for histology and ICP-MS analyses. The H/E staining of the tumors (Fig.5A, B) shows homogeneous tumor growth with consistent and regular vascularization (*yellow arrows*) and the absence of necrotic regions. These features were confirmed for all tested tumors. The CD-31 fluorescence staining of the slices showed that the GUVs were only bound to vessels in Group2 mice (*i.e.* those ones treated with RGD-Gd GUVs) (Fig.5C *white arrows*), and not those in Group1 (*i.e.* those ones treated with ctrl-Gd GUVs) (Fig.5D).

Finally, the quantification of Gd(III) content in the tumors was carried out using the ICP-MS technique. As reported in Fig. 5E, the amount of Gd(III) is higher in tumors from Group2 than in those in Group1, both at $t=4$ h and $t=24$ h (P -value < 0.05). In Group2 tumors, $4.2 \mu\text{g Gd/g}$ of tumor and $1.6 \mu\text{g Gd/g}$ of tumor are present at $t=4$ h and $t=24$ h, respectively.

Discussion

The ability to target cancer cells,^{2,15} and visualize them using a high-resolution imaging technique, such as MRI,^{2,4} is one of the most important goals of molecular imaging. Undoubtedly, detecting cancer cells at an early stage by MRI is of huge importance, and will allow the primary role of this diagnostic approach to be further enhanced within the field of oncology.² Unfortunately, the intrinsically low sensitivity of MRI means that reaching the detection threshold in targeting experiments is challenging. Many attempts to obtain T_{1w} and/or T_{2w} images of cancer cells upon the administration of targeted contrast agents have been carried out over the last two decades.^{4-8,15} The use of T_1 contrast agents has not provided convincing results, especially when targeted epitopes are sparse.⁴¹

In this work, we have explored a new way to tackle the sensitivity drawbacks of MRI by exploiting the synergy offered by two strategies: *i*) RGD-Containing Giant Unilamellar Vesicles (GUVs); and *ii*) MRI detection based on the assessment of Magnetization Transfer Contrast (MTC) as an alternative to the commonly used T_{1w} images that are acquired in the presence of paramagnetic GBCAs.^{20, 26-28}

GUVs were chosen as they are biocompatible carriers that can be loaded with high payloads of T_1 Gd-based MRI CAs both encapsulated in the large inner cavity and incorporated into the phospholipidic membrane.

The inner cavity was filled with a HEPES/NaCl buffer solution containing 40 mM of Gd-HPDO3A. Although the Gd-HPDO3A dose can be increased up to 300 mM without any osmolarity problems, this did not appear to be convenient because of the occurrence of relaxivity “quenching” upon increasing the amount of entrapped Gd-complexes. This is due to the low water permeability of the GUV membrane.⁴²⁻⁴⁴ For this reason, and in order to increase the attainable relaxivity, the amphiphilic Gd-complex was inserted into the GUV membrane. The Gd-complexes exposed on the outside of the GUVs did not show any drawbacks in their function as agents that shorten the T_1 of water.

The ability to easily functionalize the surfaces of phospholipid vesicles (*e.g.* GUVs, SUVs, micelles, etc.) with targeting moieties is a particular advantage.^{23,33} Cyclic RGD has been used, herein, for its binding to integrins. The RGD tripeptide (Arg-Gly-Asp) is an amino acid sequence that is largely

present in many extracellular matrix proteins (*e.g.* fibronectin, vitronectin, laminin, etc.) and is responsible for cell-cell and cell-matrix adhesion. This sequence is recognized by a number of integrin proteins, including $\alpha\beta_3$, $\alpha_5\beta_1$ and $\alpha 11\beta_3$. There is a large overexpression of integrins on the outer surface of solid tumors, and they play an important role in tumor proliferation, invasiveness and metastasis formation.^{45,46}

Furthermore, integrin expression is also increased in endothelial cell surfaces during neo-angiogenesis, to facilitate the growth and survival of newly forming vessels.^{47,48}

These liposomes have micrometric diameter (1.5-2 μm) and a slightly negative surface ζ -potential, making them suitable for extravascular/extracellular targeting. No significant differences between RGD-Gd GUVs and ctrl-Gd GUVs were reported. As previously reported,²³ they are only slightly internalized by macrophages, as observed in *in vitro* experiments. Furthermore, no evidence of cell toxicity is present in either the targeted or untargeted formulations.

The targeting was efficient and specific. Only in the presence of RGD moiety can the GUV bind integrin-overexpressing cells. It is worth noting that RGD GUVs cannot be internalized by cells, and remain attached to the external surface, although they cluster into specific regions of cytoplasmic membranes.

The feasibility of using RGD-Gd GUVs for the MRI detection of cancer cells was assessed both *in vitro* and *in vivo* by acquiring T_{1w} , T_{2w} and MTC MR images at 7T.

U-87 MG glioblastoma cells were chosen for the *in-vitro* experiments as they are characterized by a very high expression of RGD receptors, *ca.* 10^5 receptors per cell.⁴⁹

Validation was carried out using fluorescent microscopy and ICP-MS for Gd(III) quantification.

The use of RGD-Gd GUVs allows a very large amount of GBCAs to be carried to the site of interest. This amount is one order of magnitude higher than the amount obtained with the use of ctrl-Gd GUVs (*i.e.* 1.2×10^8 vs. 8.2×10^6 Gd³⁺/cell), which is, nevertheless, lower than the typical threshold reported for cell detection by T_{1w} MRI. In fact, some years ago, an empirical relationship to relate the threshold for MRI detection to relaxivity (r_{1p}) and the number (N) of Gd-complexes associated to each cell was proposed:⁸

$$N = 10^9 / r_{1p}$$

Considering that the r_{1p} of RGD-Gd GUVs at 7 T is lower than $2 \text{ mM}^{-1}\text{s}^{-1}$, the number of Gd-complexes present in cell pellets, after binding RGD-Gd GUVs onto the external surfaces of cells, is *ca.* 4-5 times lower than the detection threshold. This clearly justifies the absence of detectable T_1 contrast upon the incubation of the U-87 MG cells in the presence of RGD-Gd GUVs. It is likely that T_{1w} images would have reported the targeting of RGD-Gd GUVs at a lower field strength, such as 0.5 T, as the measured r_{1p} value at this field strength was found to be $5.5 \text{ mM}^{-1}\text{s}^{-1}$. The higher relaxivity observed at 0.5 than at 7T reflects, on the one hand, the important contribution provided by the Gd-complexes that are exposed on the surface of the liposome's membrane and, on the other, the limited exchange of water molecules across the vesicle's membrane, which leads to the "quenching" of the attainable relaxivity that is associated with the large amount of Gd-HPDO3A in the inner aqueous cavity.⁴²⁻⁴⁴ Although this has not yet been analyzed in detail, it is apparent that water-proton relaxation arises mainly from the exposed Gd-complexes that, being part of a

supramolecular and slowly moving system, generate a relaxivity “hump” around a field strength of 1T. The relaxivity of the Gd-GUVs used in this work decreases to lower values as the field strength increases (it is $< 2\text{mM}^{-1}\text{s}^{-1}$ at 7T). More work is necessary if the permeability of GUV membranes is to be controlled to take full advantage of the large paramagnetic payload that such systems are capable of delivering.

As expected, better results were obtained by quantifying the T_2 effect. In fact, in this case, cells are detectable upon incubation in the presence of RGD-Gd GUVs, with a ΔR_2 of 18.3% compared to control unlabeled cells. No significant ΔR_2 effect is present in cells upon incubation with ctrl-Gd GUVs.

MRI has traditionally been based on the exploitation of changes in proton density and the T_1 / T_2 relaxation times of tissue water protons. About three decades ago, a new form of tissue contrast was reported; Magnetization Transfer Contrast (MTC). It is based on the concept that tissues contain two, or more, separate populations of water molecules: i) a highly mobile (*free*) water pool; and ii) an immobile, semi-solid (restricted) water pool. This latter is made up of water molecules bound to large macromolecules (*e.g.* ECM proteins, cellular membranes, etc.).

The NMR signal of immobilized water protons is normally not visible because of their very short T_2 relaxation time (bandwidth > 10 KHz). Upon applying *rf* irradiation (at a chemical shift far from the bulk water resonance, with saturation over a very large bandwidth, *e.g.* 50 KHz), the saturated protons may enter the free bulk water proton pool (bandwidth $< 20\text{Hz}$) thus transferring their saturated magnetization to the free water protons. As consequence, there is a decrease in the visible MR signal and consequently the generation of contrast in regions in which the immobilized water molecules/proteins are present.²⁶⁻²⁸

MTC MRI has been widely investigated, at both clinical and preclinical levels, and the intrinsic differences in MTC between tissues have been exploited without the need to administer exogenous CAs.^{50,51}

The theoretical relationship between the MTC effect and water T_1 has been widely investigated.²⁶⁻²⁸ Our aim is to assess whether this approach is even more sensitive than the usual effects of paramagnetic agents in T_{1w} MR images. In a previous work, we proved that Gd-labelled cells can be detected better by MTC than via the acquisition of T_{1w} images.²⁰ Our current *in-vitro* experiments on U-87 MG cells have confirmed these previous observations. In fact, cells that were incubated in the presence of RGD-Gd GUVs were detectable by MTC-MRI. In particular, *ca.* 15% contrast difference was observed between the cells incubated with targeted-GUVs and the cells incubated in the presence of ctrl-Gd GUVs. Hence, when T_1 cannot detect U-87 MG cells, MTC succeeds in providing improved sensitivity.

Using the positive *in-vitro* results as a base, we carried out *in vivo* experiments with the aim of exploring whether the advantages offered by MTC can be translated to *in vivo* studies.

Mice underwent MRI examination when tumors reached a growth stage in which neo-angiogenesis and epithelial-mesenchymal transition events occur, but when necrotic areas are still not present; the tumors appeared to be well vascularized and perfused.

Analogously to the *in vitro* experiments, *in vivo* T_2 and T_1 contrast also failed to distinguish the tumors of mice injected with RGD- and ctrl-Gd GUVs. However, MTC was successful as it detected

the pharmacokinetics of the GUVs in the tumor region. The MTC data suggest that the RGD-Gd GUVs were specifically bound to the glioblastoma tumor with a maximum effect around $t=4$ h (MTC% contrast of *ca.* 16%).

ICP-MS confirmed the specific accumulation of GBCAs, upon use of RGD-Gd GUVs. In fact, the amount of Gd found in the tumors upon the administration of the targeted GUVs is *ca.* 4 and 8 times higher than those of Gd found in tumors upon the administration of control untargeted GUVs (at $t=0$ and $t=4$ h, respectively). Finally, the CD-31 fluorescence staining of the tumor slices indicated that a significant fraction of the RGD-Gd GUVs was bound to vessels in mice.

It should be noted that the GUVs cannot escape the vascular space *in vivo*, and this means that *in-vitro* and *in-vivo* RGD-targeting experiments are slightly different. In fact, the *in-vitro* experiments demonstrated that RGD GUVs directly bind the RGD that is overexpressed in U-87 MG cells (note that *ca.* 10^5 RGD receptors are present for each U-87 MG cell).⁴⁷ Hence, it can be stated that RGD GUVs directly bind tumor cells.

In the *in-vivo* experiments, although the xenografts consisted of U-87 MG glioblastoma cells, the observed MTC effects cannot be associated to GUV's binding of tumor cells as the size of the GUV particles hamper their extravasation from the vascular space. It follows that the observed effect relies on the binding of the integrins that are present on the surface of tumor endothelial cells (TECs). As widely reported in cancer-related literature, integrin expression is strongly increased in endothelial cell surfaces during neo-angiogenesis to facilitate the growth and survival of newly forming vessels. Tumor endothelial cells are markedly different from normal endothelial cells (NECs).⁵² This transition from NECs to TECs is triggered by the presence of tumor cells *via* several mechanisms, including: i) transdifferentiation, *i.e.* tumor cells, cancer stem cells or vascular progenitor cells might directly transdifferentiate into TECs; and ii) cell fusion, *i.e.* malignant tumor cells can fuse with NECs or circulating vascular progenitor cells. Both mechanisms lead to the over-expression of integrins on endothelial-cell surfaces.

Conclusions

Altogether, the herein reported data show that a protocol for the efficient detection of integrins that are overexpressed on glioblastoma tumors is possible.

The use of GUVs appears to be a good strategy for the delivery of a high amount of Gd-based MRI contrast agents to the tumor region. They appear to improve the sensitivity threshold of small unilamellar liposomes, while preserving their main advantages. In fact, they are biocompatible and easily loaded with contrast agents, just like as small liposomes, but they are neither sequestered by macrophages nor internalized inside cells *in vivo*. Moreover, their inner cavity can host a very large number of Gd-complexes.²³ However, although giant liposomes are able to deliver high Gd-complex amounts to the cancer region via the binding of overexpressed integrins, Gd concentration in the region of interest appears to be just at the threshold for the detection of the relaxation enhancement effects using conventional T_{1w} and T_{2w} images.

MTC MRI has been confirmed to possess higher sensitivity for the detection of the small effects that are associated with the presence of paramagnetic Gd-complexes than their $T_{1/2w}$ counterparts.

In conclusion, the synergic properties of applying RGD-Gd GUVs and the MTC-MRI technique have led to the successful visualization of the targeting of tumor integrins. The findings reported herein are promising for the development of new procedures for the preclinical targeting of epitopes that are expressed at low doses on the external surfaces of cells. More generally, the combination of MTC and GBCAs deserves more attention as it is a valid alternative to classical T_{1w} and T_{2w} MRI approaches.

Experimental

Chemicals: ProHance (Gadoteridol, Gd-HPDO3A) was a gift provided by Bracco Imaging S.p.A.³⁰ 1,2-dipalmitoyl-*sn*-glycero-3-phosphocholine (DPPC), 1,2-distearoyl-*sn*-glycero-3-phosphoethanolamine-N-[methoxy(polyethylene glycol)-2000] (ammonium salt) (DSPE-mPEG2000), 1,2-dioleoyl-*sn*-glycero-3-phosphoethanolamine-N-(lissamine rhodamine B sulfonyl) (ammonium salt) (Liss Rhod PE) and 1,2-distearoyl-*sn*-glycero-3-phosphoethanolamine-N-[maleimide(polyethylene glycol)-2000] (ammonium salt) were purchased from Avanti Polar Lipids Inc. (Fig.6).

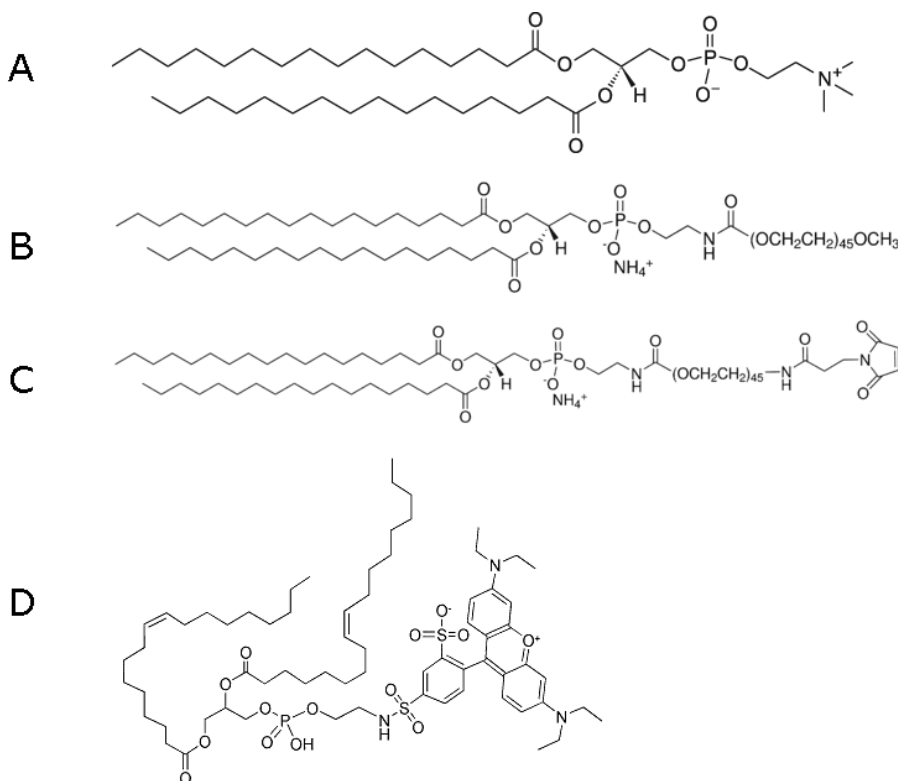


Figure 6. Chemical structure of phospholipid used for preparation of GUVs. (A) 1,2-dipalmitoyl-*sn*-glycero-3-phosphocholine (DPPC); (B) 1,2-distearoyl-*sn*-glycero-3-phosphoethanolamine-N-[methoxy(polyethylene glycol)-2000] (ammonium salt) (DSPE-mPEG2000), (C) 1,2-distearoyl-*sn*-glycero-3-phosphoethanolamine-N-[maleimide(polyethylene glycol)-2000] (ammonium salt). (D) 1,2-dioleoyl-*sn*-glycero-3-phosphoethanolamine-N-(lissamine rhodamine B sulfonyl) (ammonium salt) (Liss Rhod PE).

A Gd-amphiphilic complex, Gd(III)-DOTAMA (C₁₈)₂,³¹ was synthesized as previously reported (Fig.7).

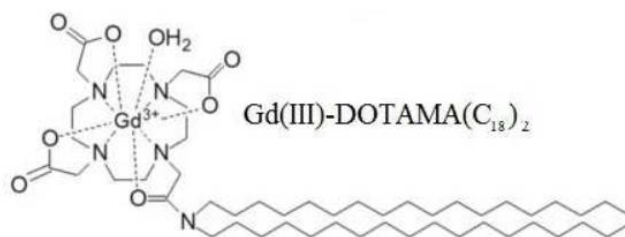


Figure 7. Chemical structure of Gd-amphiphilic complex used for preparation of GUVs, Gd(III)-DOTAMA(C₁₈)₂.

The presence of free Gd-ions was checked using the Orange xylenol procedure and was lower than 0.3% *mol/mol*.³² The exact Gd-complex concentration was checked using a relaxometric approach, as previously reported.

Cyclo(-Arg-Gly-Asp-D-Phe-Cys) acetate salt, hereinafter indicated as c(RGDfC), was purchased from Bachem AG (Bubendorf, De) (Fig.8).

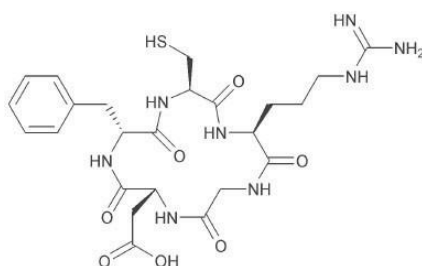


Figure 8. Cyclo(-Arg-Gly-Asp-D-Phe-Cys) acetate salt, c(RGDfC), used for preparation of GUVs.

Fluorescein-Isothiocyanate-labelled Phalloidin, from *Amanita phalloides*, hereinafter indicated as Phalloidin-FITC, was purchased from Sigma-Aldrich Co. LLC and used without further purification. Sodium chloride, sodium acetate, HEPES (4-(2-hydroxyethyl)-1-piperazineethane-sulfonic acid), sodium hydroxide, hydrochloric acid, nitric acid, chloroform and all other chemicals were acquired from Sigma-Aldrich Co. LLC and used without further purification.

Giant liposomes (GUVs) preparation: Giant liposomes were prepared according to a procedure reported in the literature with modifications.^{23,33}

Membranes were prepared using the following formulations:

- RGD-Gd GUVs: DPPC (86.95%), Gd-amphiphilic complex (10%), DSPE-PEG2000Maleimide (3%), 18:1 Liss Rhod PE (0.05%) (*moles %*);
- ctrl-Gd GUVs: DPPC (86.95%), Gd-amphiphilic complex (10%), DSPE-mPEG2000 (3%) 18:1 Liss Rhod (0.05%) (*moles %*).

Briefly, the desired blend of phospholipids is dried until a film is formed at the bottom of a flask. The hydration solution was then added. 40 mM Gd-HPDO3A in HEPES/NaCl buffer (3.8 mM HEPES, 0.15 M NaCl, pH 7.2 ± 0.1) was used for both GUV formulations. The system was left for 2 h at 60°C without any mechanical stress to allow the vesicles to close and internalize the hydration solution within the inner cavity. The GUVs were then pelleted by centrifugation, washed with fresh

HEPES/NaCl buffer and purified from any non-internalized hydration solution, impurities or (if present) small liposome populations that may have remained in the supernatant.

GUV size was determined using confocal fluorescence microscopy on a fluorescent formulation (0.05% Liss Rhod PE in the membrane and 20 μM 5(6)-carboxyfluorescein in the cavity). Z-stack images were acquired in order to center every vesicle in its main diameter in order to be suitably manually measured. Dynamic Light Scattering (DLS) measurements confirmed the absence of liposome populations of between 50 nm and 800 nm.

The molar concentration of small and giant vesicles was evaluated using the reported formula, with modifications (1,2):³⁴

$$[\text{Liposomes}] = \frac{[\text{Gd}]_i \times 1L}{V_i \times [\text{Gd}]_{\text{intra lipo}}} = \frac{[\text{Gd}]_i \times 1L}{\frac{4}{3}\pi r^3 \times [\text{Gd}]_{\text{intra lipo}}} \quad (1)$$

where

$$[\text{Gd}]_i = [\text{Gd}]_{\text{TOT}} - [\text{Gd}]_m \quad (2)$$

$[\text{Gd}]_{\text{TOT}}$ is determined *via* the acidic digestion of the sample and quantification of Gd^{3+} by ICP-MS, $[\text{Gd}]_m$ is the amount of Gd present in the membrane, r is the radius of the vesicle, $[\text{Gd}]_{\text{intra lipo}}$ is assumed to be the same as that of the hydration solution.

c(RGDfC) was attached by chemical ligation.³⁵ Briefly, GUVs were suspended in HEPES/NaCl buffer and centrifuged to obtain pellets. They were then suspended in 0.15 M sodium acetate buffer (pH=6.8). An excess of c(RGDfC) was then slowly added to the GUVs suspension, which was gently agitated for 4 h, under a N_2 atmosphere. Finally, GUVs were centrifuged and washed two times with fresh HEPES/NaCl buffer.

Cell cultures: Human glioblastoma U-87 MG cells were used for experiments (ATCC n° HTB-14). They were cultured in Eagle Minimum Essential Medium (EMEM) supplemented with 10% fetal bovine serum (FBS), 2 mM glutamine, 100 U/mL penicillin and 100 $\mu\text{g}/\text{mL}$ streptomycin. Cells were seeded in 75- cm^2 flasks at a density of ca. 2×10^4 cells/ cm^2 in a humidified 5% CO_2 incubator at 37 $^\circ\text{C}$. At confluence, they were detached by adding 1 mL of a Trypsin-EDTA solution (0.25 % (w/v) Trypsin-0.53 mM EDTA).

Cells were negative for mycoplasma, as tested using the MycoAlert™ Mycoplasma Detection Kit (Lonza Sales AG-EuroClone S.p.A., Milano, It). All cell media and supplements were purchased from Lonza Sales AG-EuroClone S.p.A. (Milano, It).

Cytotoxicity assay: Preliminary tests to assess the toxicity of GUVs were carried out using U-87 MG cancer cells in the MTT assay.³⁶ Cells were seeded into 96-well tissue culture plates (10^4 cells per plate) 24 h before the experiment. They were then incubated with fresh complete medium in the presence of RGD-Gd GUVs or ctrl-Gd-GUVs (concentration of vesicles is 0÷20 pM).

After incubation, the medium was removed, the cells were washed and re-incubated in the presence of fresh medium supplemented with 0.5 mg/mL MTT (Thiazolyl Blue Tetrazolium Bromide, Sigma Aldrich) for 4 h in a humidified 5% CO_2 incubator at 37 $^\circ\text{C}$. Then, the MTT solution was removed and the plates were filled with DMSO (0.1 mL for plate) for $\frac{1}{2}$ h at room temperature, under gentle agitation, to allow the formazan crystals to solubilize. The absorbance of the resulting

colored solutions was quantified using a 96-multiwell iMark Bio-Rad microplate Reader ($\lambda = 570$ nm). The percentage of viable cells was calculated on the basis of the control blank cells using the following formula (3):

$$Viable\ cells\ \% = \frac{Abs - T}{Abs - cnt} \times 100 \quad (3)$$

Where Abs-T is the mean absorbance of the treated cells and Abs-cnt is the mean absorbance of the control untreated cells (after subtraction of the absorption of empty plates as background). Cell experiments were repeated in triplicate and the data are reported as mean \pm standard deviation. The blank was repeated 10 times.

Cell labelling: Human glioblastoma U-87 MG cells (8×10^5) were seeded in 6-cm Petri dishes containing 3 mL of complete EMEM medium and were placed in a humidified 5% CO₂ incubator at 37°C. The day after, when cells had reached *ca.* 70-80% confluence, they were incubated in fresh medium in the presence of either ctrl-Gd GUVs or RGD-Gd GUVs (concentration of vesicles is *ca.* 4 pM), for 30 min at 37°C. The cells were then washed 3-times with fresh PBS and detached using a non-enzymatic cell dissociation solution (Lonza Sales AG-EuroClone S.p.A., Milano, It). Finally, cells were loaded into glass capillaries and centrifuged at 1200 rpm for 5 min to give pellets for MRI acquisition.

Animals: The *in vivo* experiments were performed on male athymic nude mice (Fox 1 nu/nu, Envigo) of 7-8 weeks of age and a weight of 21 ± 2 g. The mice were kept in standard housing with standard rodent chow, water available *ad libitum* and a 12 h light/dark cycle.

Experiments were performed according to the Amsterdam Protocol on Animal Protection, in conformity with institutional guidelines that are in compliance with national laws (D.L.vo 116/92, D.L.vo 26/2014 and following additions) and international laws and policies (2010/63/EU, EEC Council Directive 86/609, OJL 358, Dec 1987, NIH Guide for the Care and Use of Laboratory Animals, U.S. National Research Council, 1996).

For tumor-model preparation, mice were anesthetized *via* an intramuscular injection of tiletamine/zolazepam (Zoletil 100; Virbac, Milan, Italy) 20 mg/kg plus xylazine (Rompun; Bayer, Milan, Italy) 5 mg/kg using a 27-G syringe. *Ca.* 1×10^6 human glioblastoma U-87 MG cells were suspended in 0.1 mL of PBS and subcutaneously injected into each leg of 8-week-old male mice (N=6, a low animal number in agreement with the 3R principles for the use of animals). Two tumors were implanted into each mouse, to double the number of analyzed tumors.

Animals were monitored by caliper weekly for changes in tumor size. MRI was performed 15 days after tumor-cell implantation when the mean tumor volume was 180 ± 30 mm³.

For the MRI experiments, mice were anesthetized *via* the intramuscular injection of tiletamine/zolazepam (Zoletil 100; Virbac, Milan, Italy) 20 mg/kg plus xylazine (Rompun; Bayer, Milan, Italy) 5 mg/kg using a 27-G syringe.

Permanent vein access was obtained by inserting a PE10 catheter into the tail vein (27-G needle). The animal study protocol is reported in Fig.4A. Briefly, pre-MR images were acquired 15 days

after tumor implantation. MR images were then acquired at t=0, t=4 h and t=24 h after the administration of GUVs. Mice were divided into two groups. The first group was injected with RGD-Gd GUVs (0.05 mmol Gd/kg), and the second group was injected with ctrl-Gd GUVs (0.05 mmol Gd/kg), i.e. the low range doses of current clinical GBCAs.

The injection of GUVs was performed via slow infusion (0.1 mL/min - 0.25 mL) using an infusion pump (Phd 22/2000 MRI compatible infusion/withdrawal remote programmable dual syringe pump, Harvard Apparatus), to ensure that the GUV-administration protocol was safe.

MRI acquisition and data analysis: MRI scans were acquired at 7 T on a Bruker Avance 300 spectrometer equipped with the Micro 2.5 microimaging probe. T_{1W} images were acquired using a standard MSME (multislice multiecho) sequence with the following parameters (TR = 250 ms, TE = 3.3 s, FOV = 1 cm x 1 cm, slice thickness = 1 mm, matrix size 128 x 128). T_{2W} images were acquired using a standard RARE (Rapid Acquisition with Refocused Echoes) sequence with the following parameters (TR = 4000 ms, TE = 5.5 s, FOV = 1 cm x 1 cm, slice thickness = 1 mm, RARE factor = 32, matrix size 128 x 128). T_1 values were measured using a Saturation Recovery Spin Echo sequence (TE = 3.8 ms, 10 variable TRs ranging from 50 to 5000 ms, FOV = 1 cm x 1 cm, slice thickness = 1 mm, matrix size 128 x 128). T_2 values were measured using a MSME sequence (TR = 2000 ms, 20 variable TEs ranging from 11 to 500 ms, FOV = 1 cm x 1 cm, slice thickness = 1 mm, matrix size 128 x 128).

The T_1 contrast enhancement ($T_{1\ enh}\%$) was calculated as follows (4):

$$T_{1\ enh}\% = \frac{SI_w - SI_{w/o}}{SI_{w/o}} \times 100 \quad (4)$$

where SI_w and $SI_{w/o}$ are the normalized MR signal intensities for pellets that contained and did not contain the Gd(III)-labelled cells, respectively.

Analogously, the T_2 contrast was calculated as negative enhancement ($T_{2\ enh}\%$) using the following expression (5):

$$T_{2\ enh}\% = \frac{SI_w - SI_{w/o}}{SI_{w/o}} \times 100 \quad (5)$$

In order to evaluate the Magnetization Transfer (MT) effect, Z-spectra were acquired in the ± 300 ppm range. A typical RARE spin-echo sequence with an echo time of 3 ms and a TR value of 8 s was used. An isotropic 64×64 acquisition matrix with FOVs of 10×10 mm², for *in-vitro* experiments, and 30×30 mm², for *in vivo* experiments, and a slice thickness of 1 mm were used. The whole sequence was preceded by a saturation scheme consisting of a 3-sec-long continuous rectangular wave pulse at a radiofrequency B_1 intensity of either 3, 6 or 12 μ T (only $B_1 = 6$ μ T for *in-vivo* experiments). The Z-spectra were analyzed using custom-made software and were compiled in the MATLAB platform.

The MTC effect was measured using the following equation (6):

$$MTC_{enh}\% = \frac{SI_{RGD} - SI_{ctrl}}{SI_{ctrl}} \times 100 \quad (6)$$

where SI_{RGD} and SI_{ctrl} are the normalized MR signal intensities in the Z-spectrum at 16 ppm, in the presence of RGD-Gd GUVs and ctrl-Gd GUVs respectively.

ICP-MS: After the MRI experiments were completed, the animals were sacrificed and the tumors were explanted, weighed and processed for ICP-MS analysis using reported procedures.¹¹ The explanted tissue was treated by adding 1 mL of concentrated HNO₃ (70%) to each sample. After the complete dissolution of the tissues, the samples were further digested using microwave heating (MicroSYNTH, Microwave labstation equipped with an optical fiber temperature control and HPR-1000/6M six position high-pressure reactor, Milestone, Bergamo, Italy). After digestion, the volume of each sample was brought to 2 mL using ultrapure water. The solutions were then filtered with a 0.45 μm filter and analyzed by ICP-MS for the quantification of Gd³⁺, using a Thermo Scientific ELEMENT 2 ICP-MS-Finnigan, Rodano (MI). Quantification was obtained using a calibration curve that was measured using four gadolinium absorption standard solutions (Sigma-Aldrich) in the range 0.005–0.1 μg/mL. The total mass of the Gd³⁺ that was retained in each specimen was calculated with respect to the weight of the tumor tissue (as μg of Gd³⁺/g of tissue).

Confocal fluorescence microscopy of U-87 MG cells incubated in the presence of Gd-GUVs: 1.5 x 10⁴ U-87 MG cells were seeded into μ-Slide 8 Wells in the presence of fresh medium. One day later, they were incubated for 30 min with either Rhodamine-containing RGD-Gd GUVs or Rhodamine-containing ctrl-Gd GUVs (*ca.* 5.2 x 10⁶ vesicles per plate, red). After labelling, the cells were extensively and gently washed to remove any unbound liposomes. The cells were then stained with Phalloidin-FITC (green) solution for 30 min at RT. Subsequently, the cells were washed twice with fresh PBS and observed using confocal microscopy. Z-stack images were acquired on a Leica SP8 confocal system (Leica Microsystems), in order to acquire a series of parallel images along the Z-axis that could be used to reconstruct 3D images of the GUV-labelled cells. This allowed the effective number of GUVs that were bound to cells to be assessed. The following wavelengths were considered for microscopy: 1) λ_{ex}=545 nm, λ_{em}=567 nm for rhodamine-B; and 2) λ_{ex}=495 nm, λ_{em}=520 nm for Phalloidin-FITC. Fluorescent images were processed using ImageJ Fiji freeware software.

Hematoxylin/Eosin and CD-31 staining: After MRI acquisition, mice were sacrificed via cervical dislocation. Cancer tissues were excised, cut along the major axis and frozen into cold isopentane (-80°C overnight). Then, 4 μm sections were prepared, using cryotome, and fixed using ice-cold acetone for 8 min. This was followed by three washings with PBS. One slice was stained with hematoxylin/eosin (H/E stain) (BioOptica) and observed under an Olympus BX41 microscope equipped with a Leica photographic system for a histological characterization of the tumor.

For CD-31 staining and confocal fluorescence microscopy,³⁸ slices were incubated with 10% goat serum in PBS, 1 h, RT. They were then incubated in the presence of the primary antibody (rat anti-mouse CD-31 (Invitrogen, Life technologies, 1:200 in 10% goat serum in PBS) overnight at 4°C. Slices were washed three times with PBS (5 min, under agitation) and incubated in the presence of the secondary fluorescent antibody (Alexa Fluor 488 anti-rat antibody secondary Ab, Invitrogen, Life technologies, 1:500 in PBS), for 1 h at room temperature. Subsequently, the slices were washed 3 times with PBS (5 min, under agitation), and the nuclei were stained with TO-PRO-3 via incubation with the TO-PRO-3 staining solution (Thermo-Fisher Scientific) 1:1000 in PBS, for 10 min at room temperature. After 2 washings with PBS (5 min, under agitation), the sections were mounted using ProLong Mountant (Thermo-Fisher Scientific). Sections were imaged on a Leica SP8 confocal system (Leica Microsystems). The following wavelengths were considered for microscopy: 1) $\lambda_{\text{ex}}=545$ nm, $\lambda_{\text{em}}=567$ nm for rhodamine-B of GUVs (red); 2) $\lambda_{\text{ex}}=495$ nm, $\lambda_{\text{em}}=519$ nm for CD-31 staining (green); and 3) $\lambda_{\text{ex}}=642$ nm, $\lambda_{\text{em}}=661$ nm for TO-PRO-3 nuclei staining (blue).

Statistical analysis: All data are expressed as mean \pm standard deviation (N=6). The Graph-Pad Prism software was used for data analysis. The statistical analysis of the data was carried out using the unpaired two-tailed t-test. A P-value < 0.05 was taken to be statistically significant.

Supplementary figures

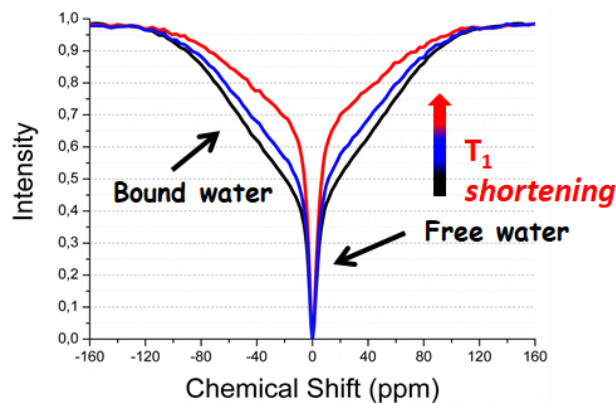


Figure S1. Representative Z-spectra in presence of increased amount of a T_1 -shortening agent.

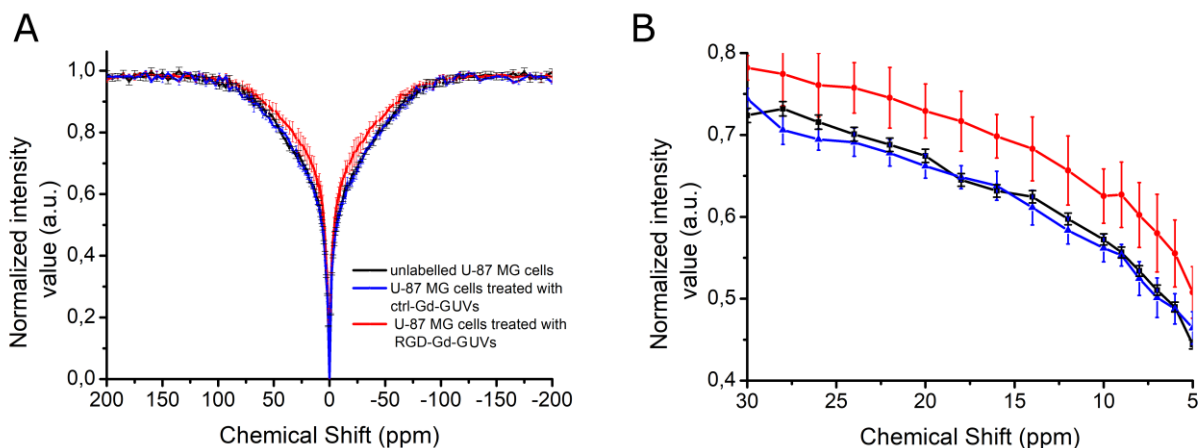


Figure S2. (A) Z-spectra of U-87 MG cells specimens ($B_1 = 3 \mu\text{T}$) and (B) magnification of Z-spectra in the 5-40 ppm region.

Chapter 4: MTC-MRI visualization of Gd-GUVs

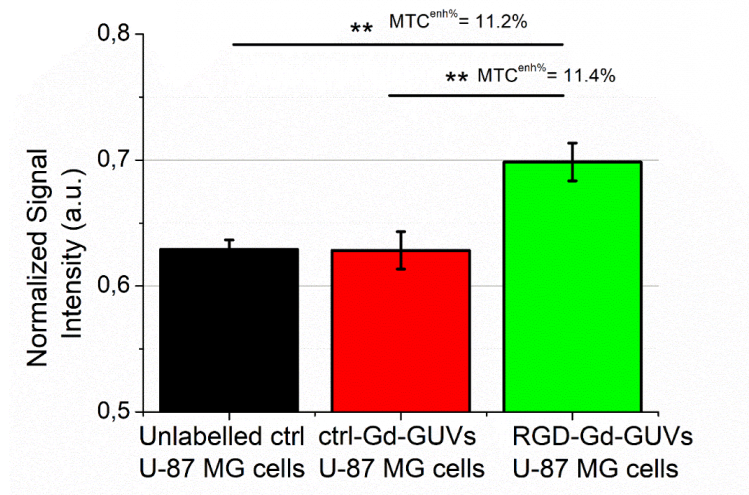


Figure S3. Normalized signal intensity of the three specimens from Z-spectra (for calculating $MTC^{enh\%}$), $B_1 = 3 \mu T$.

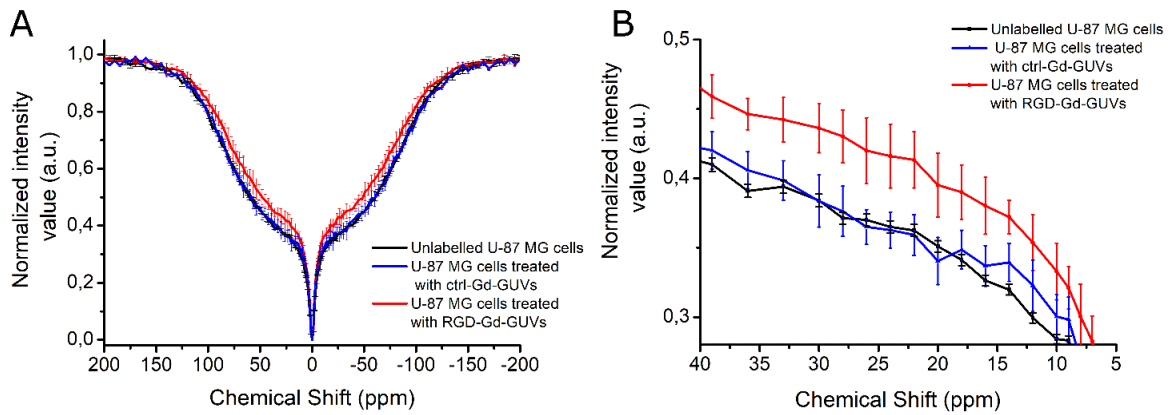


Figure S4. (A) Z-spectra of U-87 MG cells specimens ($B_1 = 12 \mu T$) and (B) magnification of Z-spectra in the 5-40 ppm region.

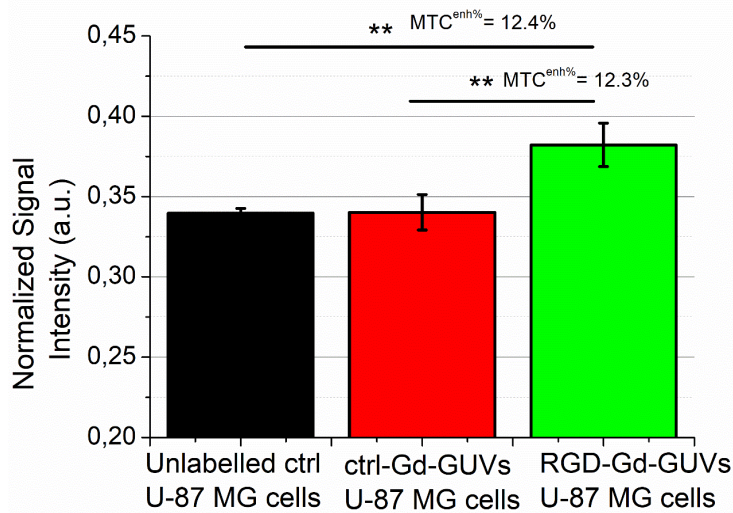


Figure S5. Normalized signal intensity of the three specimens from Z-spectra (for calculating $MTC^{enh\%}$), $B_1 = 12 \mu T$.

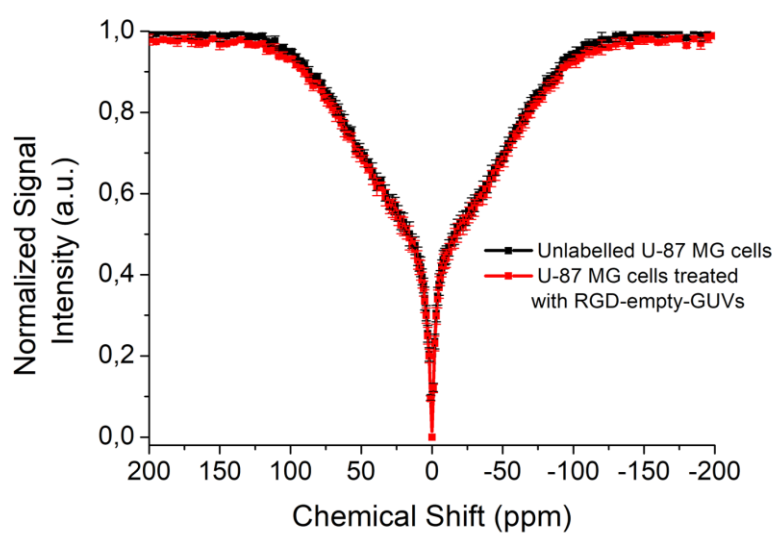


Figure S6. Z-spectra of untreated U-87 MG cells and treated with RGD-empty-GUVs ($B_1 = 12 \mu\text{T}$).

References

1. Bray, F., Ferlay, J., Soerjomataram, I., Siegel, R. L., Torre, L. A., & Jemal, A. (2018). Global cancer statistics 2018: GLOBOCAN estimates of incidence and mortality worldwide for 36 cancers in 185 countries. *CA: a cancer journal for clinicians*, 68(6), 394-424.
2. Penet, M. F., Artemov, D., Farahani, K., & Bhujwala, Z. M. (2013). MR-eyes for cancer: looking within an impenetrable disease. *NMR in Biomedicine*, 26(7), 745-755.
3. Frenzel, T., Lawaczeck, R., Taupitz, M., Jost, G., Lohrke, J., Sieber, M. A., & Pietsch, H. (2015). Contrast media for x-ray and magnetic resonance imaging: development, current status and future perspectives. *Investigative radiology*, 50(9), 671-678.
4. Wahsner, J., Gale, E. M., Rodríguez-Rodríguez, A., & Caravan, P. (2018). Chemistry of MRI contrast agents: current challenges and new frontiers. *Chemical reviews*, 119(2), 957-1057.
5. Sherry, A. D., Caravan, P., & Lenkinski, R. E. (2009). Primer on gadolinium chemistry. *Journal of Magnetic Resonance Imaging: An Official Journal of the International Society for Magnetic Resonance in Medicine*, 30(6), 1240-1248.
6. Geraldes, C. F., & Laurent, S. (2009). Classification and basic properties of contrast agents for magnetic resonance imaging. *Contrast media & molecular imaging*, 4(1), 1-23.
7. Pierre, V. C., Allen, M. J., & Caravan, P. (2014). Contrast agents for MRI: 30+ years and where are we going? *Journal of Biological Inorganic Chemistry*, 19, 127-131
8. Aime, S., Cabella, C., Colombatto, S., Geninatti Crich, S., Gianolio, E., & Maggioni, F. (2002). Insights into the use of paramagnetic Gd (III) complexes in MR-molecular imaging investigations. *Journal of Magnetic Resonance Imaging: An Official Journal of the International Society for Magnetic Resonance in Medicine*, 16(4), 394-406.
9. Le Fur, M., & Caravan, P. (2019). The biological fate of gadolinium-based MRI contrast agents: a call to action for bioinorganic chemists. *Metallomics*, 11(2), 240-254.
10. Frenzel, T., Apte, C., Jost, G., Schöckel, L., Lohrke, J., & Pietsch, H. (2017). Quantification and assessment of the chemical form of residual gadolinium in the brain after repeated administration of gadolinium-based contrast agents: comparative study in rats. *Investigative radiology*, 52(7), 396.
11. Di Gregorio, E., Ferrauto, G., Furlan, C., Lanzardo, S., Nuzzi, R., Gianolio, E., & Aime, S. (2018). The issue of gadolinium retained in tissues: insights on the role of metal complex stability by comparing metal uptake in murine tissues upon the concomitant administration of lanthanum-and gadolinium-diethylenetriaminopentaacetate. *Investigative radiology*, 53(3), 167-172.

12. Di Gregorio, E., Furlan, C., Atlante, S., Stefania, R., Gianolio, E., & Aime, S. (2020). Gadolinium retention in erythrocytes and leukocytes from human and murine blood upon treatment with gadolinium-based contrast agents for magnetic resonance imaging. *Investigative radiology*, 55(1), 30-37.
13. Strzeminska, I., Factor, C., Robert, P., Grindel, A. L., Comby, P. O., Szpunar, J., ... & Lobinski, R. (2020). Long-term evaluation of gadolinium retention in rat brain after single injection of a clinically relevant dose of gadolinium-based contrast agents. *Investigative radiology*, 55(3), 138.
14. Knobloch, G., Frenzel, T., Pietsch, H., & Jost, G. (2020). Signal enhancement and enhancement kinetics of gadobutrol, gadoteridol, and gadoterate meglumine in various body regions: a comparative animal study. *Investigative radiology*, 55(6), 367-373.
15. Strijkers, G. J., Kluza, E., Van Tilborg, G. A., van der Schaft, D. W., Griffioen, A. W., Mulder, W. J., & Nicolay, K. (2010). Paramagnetic and fluorescent liposomes for target-specific imaging and therapy of tumor angiogenesis. *Angiogenesis*, 13(2), 161-173.
16. Man, F., Lammers, T., & de Rosales, R. T. (2018). Imaging nanomedicine-based drug delivery: a review of clinical studies. *Molecular imaging and biology*, 20(5), 683-695.
17. V. P. Torchilin, V. Weissig, in *Liposomes: Practical Approach*, (2003). Oxford University Press, NY, USA, 2nd ed., pp. 4-7.
18. Chan, K. W., Bulte, J. W., & McMahon, M. T. (2014). Diamagnetic chemical exchange saturation transfer (diaCEST) liposomes: physicochemical properties and imaging applications. *Wiley Interdisciplinary Reviews: Nanomedicine and Nanobiotechnology*, 6(1), 111-124.
19. Jia, Y., Geng, K., Cheng, Y., Li, Y., Chen, Y., & Wu, R. (2020). Nanomedicine particles associated with chemical exchange saturation transfer contrast agents in biomedical applications. *Frontiers in chemistry*, 8, 326.
20. Delli Castelli, D., Ferrauto, G., Di Gregorio, E., Terreno, E., & Aime, S. (2015). Sensitive MRI detection of internalized T1 contrast agents using magnetization transfer contrast. *NMR in Biomedicine*, 28(12), 1663-1670.
21. Zhao, J. M., Har-el, Y. E., McMahon, M. T., Zhou, J., Sherry, A. D., Sgouros, G., ... & Van Zijl, P. C. (2008). Size-induced enhancement of chemical exchange saturation transfer (CEST) contrast in liposomes. *Journal of the American Chemical Society*, 130(15), 5178-5184.
22. Morales-Pennington, N. F., Wu, J., Farkas, E. R., Goh, S. L., Konyakhina, T. M., Zheng, J. Y., ... & Feigenson, G. W. (2010). GUV preparation and imaging: minimizing artifacts. *Biochimica et Biophysica Acta (BBA)-Biomembranes*, 1798(7), 1324-1332.

23. Tripepi, M., Ferrauto, G., Bennardi, P. O., Aime, S., & Delli Castelli, D. (2020). Multilamellar LipoCEST Agents Obtained from Osmotic Shrinkage of Paramagnetically Loaded Giant Unilamellar Vesicles (GUVs). *Angewandte Chemie*, 132(6), 2299-2303.
24. Ferrauto, G., Delli Castelli, D., Di Gregorio, E., Terreno, E., & Aime, S. (2016). LipoCEST and cellCEST imaging agents: opportunities and challenges. *Wiley Interdisciplinary Reviews: Nanomedicine and Nanobiotechnology*, 8(4), 602-618.
25. Langereis, S., Geelen, T., Grüll, H., Strijkers, G. J., & Nicolay, K. (2013). Paramagnetic liposomes for molecular MRI and MRI-guided drug delivery. *NMR in Biomedicine*, 26(7), 728-744.
26. Henkelman, R. M., Stanisz, G. J., & Graham, S. J. (2001). Magnetization transfer in MRI: a review. *NMR in Biomedicine: An International Journal Devoted to the Development and Application of Magnetic Resonance In Vivo*, 14(2), 57-64.
27. Knutsson, L., Xu, J., Ahlgren, A., & van Zijl, P. C. (2018). CEST, ASL, and magnetization transfer contrast: How similar pulse sequences detect different phenomena. *Magnetic resonance in medicine*, 80(4), 1320-1340.
28. Van Zijl, P. C., & Yadav, N. N. (2011). Chemical exchange saturation transfer (CEST): what is in a name and what isn't?. *Magnetic resonance in medicine*, 65(4), 927-948.
29. Pierre, V. C., & Allen, M. J. (Eds.). (2017). *Contrast agents for MRI: experimental methods*. Royal Society of Chemistry.
30. Runge, V. M. (2000). Safety of approved MR contrast media for intravenous injection. *Journal of Magnetic Resonance Imaging: An Official Journal of the International Society for Magnetic Resonance in Medicine*, 12(2), 205-213.
31. Anelli, P. L., Lattuada, L., Lorusso, V., Schneider, M., Tournier, H., & Uggeri, F. (2001). Mixed micelles containing lipophilic gadolinium complexes as MRA contrast agents. *Magnetic Resonance Materials in Physics, Biology and Medicine*, 12(2-3), 114-120.
32. Barge, A., Cravotto, G., Gianolio, E., & Fedeli, F. (2006). How to determine free Gd and free ligand in solution of Gd chelates. A technical note. *Contrast media & molecular imaging*, 1(5), 184-188.
33. Reeves, J. P., & Dowben, R. M. (1969). Formation and properties of thin-walled phospholipid vesicles. *Journal of cellular physiology*, 73(1), 49-60.
34. Mulas, G., Ferrauto, G., Dastrù, W., Anedda, R., Aime, S., & Terreno, E. (2015). Insights on the relaxation of liposomes encapsulating paramagnetic Ln-based complexes. *Magnetic resonance in medicine*, 74(2), 468-473.

35. Reulen, S. W., Brusselaars, W. W., Langereis, S., Mulder, W. J., Breurken, M., & Merkx, M. (2007). Protein– liposome conjugates using cysteine-lipids and native chemical ligation. *Bioconjugate chemistry*, 18(2), 590-596.
36. Garbison, K. E., Heinz, B. A., Lajiness, M. E., Weidner, J. R., & Sittampalam, G. S. (2015). Phospho-ERK assays. In *Assay Guidance Manual [Internet]*. Eli Lilly & Company and the National Center for Advancing Translational Sciences.
37. Ferrauto, G., Di Gregorio, E., Auboiron, V., Petit, M., Berger, F., Aime, S., & Lahrech, H. (2018). CEST-MRI for glioma pH quantification in mouse model: Validation by immunohistochemistry. *NMR in Biomedicine*, 31(11), e4005.
38. Ferrauto, G., Di Gregorio, E., Lanzardo, S., Ciolli, L., Iezzi, M., & Aime, S. (2018). Generation of multiparametric MRI maps by using Gd-labelled-RBCs reveals phenotypes and stages of murine prostate cancer. *Scientific reports*, 8(1), 1-13.
39. Ferrauto, G., Di Gregorio, E., Delli Castelli, D., & Aime, S. (2018). CEST-MRI studies of cells loaded with lanthanide shift reagents. *Magnetic resonance in medicine*, 80(4), 1626-1637.
40. Ferrauto, G., Castelli, D. D., Terreno, E., & Aime, S. (2013). In vivo MRI visualization of different cell populations labeled with PARACEST agents. *Magnetic resonance in medicine*, 69(6), 1703-1711.
41. Lanza, G. M., Winter, P. M., Neubauer, A. M., Caruthers, S. D., Hockett, F. D., & Wickline, S. A. (2005). ¹H/¹⁹F magnetic resonance molecular imaging with perfluorocarbon nanoparticles. *Current topics in developmental biology*, 70, 57-76.
42. Strijkers, G. J., Hak, S., Kok, M. B., Springer Jr, C. S., & Nicolay, K. (2009). Three-compartment T1 relaxation model for intracellular paramagnetic contrast agents. *Magnetic Resonance in Medicine: An Official Journal of the International Society for Magnetic Resonance in Medicine*, 61(5), 1049-1058.
43. Guenoun, J., Doeswijk, G. N., Krestin, G. P., & Bernsen, M. R. (2016). Compartmentalization of Gd liposomes: the quenching effect explained. *Contrast media & molecular imaging*, 11(2), 106-114.
44. Di Gregorio, E., Ferrauto, G., Gianolio, E., & Aime, S. (2013). Gd loading by hypotonic swelling: an efficient and safe route for cellular labeling. *Contrast media & molecular imaging*, 8(6), 475-486.
45. Hamidi, H., Pietilä, M., & Ivaska, J. (2016). The complexity of integrins in cancer and new scopes for therapeutic targeting. *British journal of cancer*, 115(9), 1017-1023.
46. Sökeland, G., & Schumacher, U. (2019). The functional role of integrins during intra-and extravasation within the metastatic cascade. *Molecular cancer*, 18(1), 1-19.

47. Weis, S. M., & Cheresh, D. A. (2011). αV integrins in angiogenesis and cancer. *Cold Spring Harbor perspectives in medicine*, 1(1), a006478.
48. Avraamides, C. J., Garmy-Susini, B., & Varner, J. A. (2008). Integrins in angiogenesis and lymphangiogenesis. *Nature Reviews Cancer*, 8(8), 604-617.
49. Zhang, X., Xiong, Z., Wu, Y., Cai, W., Tseng, J. R., Gambhir, S. S., & Chen, X. (2006). Quantitative PET imaging of tumor integrin $\alpha\beta 3$ expression with ^{18}F -FRGD2. *Journal of nuclear medicine*, 47(1), 113-121.
50. Mehta, R. C., Pike, G. B., & Enzmann, D. R. (1996). Magnetization transfer magnetic resonance imaging: a clinical review. *Topics in magnetic resonance imaging: TMRI*, 8(4), 214-230.
51. Maas, M. C., Litjens, G. J., Wright, A. J., Attenberger, U. I., Haider, M. A., Helbich, T. H., ... & Scheenen, T. W. (2019). A single-arm, multicenter validation study of prostate cancer localization and aggressiveness with a quantitative multiparametric magnetic resonance imaging approach. *Investigative radiology*, 54(7), 437-447.
52. Hida, K., Maishi, N., Annan, D. A., & Hida, Y. (2018). Contribution of tumor endothelial cells in cancer progression. *International journal of molecular sciences*, 19(5), 1272.

- Chapter 5 -

**LipHosomes: a new generation of reporters for
ligand/anti-ligand assays based on pH readout**

Martina Tripepi, Paolo Oronzo Bennardi, Giuseppe Ferrauto, Silvio Aime, Daniela Delli Castelli*

Published as Full Paper: *Analysis & Sensing*, 2020

Abstract

This work reports about a new class of liposomes (LipHosomes) designed to induce a change of pH upon releasing their content. pH-readout reports on the number of LipHosomes in the specimen.

LipHosomes were prepared by entrapping NaOH or bicarbonate buffer in the intravesicular compartment. The liposomes suspension was purified from untrapped compounds and brought to pH 7.0. The pH gradient between intra- and extra-liposomal compartments is maintained because the phospholipidic membrane works as a semipermeable membrane, without diffusion of ions across the membrane.

The release of the liposomal content triggers a quantifiable variation of the pH of the medium. This feature has been harnessed in analytical assays based on ligand/anti-ligand molecular recognition by exploiting the biotin-streptavidin binding scheme.

A pH difference of 0.2 units was observed upon the release of the payload from biotinylated LipHosomes bound to streptavidinated plates. The test showed an excellent sensitivity being able to reveal a concentration of bound LipHosomes in the sub-pM range.

Keywords: ELISA • Dosing method • Immunoassay • Liposome • pH readout

Introduction

Liposomes have been known since the middle of the last century, yet the research areas in which they find applications are still constantly growing.¹ According to their size, liposomes can be classified as Small Unilamellar Vesicles (SUV, diameter 20 – 100 nm), Large Unilamellar Vesicles (LUV, diameter > 100 nm), and Giant Unilamellar Vesicles (GUV, diameter > 1 μm).²

Up to now, SUVs and LUVs have been studied and exploited in the biomedical field to a larger extent rather than GUVs, having found important applications either *in vivo* (e.g. drug delivery)^{3,4} or in *in vitro* assays, where they act as reporter signal amplifiers.^{5,6}

Over the last 50 years, numerous and increasingly refined methods have been developed for the *in vitro* detection of diagnostic markers in biologic fluids, typically based on the antibody/antigen recognition (immunoassays).^{7,8} Among them, those based on the use of solid supports, on which the target molecule adheres or binds to in a specific way, display a very high efficiency. Enzyme-based immunoassays for various analytes have been subjected to intense scrutiny.⁹

One of the most applied technique for bio-molecular analysis is the enzyme-linked immunosorbent assay (ELISA). Briefly, ELISA-based methods consist of using chromatic variations induced by the antigen/antibody molecular recognition. For the detection of the antigen of interest, they require the use of a proper analytical tool, often represented by a spectrophotometer or a fluorimeter.

The sensitivity of the method falls in the pM range.¹⁰ Although good, the sensitivity is often challenged as many diagnostically relevant analytes are present in biological fluids at even lower concentration. Therefore, it appears necessary to push further down the sensitivity threshold. Other items that are considered relevant deal either with the need to reduce the analysis' costs and to access to quicker and reliable responses.

Magnetic immunoassays¹¹ and radio immunoassays¹² are variants of the ELISA method. Although they are potentially more sensitive than ELISA, the detection technology is definitively more expensive than the spectrophotometric readout.

A possible strategy for performing liposome-based immunoassays consists of replacing the enzyme by specific probes encapsulated into the liposome cavity that can be detected by colorimetric,¹³ fluorimetric,¹⁴ chemiluminometric,¹⁵ photothermic^{16,17} or electrochemical methods.¹⁸⁻²² The choice of the detection method is typically made on the basis of the equipment available in the laboratory. Specific antigens or antibodies can be introduced on the liposome surface by exploiting different routes.²³⁻²⁸ The procedures are well established and can be applied to a wide range of antigens and antibodies.²⁹

The herein reported work reports about the development of an innovative class of liposomes that can be quantified in a given specimen by a simple pH readout. The proposed method is based on the use of liposomal vesicles whose payload is represented by solutions characterized by a pH value different from the one of the medium in which they are suspended.

We call these systems with the name of LipHosomes. LipHosomes are liposomes capable of maintaining a pH gradient between the intra and extra media of the vesicles. Upon the release of the payload from the LipHosomes, a significant change in the pH of the medium occurs, that can be easily measured with a conventional pH-meter.

The herein reported results show how the proposed method is competitive in terms of the achievable sensitivity in respect to the currently available methods, with the great advantage of using a well-established, simple, fast responding, low cost detection technique as a laboratory pH-meter. Although different methods and strategies by using liposomes have been numerous reported for the bioassays on the basis of various signal-generation principles,¹³⁻²² there is no report focusing on liposome-based pH readout in the bioassays until now.

Moreover, the great advantage of the proposed method over existing ones relies in the reduction of the analysis costs. In fact, the vast majority of the existing methods make use of the reaction between enzymes and substrate to induce a variation of either absorbance or pH in the solution. The proposed method doesn't need of enzymes as amplification strategy, instead it makes use of bicarbonate or NaOH to induce a change in pH once these molecules are released from liposomes. The use of these very cheap reagents with respect to enzyme is supposed to drastically reduce the costs of the analysis kit. In addition, the reaction between enzyme and substrate is an additional step that causes the elongation of the analysis time and reduces the in-time stability of the response. In the present work, as to provide a proof of concept of the method, the analysis scheme and its sensitivity has been tested making advantage of the well-established binding couple biotin/streptavidin but this analysis set-up can be applied to a wide range of diagnostic biomarkers present in biological fluids. The application to a specific biomarker would be the subject of our next investigation to continue this study.

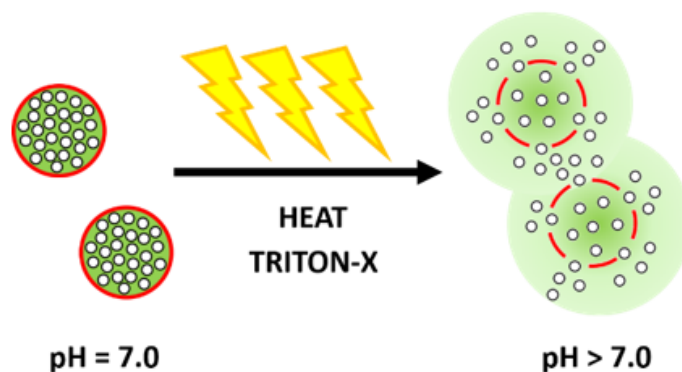
Results and discussion

Liposomes are vesicles made by phospholipid bilayers acting as semipermeable membranes. Small lipophilic molecules can cross the bilayer through a diffusion process driven by a concentration gradient (*e.g.* doxorubicin).^{30,31}

Viceversa hydrophilic ions are not expected to cross the phospholipid bilayer³² and this was the working hypothesis of the herein proposed method as it requires that the liposome membrane has to be impermeable to H_3O^+ and OH^- ions (to guarantee the pH gradient between intra- and extra-liposomal compartments). The first step of our project dealt with a careful control of the impermeability of the liposomal membrane to the electrolytes used to generate the pH in the inner aqueous cavity.

In the proposed method, the aqueous core of the liposomes was loaded with strong or weak basic substances.

To this purpose, different LipHosomes, either SUVs or GUVs, entrapping NaOH 1 mM (in NaCl 0.15 M) or bicarbonate buffer 0.15 M at pH 10, were tested. LipHosomes were prepared through the thin film hydration method (for SUVs) or the "gentle hydration" method (for GUVs)³³ in presence of the strong base or the buffer (See Experimental). The purification from the not entrapped material was carried out by neutralization in case of NaOH (by adding HCl, in NaCl 0.15 M) and by dialysis or ultrafiltration (carried out at pH 7 equilibrated with 0.15 M NaCl) in case of the bicarbonate buffer.



Scheme 1. Rupture of LipHosomes with release of their content and consequent variation of pH value.

The suspension of purified LipHosomes, isosmotic with the intraliposomal core, is neutral as long as the nanovesicles are intact. Then, LipHosomes were forced to release their content either by adding a surfactant as TRITON-X or by heating the liposomal suspension as sketched in Scheme 1.

Whatever is the chosen, upon destroying the liposomes, the released payload induced a variation in the pH value of the medium, measurable by a conventional pH-meter (endowed with a microelectrode suitable for measurements in 96-wells microplates containing 100 μ L of solution), that was correlated to the number of destroyed LipHosomes.

Table 1 reports the LipHosomes formulations investigated in this work.

Table 1. Formulations of the studied LipHosomes.

| Name | Membrane | Content |
|---------|---------------------------------|---------------------------|
| A (LUV) | DPPC/DSPE-PEG2000 95/5 | 1 mM NaOH - 0.15 M NaCl |
| B (LUV) | DPPC/DSPE-PEG2000 95/5 | 150 mM NaHCO ₃ |
| C (GUV) | DPPC/DSPE-PEG2000 97/3 | 150 mM NaHCO ₃ |
| D (GUV) | DPPC/DSPE-PEG2000Biotin 97/3 | 150 mM NaHCO ₃ |

The pH values of the suspensions containing LipHosomes of formulations A, B, and C did not vary over a period of three hours. Formulation C showed to be also stable upon incubation with human serum taken as model of biological fluid, as reported in the supporting information.

LipHosomes encapsulating NaOH

The pH values were calculated by considering that the concentration of OH⁻ released by a given number of LipHosomes in 1 L of solution is given by Equation 1:

$$\begin{aligned} [\text{OH}^-]_{\text{released}} &= \text{N}^\circ \text{ liposomes} \cdot (\text{mol of NaOH})_{\text{single liposome}} = \\ &= \text{N}^\circ \text{ liposomes} \cdot [\text{NaOH}]_{\text{single liposome}} \cdot V_{\text{inside liposome}} \end{aligned} \quad (1)$$

The number of liposomes can be easily converted in moles dividing by the Avogadro's number (NA) and, as the above relationship refers to 1 L of solution, the LipHosomes moles number corresponds to their molar concentration (Equation 2):

$$(\text{N}^\circ \text{ liposomes}/\text{NA})/1 \text{ L} = [\text{Liposomes}] \quad (2)$$

The proposed method is based on a pH readout before and after triggering the full release of the inner payload from the LipHosomes. The initial pH should be close around neutrality, but the release of the strong base will increase the concentration of OH⁻ ions in the suspension, thus increasing pH. The measured proton concentration is correlated to the OH⁻ concentration *via* the ionic product of water (K_w):

$$[\text{H}_3\text{O}^+] = \frac{K_w}{[\text{OH}^-]_{\text{equilibrium}}}$$

The charge balance of the suspension (considering that NaCl does not affect the calculations) is the following:

$$[\text{OH}^-]_{\text{equilibrium}} = [\text{Na}^+]_{\text{released}} + [\text{H}_3\text{O}^+]$$

$$\text{with } [\text{Na}^+]_{\text{released}} = [\text{OH}^-]_{\text{released}}$$

Combining the two equations above, it is possible to express [OH⁻]_{released} as a function of [OH⁻]_{equilibrium}:

$$[\text{OH}^-]_{\text{released}} = \frac{([\text{OH}^-]_{\text{equilibrium}})^2 - K_w}{[\text{OH}^-]_{\text{equilibrium}}} \quad (3)$$

and substituting Equation 3 in Equation 1, the pH of the LipHosomes suspension can be correlated to the concentration of the nanovesicles according with the following equation (Eq. 4):

$$\begin{aligned} [\text{LipHosomes}] &= \text{N}^\circ \text{LipHosomes} / \text{NA} = \\ &= (\text{mol}(\text{OH}^-)_{\text{released}} / \text{mol}(\text{OH}^-)_{\text{single liposome}}) / \text{NA} = \\ &= ([\text{OH}^-]_{\text{released}} / ([\text{OH}^-]_{\text{single liposome}} \times V_{\text{intra liposome}})) / \text{NA} \end{aligned} \quad (4)$$

The sensitivity of the method is of course dependent on the concentration of entrapped OH^- . However, two limitations have to be taken in account, namely: *i*) the iso-osmotic condition for the inner and the outer compartments should hold, in the case of biological samples this value has to be isotonic *i.e.* 300 mOsm/L; *ii*) the ratio between OH^- and phospholipids has to be lower than the saponification value.³⁴

A route to increase the OH^- payload was to consider the Giant Unilamellar Vesicles (GUVs)³³ (Fig. 1).

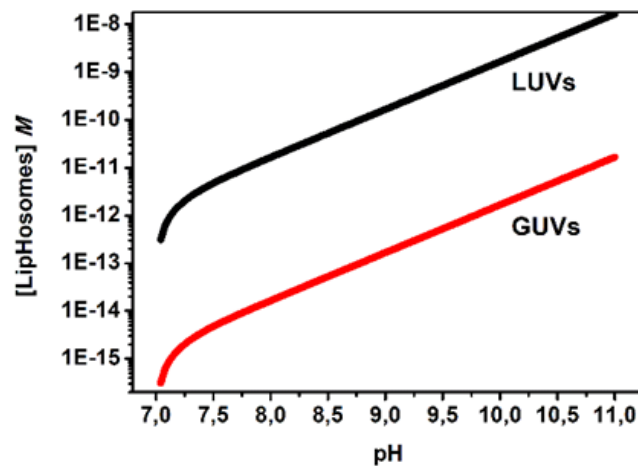


Figure 1. Concentration of OH^- loaded LipHosomes vs. pH generated in the medium upon the release of their payload., calculated on the assumption that *i*) GUVs own a mean diameter of 1 μm and entrap 100 mM of NaOH (*red line*) and *ii*) LUVs have a mean diameter of 100 nm and entrap 100 mM of NaOH (*black line*), respectively.

Notably, the sensitivity in terms of LipHosomes concentration using giant LipHosomes reaches the fM range, which appears very suitable for applications aimed at assaying the detection of the less concentrated biomarkers. In particular, when the comparison is carried out with ELISA-like tests, it is important to note that, in the herein reported approach, the stoichiometry of the interaction between a LipHosome and the analyte is 1:1. Therefore the detection limit of concentration of LipHosomes immediately identifies the threshold sensitivity of the analyte detection. The sensitivity threshold reported for standard colorimetric ELISA tests is in the order of pM, so in principle, this method appears more sensitive. As anticipated in the introduction, the sensitivity threshold of ELISA assays has been pushed further by developing different types of amplification strategies (e.g. magnetic immunoassays¹¹, radio immunoassays¹², liposome-based immunoassays) able to reach the fM concentration threshold. Referring to the above-mentioned methods, our approach has the advantage of using much cheaper reagents and technology that can be applied in the field without the involvement of specialized personnel to perform the analysis. On the basis of these preliminary calculations, LipHosomes of Formulation A were tested in a real experiment.

Formulation A (LUVs)

Samples with different concentration of LipHosomes of Formulation A (LUVs) were prepared and independently heated at 55°C for 10 minutes to induce the full release of the liposomal content. Afterwards, the pH of the suspension was measured, and the results are reported in Figure 2.

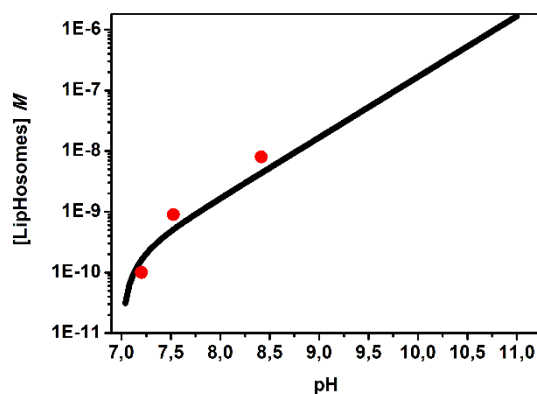


Figure 2. pH dependence on the concentration of LipHosomes after the release of their content. *Black line*: calculated curve (see above) using the parameters of Formulation A. *Red circles*: pH readouts for the real experiments with LipHosomes of formulation A.

The pH values measured after the release of the liposomal payload are quite close to the calculated values. However, the measured values were lower than expected for the two more concentrated samples, while in the less concentrated sample the pH was slightly higher.

The discrepancies in pH measurements have to be related to the fact that the pH readout was not carried out in a buffered solution, *i.e.* the pH resulted very unstable over time as a consequence of the slow acidification associated to the progressive CO₂ dissolution in the solution. To avoid such pH instability, we deemed useful encapsulating a basic, but buffered, solution, *e.g.* sodium bicarbonate, in the LipHosomes.

LipHosomes encapsulating sodium bicarbonate

As the theory anticipates different dilution effect of the released salt upon the LipHosomes concentration, the simulation of the pH dependence on the concentration of LipHosomes encapsulating a sodium bicarbonate buffer appears rather difficult due to the complexity of the multiple equilibria present in solution.

The experiment was carried out as follows: *i)* a 150 mM solution of sodium bicarbonate was prepared, *ii)* the solution was basified with NaOH to pH 10,0, *iii)* the solution was diluted with water several times in the range comprised between 2.5×10^{-2} M and 1.25×10^{-6} M, *iv)* the pH was measured after each dilution.

The salt concentration was expressed as $[\text{HCO}_3^-]_{\text{nominal}}$ which represents the nominal amount of bicarbonate, *i.e.* the pH dependent transformation of HCO₃⁻ in CO₂ and CO₃²⁻ ion was not considered.

The obtained data (Figure 3) displayed a region (0.01 - 1 mM) in which the pH readout (that ranges from 7.5 to 9.5) is very sensitive to the salt concentration. At concentrations higher than 1 mM and lower than 0.01 mM the pH is almost independent of the salt concentration.

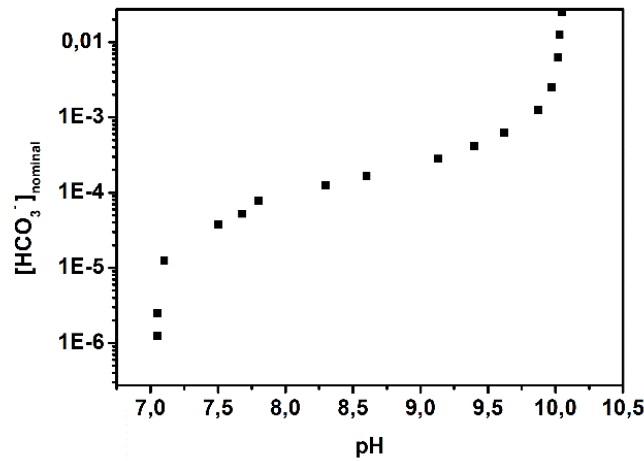


Figure 3. Nominal concentration of NaHCO₃ in solution vs. pH.

Once known the mean diameter of the vesicles and the concentration of their payload, in analogy to what done above in the case of NaOH encapsulation, the number of releasing LipHosomes (in 1 L of suspension) can be correlated to the concentration of the released HCO₃⁻ as shown by Equation 5:

$$\begin{aligned}
 [HCO_3^-]_{released} &= N^\circ \text{ liposomes} \cdot (\text{mol of } HCO_3^-)_{single \text{ liposome}} = \\
 &= N^\circ \text{ liposomes} \cdot [HCO_3^-]_{single \text{ liposome}} \cdot V_{inside \text{ liposome}} \\
 [LipHosomes] &= N^\circ_{LipHosomes} / NA = \\
 &= (\text{mol}(HCO_3^-)_{released} / \text{mol}(HCO_3^-)_{single \text{ liposome}}) / NA = \\
 &= ([HCO_3^-]_{released} / ([HCO_3^-]_{single \text{ liposome}} \times V_{intra\text{liposome}})) / NA
 \end{aligned} \tag{5}$$

Figure 4 displays this correlation, after substituting [HCO₃⁻]_{nominal} to [HCO₃⁻]_{released}, for both LUVs and GUVs formulations, which confirms the difference already observed in the formulations loaded with NaOH.

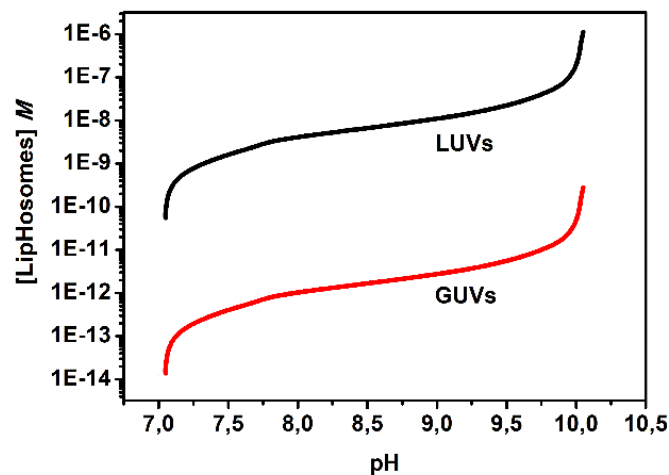


Figure 4. pH dependence on the concentration of bicarbonate loaded LipHosomes, estimated for GUVs (diameter 1 μm, red line) and LUVs (diameter 100 nm, black line) entrapping 150 mM of NaHCO₃.

Furthermore, the data reported in Figure 4 clearly indicates that the validity range of this method in terms of LipHosomes concentration is spanned over two orders of magnitude (0.1 - 10 nM for LUVs and 0.1 - 10 pM for GUVs), instead of the 4 orders determined for the LipHosomes loaded with a strong base (Figure 1).

After having experimentally simulated the expected pH values following the release of LipHosomes loaded with bicarbonate at pH 10, real release experiments were planned and executed using formulations B and C.

Formulations B (LUVs) and C (GUVs)

Samples containing different concentration of LipHosomes of formulation B (LUVs) were prepared and independently heated at 55°C for 10 minutes to induce the full release of the liposomal payload. Afterwards, the pH of the suspension was measured, and the results are reported in Figure 5 (batch 1, magenta triangles). The same plot reports the results obtained using a second and a third batches of formulation B of LipHosomes (green triangles and orange triangles, respectively).

The over imposition of the experimental data with those showed in Figure 4 for LUVs with similar size, shows a good agreement, as well as a good inter-pH reproducibility.

The same procedure (except for the triggering stimulus, in this case operated by the addition of TRITON-X) was applied for the formulation C, GUVs loaded with bicarbonate 150 mM at pH 10.

The excellent agreement between experimental and calculated data (Figure 5) confirmed the good reliability of this approach.

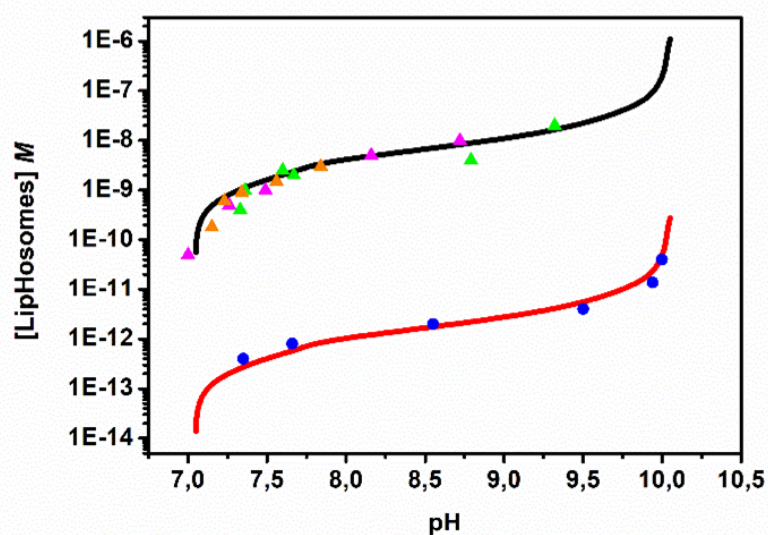
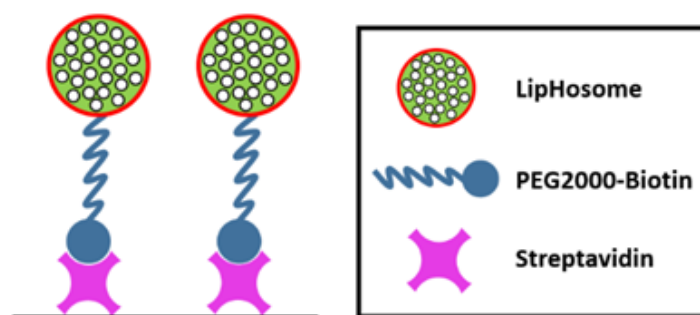


Figure 5. pH dependence on the concentration of LUVs and GUVs LipHosomes loaded with bicarbonate. *Magenta triangles*: LipHosomes of formulation B, batch 1 (LUVs). *Green triangles*: LipHosomes of formulation B, batch 2 (LUVs). *Orange triangles*: LipHosomes of formulation B, batch 3 (LUVs). *Black line*: calibration data for liposomes with similar size and composition of formulation B. *Blue circles*: LipHosomes of formulation C (GUVs). *Red line*: calibration data for liposomes with similar size and composition of formulation C.

Validating the method in a ligand/anti-ligand test

LipHosomes are expected to find application as reporters for a number of *in vitro* diagnostic tests based on the ligand/anti-ligand binding. Herein we report preliminary observations obtained by using a biotinylated LipHosome designed to recognize streptavidin molecules deposited on the bottom of a plate. Scheme 2 illustrates the ligand/anti-ligand assay taken as test in this work.



Scheme 2: Example of the direct ligand/anti-ligand assay using LipHosomes tested in this work.

In this case, the assay consisted of the direct binding between the anti-ligand, immobilized on a plate, and the properly functionalized LipHosome.

The biotin/streptavidin association is at the basis also of commonly applied indirect assays where the ligand/anti-ligand recognition occurs via a third molecular partner that is able to bind both ligand and anti-ligand. Thus, the sensibility threshold from the herein reported experiment is of general applicability.

The analyte anti-ligand to be detected is streptavidin which binds directly to the ligand molecules (biotinylated LipHosomes), to form ligand/anti-ligand binding complexes. In the reported experiment streptavidin is already adsorbed on a 96-well microplate.

Giant LipHosomes containing a biotinylated phospholipid on their membrane and 150 mM bicarbonate in the inner aqueous cavity were prepared (Formulation D). Freshly prepared LipHosomes at a concentration of about $1 \cdot 10^{-11}$ M, were incubated in the microplates for 15 minutes. Then the microplates were washed with NaCl 0.15 M at pH 7.0. A solution of TRITON-X at pH 7.0 was added to the microplates and the pH was measured in continuous for 15 minutes. Full release of the vesicle content was achieved 1 minute after the addition of the surfactant. These data allow us to conclude that the herein proposed method is a fast-responding one.

A 0.2 units increase of pH was measured. According to calibration curve reported in Figure 4, this value indicates that about $1 \cdot 10^{-13}$ M of LipHosomes were bound to the plates.

This experiment was repeated five times and results are reported in Figure 6 (Mean \pm SD). As control, the same experiment was carried out using Giant LipHosomes of analogous size and membrane composition (Formulation C) but deprived of biotin moieties on the external surface. In the latter case the pH variation resulted to be about 0.05 units. As further control, microplates were added with washing solution alone (NaCl 0.15 M pH 7.0). The controls were repeated 5 times and results are reported in Figure 6 (Mean \pm SD).

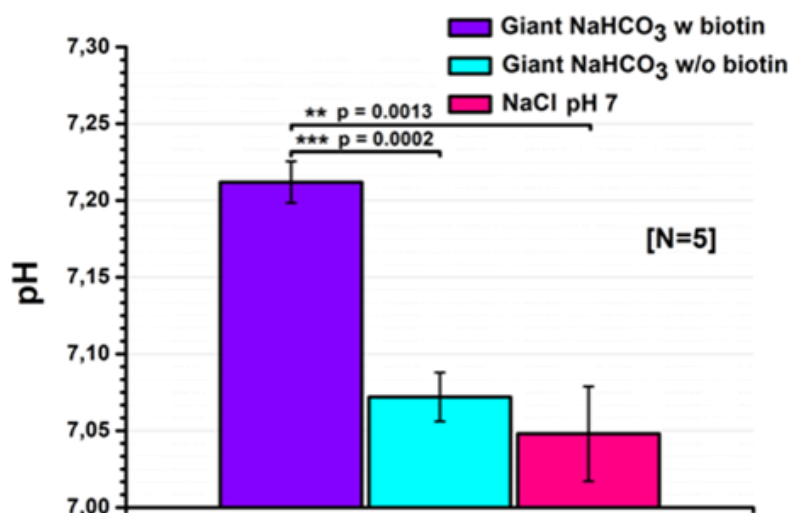


Figure 6: pH variation after direct ligand/anti-ligand assay using giant LipHosomes with biotin (*Formulation D, Violet*), giant LipHosomes without biotin (*Formulation C, Cyan*) and washing solution of NaCl 0.15 M pH 7 (*Pink*).

The statistical analysis of the results showed that the difference between functionalized and control LipHosomes is statistically significant (unpaired two-tails T student test, $p = 0.0002$).

Conclusions

LipHosomes represent a platform of reporters that may be used to design many low costs dosing tests. Herein a proof of concept of their potential efficacy in ELISA-like tests where the analyte is immobilized on a solid plate is reported. It has been shown that the markedly high sensitivity shown by the use of GUVs may pave the way to a new generation of highly sensitive dosing method based on pH reading.

The main advantage of the proposed test over other electrochemical immunoassays, is represented from *i)* the use of reagents much cheaper rather than enzymes and *ii)* from the rapidity of the response (1 minute). Moreover, electrochemical methods based on pH readout have the advantage over other dosing tests of making use of an easy to handle and low cost instrumentation, almost present in every analysis laboratory and that doesn't require highly qualified personnel to perform the analysis.

For the abovementioned reasons we believe that LipHosomes would represent a very interesting platform for the development of new dosing method that can be applied to a wide range of diagnostic biomarkers.

Experimental

Chemicals: 1,2-dipalmitoyl-sn-glycero-3-phosphocholine (DPPC), 1,2-distearoyl-sn-glycero-3-phosphoethanolamine-N-[methoxy(polyethylene glycol)-2000] (ammonium salt) (DSPE-mPEG2000), 1,2-distearoyl-sn-glycero-3-phosphoethanolamine -N-[biotinyl(polyethylene glycol)-2000] (ammonium salt) (DSPE-PEG2000Biotin) were purchased from Avanti Polar Lipids Inc. Sodium chloride, sodium hydroxide, sodium bicarbonate, TRITON-X, chloroform and all the other chemicals were acquired from Sigma Aldrich Co. LLC.

Liposomes preparation: Small LipHosomes (Formulation A and B) were prepared by using the thin lipidic film method.³⁵ Briefly, the desired mixture of phospholipids dissolved in chloroform (DPPC/DSPEmPEG2000 95/5 molar ratio) was dried under vacuum in a rotavapor system, until a thin film was formed on a round bottom flask. The film was then hydrated at 55°C with the hydration solution (1 mL NaOH 1 mM or 1 mL bicarbonate 150 mM). The solution was vortexed to form multilamellar vesicles and then sonicated with a sonicator tip to form Large Unilamellar Vesicles (LUVs). The final suspension of vesicles was purified by exhaustive dialysis carried out at 4°C against 0.15 M NaCl aqueous solution. The vesicles were characterized by using DLS (Zetasizer NanoZS, Malvern, UK) to define the mean hydrodynamic diameter and the polydispersity of the system.

Giant LipHosomes (Formulation C and D) were prepared according to a procedure reported in literature with modifications.³³ The mixture of phospholipids (0.0224 mmol) dissolved in chloroform (DPPC/DSPEmPEG200 or DPPC/DSPE-PEG2000Biotin 97/3 molar ratio) was spread on the bottom of a 2 L flask and it was dried for 15 minutes with a flux of Argon. The hydration solution (25 mL of 150 mM bicarbonate buffer) was then carefully added and the flask was set for 2 h at 60°C without any mechanical stress. Next, the flask is mildly swirled, the cloudy suspension recovered and cooled to room temperature. The suspension is centrifuged 30 minutes at 6500 rpm in a fixed 45° angle centrifuge to purify the giant LipHosomes from impurities and small liposomes populations eventually present. The supernatant is removed, fresh NaCl 0.15 M is added, the centrifugation is repeated and the purified sample is resuspended in NaCl 0.15 M at pH 7.0.

DLS measurements were achieved to ensure there was no evidence of populations of liposomes between 50 nm and 800 nm.

Vesicle size distribution: To characterize LUVs suspensions we used Dynamic Light Scattering (DLS). The average size is 101.9 nm and the polydispersion index resulted to be 0.178.

To achieve a GUVs suspension size distribution, we used fluorescence microscopy (Figure 7).

We used a Rhodamine-labelled phospholipid to highlight the burden of the vesicle (red) and aqueous carboxyfluorescein inside the vesicle (green). We acquired different Z-stack images in order to center every vesicle in its main diameter and measured it. The distribution was fitted with Landau equation and the size resulted to be $1.2 \pm 0.15 \mu\text{m}$.

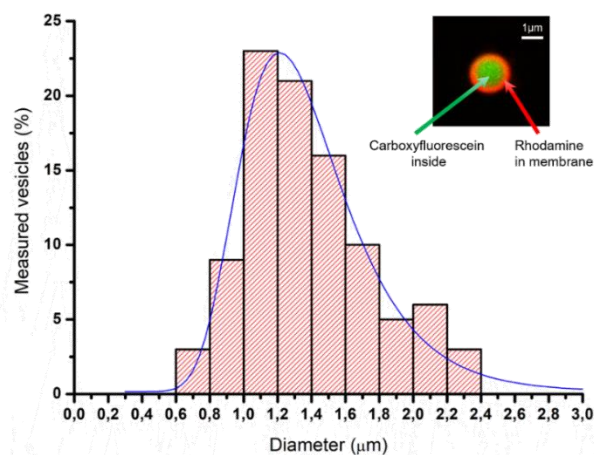


Figure 7. Size distribution of fluorescent GUVs containing a Rhodamine-labelled phospholipid in the membrane (red) and aqueous carboxyfluorescein inside the vesicle (green) as reported in the confocal microscopy image of a GUV in the top corner of the figure.

Study of the stability of the intact vesicles in saline solution and serum: The stability of integer LipHosomes suspensions (Formulation B and C) was tested in order to assess whether a spontaneous release of the payload could occur. Freshly prepared and purified LipHosomes underwent pH measurements in continuous for three hours (FiveEasy Plus pH meter with pH electrode InLab Micro purchased from METTLER TOLEDO).

Meanwhile, an aliquot of the freshly prepared and purified LipHosomes was induced to release its content without previous pH monitoring to be used as reference. All the samples were tested in triplicate and no statistic significant difference in pH value was found among the samples after monitoring (3 hours) and towards reference solution after rupture.

The stability of LipHosomes of Formulation C was also tested in human serum. Freshly prepared and purified LipHosomes were incubated with human serum for 1 hour and then extensively washed with NaCl 0.15 M at pH 7.0. Afterward, they were induced to release their content and pH was measured. As control, a suspension of LipHosomes of Formulation C was maintained for 1 hour with NaCl 0.15 M instead of human serum. No significant variation in the final pH value between samples occurred, suggesting a good stability of these newly proposed vesicles also in the presence of biological fluids.

The complete release of the payload could be achieved in two different ways *i)* by heating the aqueous suspension of vesicles at 55°C for ten minutes, or *ii)* by adding a solution of TRITON-X 1X at pH 7.0 to the suspension of LipHosomes and wait for 1 minute.

Ligand/anti-ligand diagnostic test: Freshly prepared and purified giant LipHosomes of Formulation C and D at a concentration of about $1 \cdot 10^{-11}$ M, were incubated in a 96-well streptavidin-coated microplate (purchased from Greiner Bio-One International) for 15 minutes. Then the microplate is washed 5 times with NaCl 0.15 M at pH 7.0. Then, LipHosomes were induced to release their content with TRITON-X and the pH was measured 15 minutes later. As further control, microplates were added with washing solution alone (NaCl 0.15 M pH 7.0). The experiments were carried out in quintuplicate and the statistical analysis of the results was achieved by unpaired two-tails T student test.

References

1. Pattni, B. S., Chupin, V. V., & Torchilin, V. P. (2015). New developments in liposomal drug delivery. *Chemical reviews*, 115(19), 10938-10966.
2. Storm, G., & Crommelin, D. J. (1998). Liposomes: quo vadis?. *Pharmaceutical science & technology today*, 1(1), 19-31.
3. El-Hammadi, M. M., & Arias, J. L. (2019). An update on liposomes in drug delivery: a patent review (2014-2018). *Expert opinion on therapeutic patents*, 29(11), 891-907.
4. Strijkers, G. J., Kluza, E., Van Tilborg, G. A., van der Schaft, D. W., Griffioen, A. W., Mulder, W. J., & Nicolay, K. (2010). Paramagnetic and fluorescent liposomes for target-specific imaging and therapy of tumor angiogenesis. *Angiogenesis*, 13(2), 161-173.
5. Quesada-González, D., & Merkoçi, A. (2015). Nanoparticle-based lateral flow biosensors. *Biosensors and Bioelectronics*, 73, 47-63.
6. Ferrauto, G., Di Gregorio, E., Ruzza, M., Catanzaro, V., Padovan, S., & Aime, S. (2017). Enzyme-Responsive LipoCEST Agents: Assessment of MMP-2 Activity by Measuring the Intra-liposomal Water 1H NMR Shift. *Angewandte Chemie*, 129(40), 12338-12341.
7. Gao, Y., Huang, X., Zhu, Y., & Lv, Z. (2018). A brief review of monoclonal antibody technology and its representative applications in immunoassays. *Journal of Immunoassay and Immunochemistry*, 39(4), 351-364.
8. Yin, Y., Cao, Y., Xu, Y., & Li, G. (2010). Colorimetric immunoassay for detection of tumor markers. *International journal of molecular sciences*, 11(12), 5077-5094.
9. Shah, K., & Maghsoudlou, P. (2016). Enzyme-linked immunosorbent assay (ELISA): the basics. *British journal of hospital medicine*, 77(7), C98-C101.
10. Zhang, S., Garcia-D'Angeli, A., Brennan, J. P., & Huo, Q. (2014). Predicting detection limits of enzyme-linked immunosorbent assay (ELISA) and bioanalytical techniques in general. *Analyst*, 139(2), 439-445.
11. Davies, G. E., & Janata, J. (1979). *U.S. Patent No. 4,177,253*. Washington, DC: U.S. Patent and Trademark Office.
12. Grange, R. D., Thompson, J. P., & Lambert, D. G. (2014). Radioimmunoassay, enzyme and non-enzyme-based immunoassays. *British journal of anaesthesia*, 112(2), 213-216.
13. Ren, R., Cai, G., Yu, Z., & Tang, D. (2018). Glucose-loaded liposomes for amplified colorimetric immunoassay of streptomycin based on enzyme-induced iron (II) chelation reaction with phenanthroline. *Sensors and Actuators B: Chemical*, 265, 174-181.

14. Horie, M., Yanagisawa, H., & Sugawara, M. (2007). Fluorometric immunoassay based on pH-sensitive dye-encapsulating liposomes and gramicidin channels. *Analytical biochemistry*, 369(2), 192-201.
15. Haga, M., Hoshino, S., Okada, H., Hazemoto, N., Kato, Y., & Suzuki, Y. (1990). An improved chemiluminescence-based liposome immunoassay involving apoenzyme. *Chemical and pharmaceutical bulletin*, 38(1), 252-254.
16. Cai, G., Yu, Z., Tong, P., & Tang, D. (2019). Ti₃C₂ MXene quantum dot-encapsulated liposomes for photothermal immunoassays using a portable near-infrared imaging camera on a smartphone. *Nanoscale*, 11(33), 15659-15667.
17. Zhi, L. J., Sun, A. L., & Tang, D. (2020). In situ amplified photothermal immunoassay for neuron-specific enolase with enhanced sensitivity using Prussian blue nanoparticle-loaded liposomes. *Analyst*, 145(12), 4164-4172.
18. Liang, J., Wang, J., Zhang, L., Wang, S., Yao, C., & Zhang, Z. (2019). Glucose oxidase-loaded liposomes for in situ amplified signal of electrochemical immunoassay on a handheld pH meter. *New Journal of Chemistry*, 43(3), 1372-1379.
19. Tang, Y., Tang, D., Zhang, J., & Tang, D. (2018). Novel quartz crystal microbalance immunodetection of aflatoxin B1 coupling cargo-encapsulated liposome with indicator-triggered displacement assay. *Analytica chimica acta*, 1031, 161-168.
20. Lin, Y., Zhou, Q., Zeng, Y., & Tang, D. (2018). Liposome-coated mesoporous silica nanoparticles loaded with L-cysteine for photoelectrochemical immunoassay of aflatoxin B 1. *Microchimica Acta*, 185(6), 1-9.
21. Tang, J., Huang, Y., Liu, H., Zhang, C., & Tang, D. (2016). Novel glucometer-based immunosensing strategy suitable for complex systems with signal amplification using surfactant-responsive cargo release from glucose-encapsulated liposome nanocarriers. *Biosensors and Bioelectronics*, 79, 508-514.
22. Lin, Y., Zhou, Q., & Tang, D. (2017). Dopamine-loaded liposomes for in-situ amplified photoelectrochemical immunoassay of AFB1 to enhance photocurrent of Mn²⁺-doped Zn₃(OH) 2V₂O₇ nanobelts. *Analytical chemistry*, 89(21), 11803-11810.
23. Ishikawa, E., Imagawa, M., Hashida, S., Yoshitake, S., Hamaguchi, Y., & Ueno, T. (1983). Enzyme-labeling of antibodies and their fragments for enzyme immunoassay and immunohistochemical staining. *Journal of Immunoassay and Immunochemistry*, 4(3), 209-327.
24. Poznansky, M. J., & Juliano, R. L. (1984). Biological approaches to the controlled delivery of drugs: a critical review. *Pharmacological reviews*, 36(4), 277-336.

Chapter 5: LipHosomes as a new diagnostic tool

25. Toonen, P. A. H. M., & Crommelin, D. J. A. (1983). Immunoglobulins as targeting agents for liposome encapsulated drugs. *Pharmaceutisch Weekblad*, 5(6), 269-280.
26. Connor, J., Sullivan, S., & Huang, L. (1985). Monoclonal antibody and liposomes. *Pharmacology & therapeutics*, 28(3), 341-365.
27. Hansen, C. B., Kao, G. Y., Moase, E. H., Zalipsky, S., & Allen, T. M. (1995). Attachment of antibodies to sterically stabilized liposomes: evaluation, comparison and optimization of coupling procedures. *Biochimica et Biophysica Acta (BBA)-Biomembranes*, 1239(2), 133-144.
28. Rongen, H. A. H., Bult, A., & Van Bennekom, W. P. (1997). Liposomes and immunoassays. *Journal of immunological methods*, 204(2), 105-133.
29. A. George, P. Tan, (2003). Immunoliposomes formed with aggregated antibody, *World patent WO 101427*.
30. Alyane, M., Barratt, G., & Lahouel, M. (2016). Remote loading of doxorubicin into liposomes by transmembrane pH gradient to reduce toxicity toward H9c2 cells. *Saudi pharmaceutical journal*, 24(2), 165-175.
31. Fatima, M. T., Islam, Z., Ahmad, E., Barreto, G. E., & Ashraf, G. M. (2018). Ionic gradient liposomes: Recent advances in the stable entrapment and prolonged released of local anesthetics and anticancer drugs. *Biomedicine & Pharmacotherapy*, 107, 34-43.
32. Scarpa, A., & Gier, J. D. (1971). Cation permeability of liposomes as a function of the chemical composition of the lipid bilayers. *Biochimica et Biophysica Acta (BBA)-Biomembranes*, 241(3), 789-797.
33. Reeves, J. P., & Dowben, R. M. (1969). Formation and properties of thin-walled phospholipid vesicles. *Journal of cellular physiology*, 73(1), 49-60.
34. R. Barrett, in *Therapeutic Chemistry: Fundamentals*, (2018). Elsevier, San Diego, Chapter 3, pp. 57-78.
35. V. P. Torchilin, V. Weissig, in *Liposomes: Practical Approach*, (2003). Oxford University Press, NY, USA, 2nd ed., pp. 4-7.

- Chapter 6 -

Concluding remarks and future perspectives

Concluding remarks and future perspectives

The aim of this thesis was to develop innovative and highly sensitive smart probes for diagnostic and Molecular Imaging applications.

Over the last twenty years, the MRI sensitivity issue has been faced by developing nanocarriers able to deliver high contrast agents' payload at the site of interest: from the use of dendrimers to liposomes, passing through protein-based carriers. Even though these systems represent valid examples of Molecular Imaging probes, there could be still work to do to increase their efficiency. In this work, the main efforts rely on the development of a new vesicle-based micrometric system provided with a high sensitivity and biocompatibility based on the use of Giant Unilamellar Vesicles (GUVs).

In particular, the target of the work was to design and evaluate a new microsystem preserving the advantages of nanosized liposomes and trying to overcome their limits.

Liposomes are characterized by a biocompatible structure and a versatile membrane and cavity in which imaging reporters or drugs can be englobed. Unfortunately, nanosized liposomes present some limits especially when interacting with the biological systems. In particular, Large Unilamellar Vesicles (LUVs) undergo a high macrophagic uptake resulting in a reduced specific targeting; moreover their internalization into cells implies their disassemblment causing the release of their content that for some applications is the wanted result but for other applications it might hamper their efficacy.

Throughout all the work, we extensively compared the behaviour of GUVs and LUVs. In **Chapter 2**, both are studied to better understand their efficiency as LipoCEST probes; the main result of this study was three order of magnitude higher efficiency in the generation of CEST signal by using GUVs with respect to LUVs.

Moreover, the behaviour of vesicles towards osmotic shock resulted to be very different. On one hand as reported in literature, shrunken LUVs acquire a cigar-like shape capable of orienting them in the magnetic field; on the other hand, shrunken GUVs could not orient in magnetic field, due to their amorphous shape resulting from the osmotic stress. At the end of Chapter 2, the behaviour towards macrophagic uptake of LUVs and GUVs is also reported; while LUVs are almost completely seized by macrophages, Giant Unilamellar Vesicle uptake seems to be negligible.

This behaviour toward cells is confirmed by the work detailed in **Chapter 3**, in which another application GUVs could find space for is reported. Folate-targeted fluorescent GUVs were designed and their interaction with Folate Receptor (FR) overexpressing cells (IGROV-1) was studied with fluorescent microscopy. Due to their size, GUVs were clearly visible by fluorescent microscopy; the main result of this study is the direct observation of their anchorage to the cell membrane that wasn't followed by any internalization. In case of IGROV-1 cells, GUVs are clustered in specific regions of the cell membrane thus indicating a possible clustering of receptors in different zones of cellular membrane. The ability of targeted GUVs to interact with membrane receptors without internalization could pave the way to a different application of these Molecular Imaging probes: mapping the receptors present on the cell surface.

In **Chapter 4**, an *in vivo* application of targeted GUVs is reported; due to their micrometric size, it was decided to explore a vascular target such as integrins overexpressed in U87-MG cells-induced tumour.

In this study, fluorescent RGD-targeted Gd-containing GUVs are studied *in vitro* and *in vivo* experiments to demonstrate that tiny amount of Gadolinium (not detectable with conventional T₁ contrast) could be indirectly visualized using Magnetization Transfer Contrast Magnetic Resonance Imaging protocol. Moreover, the MTC-MRI results were elegantly confirmed by immunofluorescence were rhodamine-bearing RGD-targeted GUVs resulted to be localized exactly in correspondence of endothelial cells of vessels of the tumor, while they were absent in control mice were MTC-MRI contrast could not be appreciated.

In order to highlight the versatility of Large and Giant Unilamellar Vesicles, in **Chapter 5**, a different kind of their application is studied and reported; in particular, LUVs and GUVs are exploited as probes to assess a pH readout-based ligand/anti-ligand assay.

In this study, liposomes are designed to contain a pH changer molecule to be released upon a suitable external stimulus such as heat, ultrasounds or surfactants, thus generating a difference in pH in the medium. Suspensions of LUVs and GUVs containing bicarbonate buffer were tested towards calculated calibration curves in order to correlate the resulting difference of pH with the concentration of the probe. At the end of the work a proof of concept of the feasibility of this diagnostic kit is reported; in particular biotin-targeted GUVs containing bicarbonate buffer were incubated onto streptavidinated plates and induced to release their content by surfactants, resulting in a significant variation of pH with respect to control experiments.

In conclusion, this thesis highlights the versatility of Giant Unilamellar Vesicles as contrast agents and diagnostic kit tools by playing with their different payload: *i*) Tm- and Dy-complexes were used to exploit GUVs as LipoCEST agents, *ii*) Gd-complexes to study them as targeted MTC-MRI probes, *iii*) fluorescent dyes to report on membrane receptor distribution and *iv*) bicarbonate buffer to use them in a ligand/anti-ligand assay based on pH readout.

Much work has undoubtedly to be carried out to efficiently exploit GUVs as a new Molecular Imaging platform, paving the way to translate them to diagnostic, preclinical and eventually clinical level. The development of differently targeted GUVs, together with the optimization of diagnostic assay protocols can allow translating the obtained results to a preclinical level or an *in vitro* diagnostic kit.

List of abstracts

G. Ferrauto, **M. Tripepi**, E. Di Gregorio, V. Bitonto, S. Aime, D. Delli Castelli, "Targeting of cancer integrins by using RGD/Gd-Giant Unilamellar vesicles by exploiting Magnetization Transfer Contrast MRI" WMIC 2020, (Co-author in oral presentation)

G. Ferrauto, E. Di Gregorio, **M. Tripepi**, V. Bitonto, S. Aime, D. Delli Castelli, "Targeting of cancer integrins by using RGD/Gd-Giant Unilamellar vesicles by exploiting Magnetization Transfer Contrast MRI" ESMRMB Congress 2020, (Co-author in oral presentation)

G. Ferrauto, **M. Tripepi**, E. Di Gregorio, V. Bitonto, S. Aime, D. Delli Castelli, "Targeting of cancer integrins by using RGD/Gd-Giant Unilamellar vesicles by exploiting Magnetization Transfer Contrast MRI" EMIM Congress 2020 (Co-author in oral presentation)

M. Tripepi, G. Ferrauto, P. O. Bennardi, S. Aime, and D. Delli Castelli "Giant Unilamellar Vesicles (GUVs) as highly sensitive MRI contrast agents". Merck Young Chemists' Symposium 2019 (MYCS), Rimini (Poster Presentation & Flash Communication)

G. Ferrauto, E. Di Gregorio, **M. Tripepi**, D. Delli Castelli, S. Aime, "Nano- and micro-sized systems as highly sensitive CEST MRI probes", CMR Erice (TP) 2019 (Co-author in oral presentation)

M. Tripepi, G. Ferrauto, P. O. Bennardi, D. Delli Castelli, S. Aime "Paramagnetic Giant Liposomes as Highly Sensitive Versatile MRI Contrast Agents". GIDRM 2019, L'Aquila. (Oral Presentation)

M. Tripepi, G. Ferrauto, P. O. Bennardi, M. Gai, D. Delli Castelli, S. Aime "Giant liposomes as a new versatile Molecular Imaging platform". EMIM 2019, Glasgow (Oral Presentation)

M. Tripepi, G. Ferrauto, P. O. Bennardi, M. Gai, D. Delli Castelli, S. Aime. "Giant Liposomes as Highly Sensitive Versatile MRI Contrast Agents". GIDRM 2018, Torino (Poster Presentation)

M. Tripepi, F. Capuana, E. Gianolio, F. V. C. Kock, A. Pagoto, R. Stefania, G. Digilio, S. Aime "Synthesis of high relaxivity Gadolinium AAZTA tetramers as building blocks for bioconjugation" Challenges of Magnetic Resonance in Life Sciences - EMBO Workshop 2018, Grosseto (Poster Presentation)

List of publications

Tripepi M., Bennardi P.O., Ferrauto G., Aime S., Delli Castelli D., (2020), "Liposomes: Reporters for Ligand/Anti-Ligand Assays Based On pH Readout", *Analysis&Sensing*

Ferrauto G., **Tripepi M.**, Di Gregorio E., Bitonto V., Aime S., Delli Castelli D., (2020), "Detection of U-87 tumour cells by RGD-functionalized/Gd-containing Giant Unilamellar Vesicles (Gd-GUVs) in Magnetization Transfer Contrast (MTC)-MR images", *Investigative Radiology*

Mansourizadeh F., Alberti D., Bitonto V., **Tripepi M.**, Sepehri H., Khoee S., Crich S.G., (2020), "Efficient synergistic combination effect of Quercetin with Curcumin on breast cancer cell apoptosis through their loading into Apoferritin cavity", *Colloids and Surfaces B: Biointerfaces*

Tripepi M., Ferrauto G., Bennardi P.O., Aime S., Delli Castelli D. (2020), "Challenging the Sensitivity of Imaging Probes Targeting Epitopes on the External Surface of Cellular Membranes", *Submitted*

Tripepi M., Ferrauto G., Bennardi P.O., Aime S., Delli Castelli D., (2020), "Multilamellar LipoCEST Agents Obtained from Osmotic Shrinkage of Paramagnetically Loaded Giant Unilamellar Vesicles (GUVs)", *Angewandte Chemie*

Pagoto A., Garelo F., Marini G.M., **Tripepi M.**, Arena F., Bardini P., Stefania R., Lanzardo S., Valbusa G., Porpiglia F., Manfredi M. (2019), "Novel Gastrin-Releasing Peptide Receptor Targeted Near-Infrared Fluorescence Dye for Image-Guided Surgery of Prostate Cancer", *Molecular Imaging and Biology*

Pagoto A., **Tripepi M.**, Stefania R., Lanzardo S., Livio Longo D., Garelo F., Porpiglia F., Manfredi M., Aime S., Terreno E. (2019), "An efficient MRI agent targeting extracellular markers in prostate adenocarcinoma", *Magnetic Resonance in Medicine*

Tripepi M., Capuana F., Gianolio E., Kock F.V.C., Pagoto A., Stefania R., Digilio G., Aime S. (2018), "Synthesis of High Relaxivity Gadolinium AAZTA Tetramers as Building Blocks for Bioconjugation", *Bioconjugate Chemistry*